THE EFFECTS OF OUTGASSING JETS ON THE ROTATION OF A COMET NUCLEUS AND ON THE TRAJECTORY OF AN ORBITING SPACECRAFT

by

Sharyl M. Byram

A dissertation submitted in partial fulfillment
of the requirements for the degree of
Doctor of Philosophy
(Aerospace Engineering)
in The University of Michigan
2009

Doctoral Committee:

Professor Daniel J. Scheeres, Chair
Professor Pierre T. Kabamba
Professor N. Harris McClamroch
Research Professor Michael R. Combi

© Sharyl M. Byram 2008
All Rights Reserved

To Andy and my parents

ACKNOWLEDGEMENTS

Completing this thesis was not a solitary effort, I had many contributors over the course of my academic career. I would like to take this opportunity to acknowledge certain people in my life who have helped me achieve this goal. First, I would like to thank my advisor, Professor Daniel Scheeres, for his encouragement, guidance, and unending knowledge of small body dynamics among other things. He has shown remarkable patience and flexibility. Working with him has opened many doors for me.

I would also like to acknowledge some of the people in my life who may not have been directly linked to my formal education and some that were. First, I would like to acknowledge my husband, Andy, who I could not have finished my degrees without. His unconditional confidence in me and my abilities is much appreciated. Next, I would like to thank my entire family for their support of my personal and academic pursuits through the years. I especially would like to thank my parents who have always let me choose my own path in life with what can only be described as silent guidance.

Next,I would like to recognize all of my professors at both the University of Cincinnati and the University of Michigan. They have taught me the necessary tools to be a successful engineer. I'd like to especially thank my master's advisors from the University of Cincinnati, Professor Gary Slater and Professor Trevor Williams. Last but not least, I would not have gotten this far without all the friends that I

have made along the way, especially, Kim Roth, Nick Caldwell, Nick Overman, Oier Penagaricano, Islam Hussein, Julie Bellerose, Steve Broschart, and Ryan Park among many others. They have provided support, friendship, and the needed distractions to keep me motivated and on track.

Finally, I would like to acknowledge the financial support provided during this research by the Jet Propulsion Laboratory at the California Institute of Technology, the Aerospace Engineering Department and the Rackham Graduate School at the University of Michigan.

TABLE OF CONTENTS

LIST OF TABLES

Table

LIST OF FIGURES

Figure

NOMENCLATURE

(Symbols described in detail in the Chapter where they first appear)

Chapter II: Comet Model Description

α	Variable related to the thermal inertia
δ	Jet half angle
ϕ_0	Jet location longitude on comet body
λ_0	Jet location latitude on comet body
θ_{sun}	Angle between the Sun and the jet orientation
ω	Comet rotation rate
a, b, c	Ellipsoid principal semi-major radii, $a, b, c > 0$
$\vec{a}_p$	Outgassing jet acceleration vector
B	Mass to area ratio of the spacecraft normal to the comet
$\vec{e}_{r_{jet}}$	Body fixed unit vector of jet orientation direction
$\vec{e}_{r_{surf}}$	Body fixed unit vector of jet location
p_0	Outgassing pressure at the comet surface
Q_j	Mass ejection rate per unit area
Q_*	Mass ejection rate
$R(t)$	Rotation matrix between $(\hat{x}, \hat{y}, \hat{z})$ and $(\hat{x}_b, \hat{y}_b, \hat{z}_b)$
$\vec{r}$	Spacecraft's position vector
$\vec{r_j}$	Spacecraft position vector relative to jet virtual center
$\vec{r}_{og}$	Outgassing jet centerline
r_p	Jet surface radius
r_s	Comet heliocentric distance
r_0	Jet radius from the center of the comet nucleus
S	Relative intensity of the jet with respect to Q_*
s	Time since ejection
t	Time
U	Comet's gravitational force potential
$\hat{u}_s$	Unit vector pointing towards the Sun
V_{og}	Constant outgassing jet velocity
$(\hat{x}, \hat{y}, \hat{z})$	Non-rotating coordinate system
$(\hat{x}_b, \hat{y}_b, \hat{z}_b)$	Body fixed rotating coordinate system

Chapter III: Comet Nucleus Complex Rotation

κ	Variable based on jet geometry
κ_i	Values of κ, $i = 0, 1, 2...$
Φ_0, Φ_1	Variable based on heliocentric orbit
ϕ	Spin angle
ψ	Precession angle
ρ	Cone angle
σ	Clock angle
θ	Nutation angle
$\vec{\omega}$	Angular velocity vector
A, C	Moments of inertia, $C > A$
$\mathbf{a}$	Coordinate transformation matrix
a_i	Fourier series coefficients, $i = 0, 1, 2...$
D_0, D_1	Variable based on jet geometry
$\mathbf{J}$	Inertia matrix of comet body
K_i	Equilibrium points, $i = 1, 2, 3, 4$
L	Angular momentum magnitude
$\vec{M}$	Moment vector
M_1, M_2	Equilibrium points
M_{xb}, M_{yb}, M_{zb}	Moment vector components in the body fixed frame
M_{xL}, M_{yL}, M_{zL}	Moment vector components in the angular momentum frame
$\mathbf{m}$	Coordinate transformation matrix
N	Number of jets
N_1, N_2	Equilibrium points
$\hat{p}$	Perihelion vector
$\vec{R}_j$	Radius vector of the jet's center in the body fixed frame
$R_{jxb}, R_{jyb}, R_{jzb}$	Comet body fixed components of $\vec{R}_j$
$\mathbf{R_t}$	Attitude rotation matrix
T	Period
$\vec{v}_j$	Outgassing velocity vector
$v_{jxb}, v_{jyb}, v_{jzb}$	Comet body fixed components of $\hat{v}_j$
$\dot{\bar{x}}$	Secular part of the equation of motion,$\dot{x}(t)$
$\dot{x}(t)$	Generic equation of motion
x_p	Periodic magnitude of a generic function, x

Chapter IV: Outgassing Jet Passage Dynamics

μ	Comet gravitational parameter
ν	True anomaly
Ω	Longitude of ascending nodes
ω_p	Argument of periapsis
θ_{rel}	Angle between the outgassing and spacecraft
$\Delta\theta_{err}$	Angle error tolerance

a	Semimajor axis
E	Energy
e	Eccentricity
$\hat{F}_R$, $\hat{F}_T$, and $\hat{F}_N$	Radial, transverse, and orbit normal accelerations
i	Inclination
p	Orbital paramenter
q	Radius of periapsis
v	Spacecraft velocity magnitude

Chapter 5.7: Outgassing Jet Parameter Estimation

a_t, b_t, c_t	Chord lengths
J_c	Cost function
$\hat{u}_c$	Jet estimated center unit vector
$\vec{u}_c$	Jet estimated center vector
$\hat{u}_i$	Boundary crossing unit vector, $i = 1, 2, 3, ...$

Chapter VI: Solar Radiation Pressure and Third Body Effects

η	Reflectance of the spacecraft
λ	Eigenvalue
ρ_0	Initial orbit radius of spacecraft in Hill frame
ω_{com}	Comet heliocentric angular rate
$\dot{\theta}_0$	Initial angular rate of spacecraft in Hill frame
$\mathbf{A}$	Linear matrix of constant coefficients
A_{og}	Strength of the outgassing jet
a, b, c, d, e, f	Constant coefficients
$\vec{a}_{oj}$	Outgassing acceleration vector
C	Zero velocity constant
C_{og}	Zero velocity constant within an outgassing jet
C_s	Zero velocity constant for stable solution
C_u	Zero velocity constant for unstable solution
d_c	Heliocentric distance of the comet
g	Solar radiation pressure magnitude
h	Angular momentum magnitude
h_d	Angular momentum magnitude along comet-Sun line
J	Jacobi integral
J_{og}	Jacobi integral with outgassing
r	Position vector magnitude
$\vec{r}_I$	Spacecraft position vector in an inertial frame
V	Potential function
$\hat{x}$	Direction from Sun to comet
(x, ρ, θ)	Spacecraft position in cylindrical coordinates in Hill frame
(x, y, z)	Spacecraft position in cartesian coordinates in Hill frame

x_0	Initial offset of spacecraft in Hill rotating frame

Chapter VII: Restricted Orbital Motion

Δv	Impulsive velocity change
ρ_-, ρ_+	Spacecraft radius before and after impulsive manuever
$\dot{\theta}_-, \dot{\theta}_+$	Spacecraft angular rate before and after impulsive manuever
m	Scale factor
$\vec{T}$	Thrust vector
$v_{\dot{x}}, v_{\dot{\rho}}, v_{\dot{\theta}}$	Velocity components in cylindrical coordinates
v_-, v_+	Spacecraft velocity before and after impulsive manuever

ABSTRACT

THE EFFECTS OF OUTGASSING JETS ON THE ROTATION OF A COMET NUCLEUS AND ON THE TRAJECTORY OF AN ORBITING SPACECRAFT

by

Sharyl M. Byram

Chair: Daniel J. Scheeres

An outgassing jet model is presented in this thesis in support of spacecraft navigation for future missions to comets. The outgassing jet is modelled as an emission cone while the comet nucleus is modelled as a uniform density triaxial ellipsoid. The heliocentric orbit motion as well as in the strength of the outgassing jet are accounted for in the equations of motion. This model is used for predicting the rotational evolution of a comet nucleus as a result the outgassing jets' reactive torques as well as for simulation of an orbiting spacecraft's trajectory through jet passages and the estimation of the physical outgassing properties of jets from perturbations to the spacecraft's motion.

A model for the rotational evolution of a comet nucleus is presented and predicts possible levels of rotational excitation for a comet nucleus under torques produced by multiple discrete outgassing jets located on the surface. An analytical theory for the secular solution to the rotational motion of comets with an axis of symmetry is

derived and used to predict rotational state changes over multiple perihelion passages. A method of characterizing the comet nucleus dynamics to predict the end state of the rotation is found from the averaged equations. Applications of these analytical results to predict the stochastic evolution of a comet nucleus rotation are outlined.

This thesis also identifies and analyzes stable Sun synchronous orbits in a Hill rotating frame which can be applied to any small body in the solar system. The stability of these orbits is due to the inclusion of solar radiation pressure effects. The stability of the orbits in terms of escaping the comet is analyzed though construction of zero-velocity curves and the use of spectral analysis. The effect of orbital perturbations from outgassing jets on the stability criterion are also considered in the stability analysis of a spacecraft in orbit about a comet. Once these orbits have been identified, the effects of a non-spherical body are explored. In addition, impulsive and finite burn control schemes to restrict a stable orbit's motion are determined, showing that it is feasible to implement a form of orbital hovering in the terminator plane of a comet.

CHAPTER I

Introduction

The small bodies in our solar system contain important information on the early formation of the solar system and are becoming important targets of scientific investigations. The space agencies around the world are sending an increasing number of missions to small bodies, in particular comets. Most recently, the National Aeronautics and Space Administration's (NASA) and the Jet Propulsion Laboratory's (JPL) Deep Impact mission provided to the world high-resolution images of the surface of the comet Tempel 1. The Deep Impact spacecraft is currently enroute to study Comet Hartley 2 for an extended mission, EPOXI. Previous to Deep Impact, NASA and JPL launched Stardust in 1999 which flewby comet P/Wild 2 in January 2001 and returned dust samples from the comet's coma to Earth. This was the first mission to return a comet sample for physical analysis. The Stardust spacecraft is also currently on an extended mission, Stardust NExT, in which it will image the crater left by the Deep Impact mission on Tempel 1. This mission has the additional challenge of needing to accurately predict the rotational state of Tempel 1 to target the correct area to image.

While the missions mentioned and previous ones have flown by and investigated comets from a distance there has yet to be a mission to actually orbit or land on

the surface. This type of mission is near to becoming a reality and the need to determine safe orbits in the vicinity of a comet has become important. In NASA's most recent Announcement of Opportunity[2], a comet surface sample return mission is listed among its top priority mission concepts to develop. The United States is not alone in its quest for more information about comets. The European Space Agency (ESA) is even closer to reaching a comet nucleus with the launch of the Rosetta mission in 2004. It is scheduled to reach comet 67 P/Churyumov-Gerasimenko in 2014, delivering a lander to the surface. Both of the comet sample return mission and Rosetta will involve a period of close proximity to the comet and an orbital phase about the body.

From a scientific point of view, these missions can provide valuable information about the physical composition of comets as well as give insight into the formation of the solar system, but they are also of interest in the field of orbital dynamics. The asymmetrical shape and size of comets yields a set of dynamical problems similar to that of asteroids, but it is the outgassing fields that make the dynamical environment of comets unique. In particular, jets on the surface of the comet eject dust and gas which produce discrete pressure fields for a spacecraft to pass though. It is the description of these outgassing jets and their dynamical implications that will be the focus of this thesis. Describing these outgassing fields has been explored previously. Miller et al. [3] modelled the outgassing of a comet as constant bias non-gravitational acceleration with a variable modelling error acceleration from an active region which is defined by a portion of the surface area of an ellipsoid. Scheeres et al. [4] approached the outgassing acceleration in two cases to determine the stability of the spacecraft in terms of impacting or escaping from the comet. Their first outgassing model assumes that the outgassing field is continuous but variable

depending on the angle made with the Sun. Their second model assumes that the comet has jets emanating from the surface, with spacecraft interaction only acting in the vicinity of the jets.

For the purpose of this work, it will be assumed that the outgassing pressure field is created by a collection of discrete jets on the surface of the comet similar to the second case described in Scheeres et al. [4], although there exist many theories about the structure of a comet's outgassing fields. Crifo et al. [5] theorize that the coma structure is produced by multiple interacting dusty gas jets. Sekanina et al. [6] use a model of comet 81P/Wild 2 from images of dust particles taken by Stardust, which are ejected from a small active source, which make up a thin conical sheet in the coma before the formation is gradually dispersed by various forces. Our model, unlike others, will describe a full three dimensional geometry. We will define and explore a simple model for an outgassing jet from the surface of a comet. A simulation is developed using multiple jets to determine the implications of a jet passage for an orbiting spacecraft. In addition to the model and simulation, this thesis will discuss how the parameters of this model can be estimated using navigational data from a spacecraft's passages through multiple jets' outgassing fields. This research addresses the need for a spacecraft to navigate these discrete jet outgassing fields while in orbit about a comet.

The orbital phase about the nucleus in upcoming missions to comets pose the need to identify stable orbits in a rotating frame. Previously, Dankowicz[7] has found these types of orbits offset from the comet's center of mass in a non-rotating system and explored their stability. Scheeres and Marzari[8] investigated the stability of such orbits accounting for the heliocentric motion of the comet, while Scheeres[9] investigated the definition and stability of Sun-synchronous orbits starting from the

terminator plane. The analysis presented in this thesis combines the offset orbits of Dankowicz[7] with the averaging analysis and heliocentric motion present in the analysis by Scheeres[9]. The stability of identified orbits will be tested for outgassing jet accelerations in the case of comets as well as for variable gravitational forces due to an ellipsoidal body. The implications of passages though outgassing jets fields are explored and a criterion is developed for determining whether a spacecraft's trajectory will remain stable based on the outgassing acceleration magnitude. Once these orbits have been shown to be stable, different control schemes to restrict their allowable motion are explored. The restricted orbits allow for a spacecraft to better map the surface of the comet or monitor certain areas which may have interesting surface activity.

The outgassing jets not only affect an orbiting spacecraft but also have dynamical implications for the comet nucleus itself. For example, as mentioned, NASA's Stardust NExT is planning to target the comet Tempel 1 and image the crater created by Deep Impact. Precise attitude knowledge of the comet's rotation state is crucial to see the crater at its encounter. Long term predictions of the rotation state are equally important as the spacecraft will not arrive when observations of the comet are made, thus the rotational state needs to be propagated over time to determine any trajectory corrections that may need to be made over months or years before the arrival. This thesis will explore both the short term and long terms effects which are also useful beyond missions like Stardust NExT for determining if comets spin up fast enough to break apart and the time scale over which this may happen.

Changes in the rotational state of a comet through perihelion passages has been studied previously. Chesley and Yeomans[10] considered a rotating jet model with non-gravitational accelerations acting on the body to determine rotational drifts.

Neishtadt et al.[11] modelled discrete jets at the surface of the comet and considered the reactive torques on the comet body to cause the angular momentum vector to change. Drahus and Waniak[12] modelled a single active point outgassing in the comet's equatorial plane to simulate observations of spin period changes of Comet C/2001 K5 (LINEAR). Gutiérrez et al.[13] used large active patches on irregularly shaped bodies to simulate the effect of outgassing on the precession of the comet's rotation axis. Samarasinha et al.[14] theorized about outgassing and tidal torques applied to the body to change its spin state while analyzing observational data made on multiple comets.

A portion of this thesis will focus on the effects of outgassing jets on the rotational state of a comet through development of a precise simulation of the equations of motion and derivation of averaged equations for long term predictions verified by the precise simulations. Particular focus will be on the perihelion passages as this is the time when jets are most active. To study the long term effects of the outgassing jets as the comet encounters perihelion multiple times, a method of averaging the equations of motion developed by Neishtadt et al.[11] will be explored and generalized. The generalized averaged equations uncover changes in the comet's rotational state with a focus on the drift in nutation angle, cone angle, and magnitude of the angular momentum over long periods of time without the computationally intense integration of the comet's full equations of motion. These equations will be verified against the full equations of motion assuming an axially symmetric comet body in a complex rotation state with multiple randomly distributed jets of varying strengths creating the time-varying torques on the body.

1.1 Original Contributions

This thesis makes some original contributions to the field of cometary outgassing jet modelling and to the field of dynamics of and about a comet nucleus. The first major contribution of this thesis is a full three-dimensional geometric model of an outgassing jet and its pressure profile. This model is used in many applications throughout this thesis. Most importantly it is used to create reactive torques on the comet nucleus changing it's rotational state, and it is used to provide insight into the dynamics of an orbiting spacecraft as it passes though an active outgassing jet. These applications allow for better trajectory fits as well as predictions for orbiting spacecraft.

Another contribution of this thesis is a method for estimating jet parameters using in-situ measurements. The method presented allows for the location, size, and outgassing acceleration of a jet to be estimated using only trajectory data and Doppler tracking. The identification of jet locations could ideally be compared to surface images to gain insight into surface features which produce jets and furthering our knowledge of the outgassing jet structure.

The next contribution of this thesis is to perform long-term predictions for the evolution of the comet's rotational state assuming multiple jets exist over a full range of insulation values. By parameterizing the comet's jet geometry into a single variable, averaged equations of motion uncover secular drifts in the rotational axis of the comet caused by jet reactive torques. In addition to uncovering the secular drifts for a fixed jet geometry, variable jet geometry is allowed to explore the evolution for a more realistic comet model over long time spans.

The final major contribution is identification of stable Sun synchronous circular

orbits about a comet perpendicular to the Sun line in a rotating frame under perturbations by solar radiation pressure. These orbits are offset from the comet center of mass. The stability of these families of circular orbits is explored by zero velocity curves as well as analytically through spectral analysis of linearized equations.

CHAPTER II

Comet Model Description

To study the effects of outgassing jets on an orbiting spacecraft as well as the effects of the reactive torque on the rotation state of the comet body itself, a model of the comet body and the outgassing jets located on it's surface is necessary. Since the comet nucleus and its environment are complex systems, assumptions on the characteristics of the comet body and the outgassing jet geometry will be made as simplifications to the true comet properties. This chapter will define and explore the outgassing jet model that will be utilized throughout this work.

2.1 Comet Nucleus Model

Although the focus of this research is on the outgassing jet, the body of the comet needs to be defined before the jet model can be considered. The model for the jet presented allows for an arbitrarily shaped comet body, it is assumed that the comet nucleus is modelled as an ellipsoid with principle half lengths, a, b, and c. In general, we assume that the body rotates with constant rotation rate, ω, about the z-axis (aligned along the c principle half length) in a body fixed frame which may be inclined to the comet's orbital plane. This principle axis rotation assumption is modified for the analysis of the reactive torques produced on the comet body by

the outgassing jets to be presented in a later chapter. The mass distribution of the comet is assumed to be uniform and the gravitational field for a homogenous ellipsoid which has been described in Scheeres [15] will be used for this comet model. For an ellipsoid with equal principle half lengths, the model collapses to the special case of a sphere which yields a point mass gravity field. This comet model, as mentioned, is only an approximation to a true comet body which is more irregularly shaped and may have nonhomogeneous mass distributions[16][17].

In general, it is assumed that the comet is located significantly far from any other major celestial body such that the spacecraft's motion about the comet follows the standard two-body orbital equations. Other equations of motion for the comet and spacecraft will be considered as appropriate and presented in a later chapter. The mass of the spacecraft is assumed to be negligible relative to the mass of the comet. Based on these assumptions, the equations of motion take the form:

$$\ddot{\vec{r}} = \frac{\partial U}{\partial \vec{r}} + \vec{a}_p, \tag{2.1}$$

where $\vec{r}$ is the spacecraft's inertial position vector relative to the comet's center of mass, U is the comet's gravitational force potential, and $\vec{a}_p$ is the acceleration that the spacecraft feels from the outgassing jet. This jet outgassing acceleration is defined according to the jet model and is discussed in more detail in the next section.

2.2 Outgassing Jet Model

In the simplest model, the outgassing field around the comet is assumed to be produced by a single discrete jet located on the surface of the comet. More complicated models assume that the outgassing field is produced by multiple jets of varying strengths distributed across the surface of the comet nucleus. The single jet

case is presented here. Multiple jets are modelled as copies of a single jet with varied parameters.

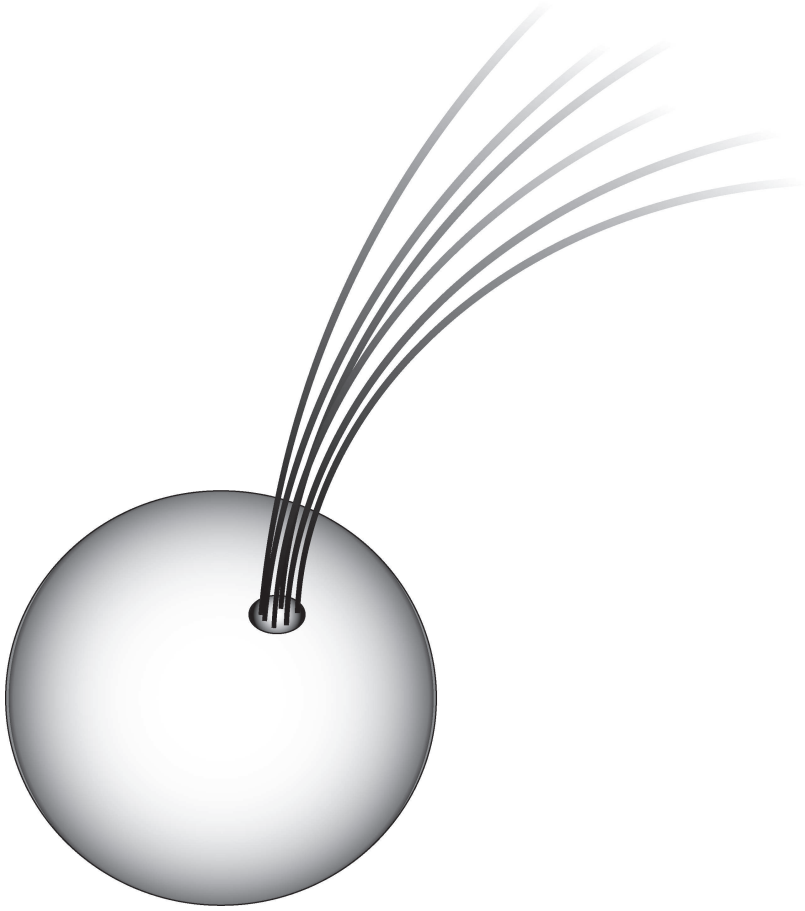

Figure 2.1: Outgassing Jet Illustration.

The jet is assumed to be fixed on the comet's surface with its center located at a radius from the center of the comet nucleus, r_0, a longitude of ϕ_0, and a latitude of λ_0 in the comet body fixed frame. The active region on the surface of the comet is assumed to have a circular cross section which is defined by the size and shape of the jet by a constant half angle, δ, and radius on the surface , r_p. For the purposes of this work, these jet parameters remain constant over time (including multiple perihelion passages) although realistically the jet geometry may change as a result of surface topological changes due to sublimation or other processes over long time spans. The

outgassing is modelled as a constant gas velocity, V_{og}, away from the comet surface in a direction defined by the jet's orientation which may point in any arbitrary direction away from the comet surface. The constant velocity is a reasonable approximation above one mean comet radius altitude while this assumption may not hold close to the comet surface where complex gas dynamics and interactions can occur [18]. The simplest model used assumes that the orientation of the jet is the outward normal to the surface at the jet location although arbitrary orientations are occasionally used. In general, the spacecraft orbits do not interact with the jets close to the surface, therefore the constant velocity assumption holds for the trajectories considered in this research.

To begin describing the three-dimensional geometry of the jet, we start with the centerline of the outgassing jet which passes through the center of the jet at the surface as defined above. The centerline is defined as a function of time since ejection, s, and can be expressed in the comet body fixed frame (illustrated in Figure 2.2) as:

$$\vec{r}_{og}(s) = r_0 \hat{e}_{r_{surf}} + V_{og} s \hat{e}_{r_{jet}}, \tag{2.2}$$

where $\vec{e}_{r_{surf}}$ is the body fixed unit vector pointing from the center of the comet to the jet surface point in the radial direction and $\vec{e}_{r_{jet}}$ is the body fixed unit vector pointing in the jet orientation direction.

As previously mentioned, the comet body fixed frame is assumed, for now, to rotate at a constant rate, ω, with the comet nucleus and is transformed from $(\hat{x}, \hat{y}, \hat{z})$, the non-rotating coordinate system with $\hat{z}$ aligned along the spin axis of the comet, to the body fixed coordinate frame, $(\hat{x}_b, \hat{y}_b, \hat{z}_b)$, by the rotation matrix, $R(t)$.

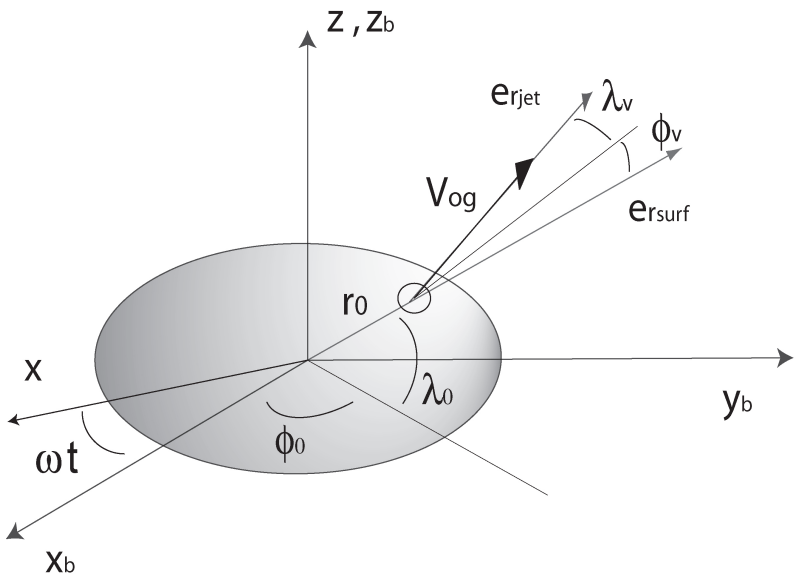

Figure 2.2: Coordinate Frames

$$R(t) = \begin{bmatrix} \cos(\lambda_0)\cos(\phi_0+\omega t) & \cos(\lambda_0)\sin(\phi_0+\omega t) & \sin(\lambda_0) \\ -\sin(\phi_0+\omega t) & \cos(\phi_0+\omega t) & 0 \\ -\sin(\lambda_0)\cos(\phi_0+\omega t) & -\sin(\lambda_0)\sin(\phi_0+\omega t) & \cos(\lambda_0) \end{bmatrix}. \tag{2.3}$$

Therefore, the outgassing jet centerline, $\vec{r}_{og}$, can be expressed as a function of both the time, t, and the time since ejection, s, in the non-rotating inertial frame, $(\hat{x}, \hat{y}, \hat{z})$, using the rotation matrix, $R(t)$.

$$\vec{r}_{og}(t,s) = R(t)^T \left[r_0 \hat{e}_{r_{surf}} + V_{og} s \hat{e}_{r_{jet}} \right]. \tag{2.4}$$

A second rotation matrix is used to transform this inertial frame to a frame corresponding to the comet's heliocentric orbit. This calculation will not be presented here as it is a common transformation and can be found in any orbital mechanics textbook. Since a circular cross section is assumed for the jet, the surface of the outgassing jet is modelled as a curved cone that is defined by the constant half

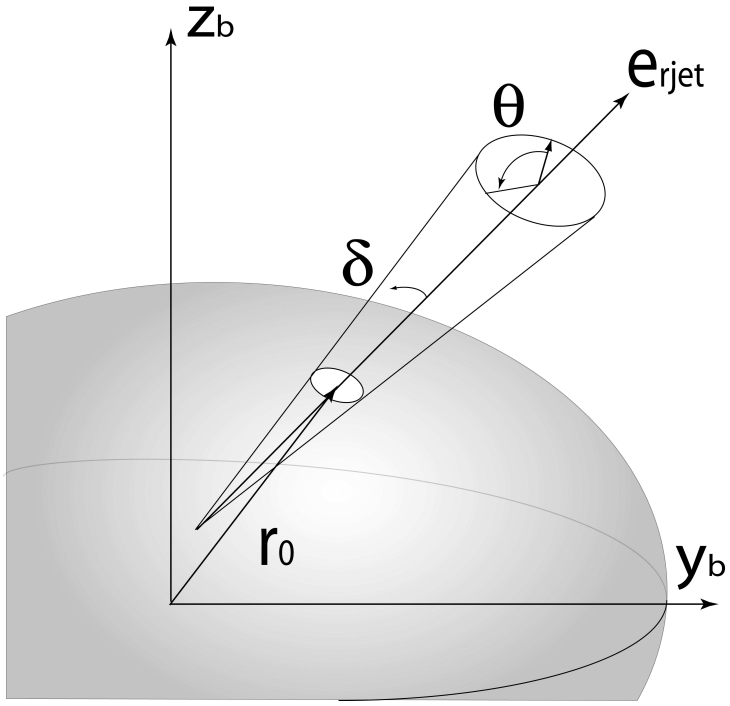

Figure 2.3: Outgassing Jet Surface

angle, δ, from the jet centerline as well as the time since ejection in the body fixed frame. The radius of the cross section at the surface of the comet, r_p, completes the geometric description of the outgassing jet by defining a virtual origin of the jet centerline which in general will not coincide with the center of the comet's nucleus and may actually reside outside the comet body. Figure 2.3 illustrates the geometry of the jet surface. Note that the cone will curve as the comet body rotates and that the half angle of the jet may diverge at large distances from the surface of the comet.

The geometric description only provides part of the full outgassing jet model. To complete the model, the outgassing pressure field needs to be considered and defined. The jet generates a pressure field which is a function of the mass ejection rate per unit area, Q_j, of the jet at the surface of the comet and the velocity of the material being ejected, V_{og}. The pressure of the outgassing at the surface of the comet, p_0, is

defined as:

$$p_0 = Q_j V_{og}. \tag{2.5}$$

The velocity field is assumed to be uniformly outwards in the direction of the jet's orientation at the time of ejection, therefore a vector pressure aligned with the velocity field can be defined as:

$$\vec{p_0} = Q_j V_{og} \hat{e}_{r_{jet}}. \tag{2.6}$$

This mass ejection rate, Q_j, is estimated as [11]:

$$Q_j = S f(\theta_{sun}) g(r_s) Q_*, \tag{2.7}$$

where Q_* is the mass ejection rate of a plane with an area equal to the surface area of the comet perpendicular to the Sun at a distance of 1 AU away, S is the relative intensity of the jet with respect to Q_* defined by the jet's active area relative to the comet's surface area, θ_{sun} is the angle between the a unit vector in the direction of the Sun and the orientation vector of the outgassing jet, and r_s is the heliocentric distance of the comet.

This mass ejection rate is not constant but is dependent on the distance from the Sun as well as if the jet is sunlit or in darkness. As the comet travels closer to the Sun its thermal activity will increase as a function of r_s yielding an outgassing strength empirically determined by Marsden et al.[19] to follow the law:

$$g(r_s) = g_0 \left(\frac{r_s}{r_{s0}} \right)^{-c_1} \left[1 + \left(\frac{r_s}{r_{s0}} \right)^{c_2} \right]^{-c_3}, \tag{2.8}$$

where $c_1 = 2.15$, $c_2 = 5.093$, $c_3 = 4.6142$, $r_{s0} = 2.808$, and $g_0 = 0.111262$. The function $f(\theta_{sun})$ provides a relationship for the strength of the pressure at the surface of the comet as it is related to the angle the Sun makes with the orientation of the jet. If the unit vector pointing towards the Sun is defined as $\hat{u}_s$, then $\cos\theta_{sun} =$

$\hat{u}_s \cdot \hat{r_{og}}(t,s)$. Neishdadt et al.[11] uses the function $f(\theta_{sun}) = 1 - \alpha(1 - \cos\theta_{sun})$ with a restriction of $\alpha \leq 1/2$, and therefore $f(\theta_{sun})$ never takes on a value of 0 in their theory. A conditional function $f(\theta_{sun})$ provides for a stronger pressure when the surface is illuminated by the Sun and a weak (possibly zero) pressure when it is not, such that

$$f(\theta_{sun}) = \max \begin{cases} 0 \\ 1 - \alpha(1 - \cos\theta_{sun}) \end{cases} \tag{2.9}$$

The parameter α is related to the thermal inertia, and can take on any numerical value of α such that $0 \leq \alpha \leq 1$. Note that if $\alpha \leq 1/2$, then the function simplifies to $f(\theta_{sun}) = 1 - \alpha(1 - \cos\theta_{sun})$ which is always greater than or equal to 0.

Note that this pressure vector described is for the pressure at the surface of the comet. The pressure magnitude felt by the orbiter will depend on it's radial distance from the comet's surface. It is assumed to be inversely proportional to its radial distance and will diminish as $1/|\vec{r_j}|^2$, where $\vec{r_j}$ is the spacecraft's position vector relative to the virtual center of the jet, illustrated in illustrated in Figure 2.3. Therefore, the pressure vector at the spacecraft is defined as:

$$\vec{p} = \vec{p_0} \left(\frac{r_0}{|\vec{r_j}|} \right)^2, \tag{2.10}$$

where $|\vec{r_j}| > r_0$ is assumed. The pressure is felt as an acceleration on the spacecraft from the outgassing, and takes the form:

$$\vec{a}_p = \frac{\vec{p}}{B} = \vec{p_0} \frac{1}{B} \left(\frac{r_0}{|\vec{r_j}|} \right)^2, \tag{2.11}$$

where B is the ratio of the mass of the spacecraft to the area of the spacecraft normal to the comet. Equation 2.11 provides the basis of the jet outgassing model and will be substituted into the spacecraft's equations of motion, equation 2.1.

2.3 Wild 2 Model

In 1999, NASA launched the Stardust spacecraft to rendezvous with the comet Wild 2. Wild 2 was chosen as the target of this mission due to the fact that it has a near original composition. Wild2 has only recently entered into our solar system with only a few perihelion passages meaning a large portion of its dust and volatiles have not been lost to sublimation processes[20].

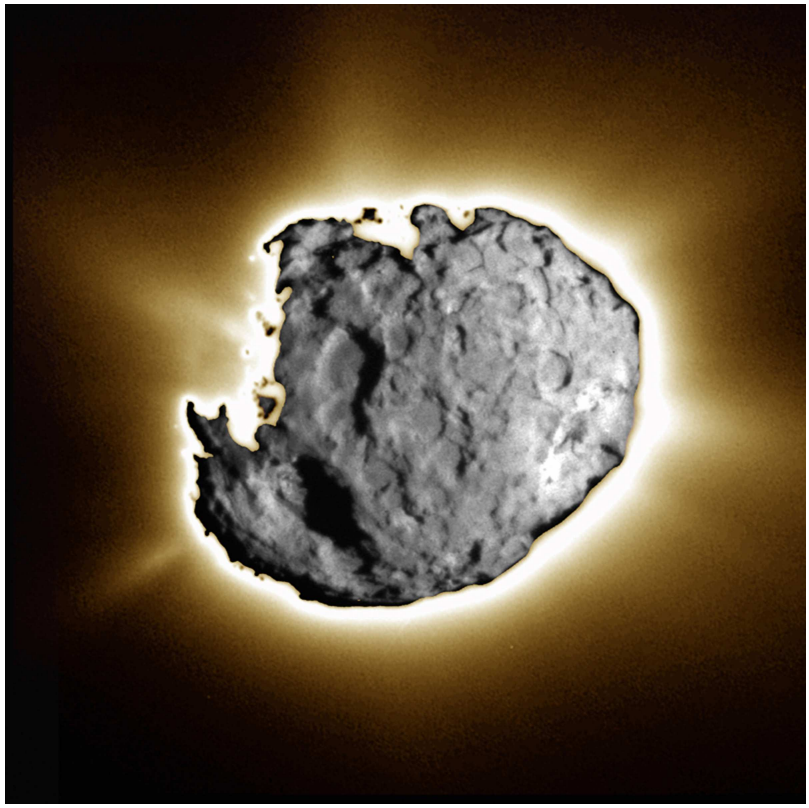

Figure 2.4: Composite Image Taken by the Navigation Camera During NASA's Stardust Jan 2, 2004 Flyby of Comet Wild2. Image from Jet Propulsion Laboratory[1].

During the 2001 fly by of the comet Wild 2, Stardust collected dust particles from the comet's coma and imaged the comet's nucleus. Sekanina et al.[6] enhanced long exposure images of the dust in the vicinity of the comet's nucleus to identify highly collimated columns of dust particles as jets ejecting material continuously from small

active patches on Wild2's surface as seen in figure 2.4.

Using a similar emission cone jet model to the one described in the previous section, the images were used to triangulate the locations and orientations of multiple jets that had been identified. Sekanina et al.[6] triangulated 20 jets emanating from the surface of Wild 2 with the locations and orientations listed in table 2.1 using a fitted triaxial ellipsoid with radii of 2.7 km, 1.9 km, and 1.5 km for the comet's nucleus.

Table 2.1: Wild2 Jet Locations and Orientations

	Orientation Angles *(degrees)*		Jet Location Angles *(degrees)*	
Jet	ψ_{or}	λ_{or}	ϕ_{loc}	λ_{loc}
α	161	4	169	1
β	−7	36	16	14
γ	25	26	38	13
δ	22	59	42	38
ϵ	−15	−20	353	−7
ζ	9	23	23	9
η	−65	3	294	2
θ	−130	4	238	2
κ	40	31	60	19
λ	30	47	45	28
μ	−59	56	266	43
ν	−49	57	260	43
ξ	20	25	27	10
π	34	17	45	9
ρ	−64	51	272	38
σ	97	49	95	36
τ	−101	53	252	39
ϕ	16	−10	14	−3
χ	16	−10	5	−3
ψ	1	−7	350	−2

Not surprisingly, most of the jets were determined to be located on the sunlit portion of Wild 2 with only two jets found to be emanating from the dark side. These two dark side jets imply that the comet has some thermal inertia which allows

for material to continue to sublimate after it is out of the direct view of the Sun or that those jets are driven by a more volatile gas. These 20 identified jets along with the fitted triaxial ellipsoidal for the Wild 2 nucleus will be modelled and used for simulation purposes in later chapters.

2.4 Summary

In support of a spacecraft mission to a comet, this chapter develops a simple cometary outgassing jet mathematical model for a single jet with constant half angle, δ, and constant outgassing velocity using a uniform ellipsoidal model of the comet nucleus. The pressure field created by the jet is constant across its profile with the magnitude inversely proportional to the square of the distance from the surface.

CHAPTER III

Comet Nucleus Complex Rotation

The model of the outgassing jets can be used for applications beyond determining the effects on an orbiting spacecraft or in estimation jet characteristics though jet encounters. In this chapter, it will be used to explore reactive torques on the comet body. Up to this point, the rotation of the comet nucleus has been assumed to be constant about a principal axis. Although there have been multiple claims of observations of comets spinning about a principal axis[23], these usually are only preliminary findings from light curves and cover only a handful of the comets in existence. Excited rotational states and tumbling motions of asteroids and comets has also been observed[24][25][26]. These reactive torques can produce a complex rotation state that causes the spin state to evolve slowly over time. Belton et al.[24] theorized that this was a possible reason for the changing periodicities seen for comet 2P/Encke. It will be this tumbling, or complex rotation, that will be the focus of this chapter. The need for a precise integration scheme which can handle both the complex motion as well as maintain accuracy over long time intervals will also be presented.

3.1 Rotational Equations of Motion

It is assumed that the comet is located significantly far from any other major celestial body such that the body follows the two-body orbital equations for motion about the Sun and the rotational dynamics are not significantly affected by gravitational torques. The comet body is assumed to follow the standard Euler equations for rigid body rotation. Since the comet body is assumed to be a constant density axially symmetric ellipsoid, these equations will be used in their principal axes formulation.

$$\mathbf{J} \cdot \dot{\vec{\omega}} + \vec{\omega} \times \mathbf{J} \cdot \vec{\omega} = \vec{M}, \tag{3.1}$$

$$\dot{\mathbf{R_t}} = \mathbf{R_t} \times \vec{\omega}, \tag{3.2}$$

where $\mathbf{J} \in \mathbf{R}^{3\times3}$ is the inertia matrix of the body, $\vec{M}, \vec{\omega} \in \mathbf{R}^3$ are the moment and angular velocity vectors, respectively, and $\mathbf{R_t}$ is the rotation matrix that defines the attitude with respect to inertial space. It is possible that comets (and asteroids) are comprised of larger mass concentrations which are held together through gravitational and spin forces[27]. For the purposes of this analysis, the comet body will be simplified to a biaxial ellipsoid with moments of inertia C and A (where $C > A$) and will not directly address any other type of mass distribution.

The rotational equations of motion for the comet will also be analyzed as appro-

priate using the equivalent form from [11]:

$$\frac{d\theta}{dt} = \frac{1}{L}[(M_{xb}\sin\psi + M_{yb}\cos\psi)\cos\theta - M_{zb}\sin\theta], \tag{3.3}$$

$$\frac{d\phi}{dt} = \frac{L}{A} - \frac{M_{xL}}{L}\cos\phi\cos\theta - \frac{M_{yL}}{L}(\cot\rho + \sin\phi\cot\theta), \tag{3.4}$$

$$\frac{d\psi}{dt} = L\cos\theta(\frac{1}{C} - \frac{1}{A}) + \frac{M_{xb}\cos\psi - M_{yb}\sin\psi}{L\sin\theta}, \tag{3.5}$$

$$\frac{d\rho}{dt} = \frac{M_{xL}}{L}, \tag{3.6}$$

$$\frac{d\sigma}{dt} = \frac{M_{yL}}{L\sin\rho}, \tag{3.7}$$

$$\frac{dL}{dt} = M_{zL}, \tag{3.8}$$

where θ is the nutation angle (the angle the angular momentum vector makes with the body fixed z-axis), where ψ is the precession angle and ϕ is the spin angle and completes the Euler Angle set with θ, L is the angular momentum magnitude, M_{xb}, M_{yb}, M_{zb} are the jets' reactive moment vector components in the comet principal axis body fixed frame, and M_{xL}, M_{yL}, M_{zL} are the same vector's components in a frame attached to the angular momentum vector. The orientation of the angular momentum vector with respect to the perihelion vector is ρ, the cone angle, and σ is the clock angle. Figure 3.1 illustrates the angular momentum vector's geometry with respect to the body fixed frame as well as the perihelion vector, $\hat{p}$.

With this set of variables, the coordinate transformation from the principle axis body fixed frame to the angular momentum frame is described by the matrix $\mathbf{m}$ and the coordinate transformation from the angular momentum frame to the inertial frame attached to the perihelion vector is described by the matrix $\mathbf{a}$.

$$\mathbf{m} = \begin{bmatrix} \cos\phi\cos\psi - \sin\phi\sin\psi\cos\theta & -\cos\phi\sin\psi - \sin\phi\cos\psi\cos\theta & \sin\phi\sin\theta \\ \sin\phi\cos\psi + \cos\phi\sin\psi\cos\theta & -\sin\phi\sin\psi + \cos\phi\cos\psi\cos\theta & -\cos\phi\sin\theta \\ \sin\psi\sin\theta & \cos\psi\sin\theta & \cos\theta \end{bmatrix}. \tag{3.9}$$

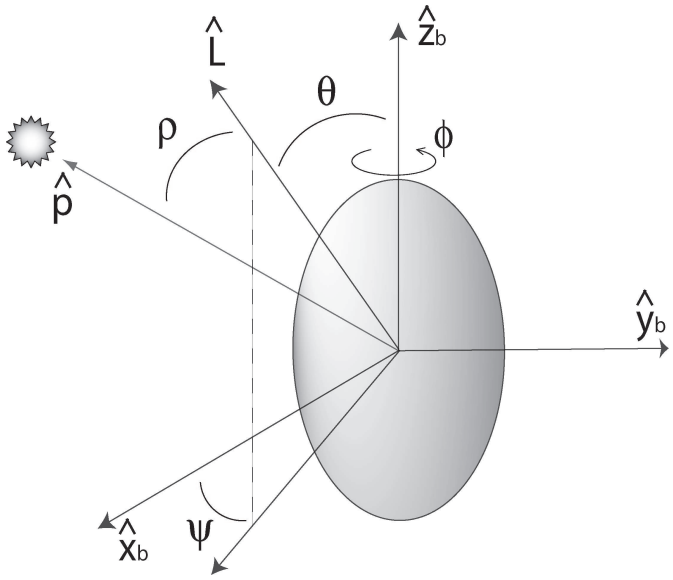

Figure 3.1: Angular Momentum Vector Geometry.

$$\mathbf{a} = \begin{bmatrix} \cos\sigma\cos\rho & -\sin\sigma & \cos\sigma\sin\rho \\ \sin\sigma\cos\rho & \cos\sigma & \sin\sigma\sin\rho \\ -\sin\rho & 0 & \cos\rho \end{bmatrix}. \tag{3.10}$$

The applied moments on the body are reactions to the discrete jets located in arbitrary positions on the surface. Previously, the outgassing jet model was defined using the following $f(\theta_{sun})$ function:

$$f(\theta_{sun}) = \max \begin{cases} 0, \\ 1 - \alpha(1 - \cos\theta_{sun}) \end{cases} \tag{3.11}$$

where α is related to the thermal inertia. Since the function $f(\theta_{sun})$ is a maximum function, it is instructive to approximate it for the purposes of this analysis of the reactive torques produced by discrete jets. To account for larger α values which would cause zero values of $f(\theta_{sun})$, the $f(\theta_{sun})$ function is approximated with a Fourier series for $\alpha > 1/2$, such that the function has a the form:

$$f(\theta_{sun}) \approx a_0 + \sum_{n=1}^{k} (a_n \cos(n\theta_{sun}) + b_n \sin(n\theta_{sun})), \tag{3.12}$$

where k is the number of terms used in the Fourier series and the coefficients, a_0 and a_n, are defined as:

$$a_0 = \frac{1}{2\pi}\int_{-\theta_m}^{\theta_m}(1-\alpha(1-\cos\theta))d\theta, \tag{3.13}$$

$$a_n = \frac{1}{\pi}\int_{-\theta_m}^{\theta_m}(1-\alpha(1-\cos\theta))\cos(n\theta)d\theta, \tag{3.14}$$

$$\theta_m = \cos^{-1}(1-(\frac{1}{\alpha})). \tag{3.15}$$

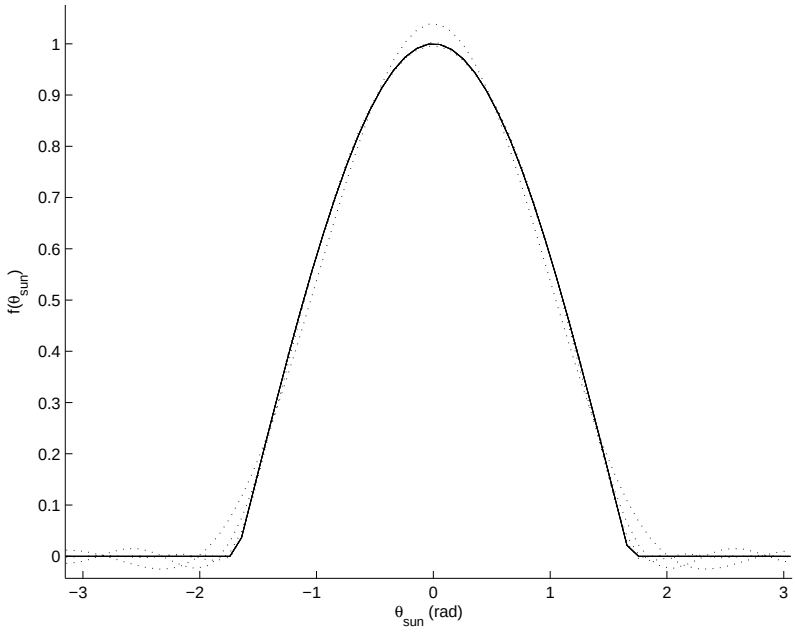

Figure 3.2: Fourier Series Approximation to the $f(\theta_{sun})$ Function with $\alpha = 0.8$ for 2, 5, 10, and 20 Terms. Solid = $f(\theta_{sun})$, Dotted = Fourier Series Approximations.

For this function, the coefficients b_n are identically 0. Figure 3.2 shows the Fourier series approximation to the $f(\theta_{sun})$ function for $0 \geq \alpha \geq 1$ with 2, 5, 10, and 20 terms used. The next order of approximation beyond the function used in Neishdadt et al.[11] is $k = 2$, which has the following form:

$$f(\theta_{sun}) \approx a_0 + a_1\cos\theta_{sun} + a_2\cos(2\theta_{sun}). \tag{3.16}$$

Using a trigonometric identity, the function can be rewritten in a more convenient

form as a polynomial of the variable $\cos(\theta_{sun})$:

$$f(\theta_{sun}) \approx (a_0 - a_2) + a_1 \cos\theta_{sun} + 2a_2 \cos^2\theta_{sun}. \tag{3.17}$$

Note that if $\alpha \leq 1/2$, this general function takes on the simpler form of $f(\theta_{sun}) = (a_0 - a_2) + a_1 \cos\theta_{sun}$ where $a_0 = 1$, $a_1 = \alpha$, and $a_2 = \alpha$ since it is no longer an approximation and yields the function used in [11]. Combining the parameters used in the jet model definition with the new $f(\theta_{sun})$ approximation, the net applied moment vector created by the outgassing jets, $\vec{M}$, has the form:

$$\vec{M} = -\sum_{j=1}^{N} S_j f(\theta_{sun}) g(r_s) Q_* (\vec{R}_j \times \vec{v}_j), \tag{3.18}$$

where N is the number of jets, $\vec{R}_j$ is the radius vector of the jet's center in the body fixed frame, and $\vec{v}_j$ is the outgassing velocity vector. Although the jet model allows for an arbitrary direction for the outgassing, this analysis will assume for simplicity that the outgassing velocity is in the outer normal direction to the ellipsoidal surface at the center location of the jet.

3.2 Averaged Equations

By averaging the equations of motion, insight can be gained into any long term changes in the comet's rotation state without needing to numerically integrate the full equations of motion. If it is assumed that there are no moments created by outgassing jets, $\vec{M} = \vec{0}$, then equations 3.3- 3.8 have the right hand side equal to zero or become constant rates such as:

$$\frac{d\phi}{dt} = \frac{L}{A}, \tag{3.19}$$

$$\frac{d\psi}{dt} = L\cos\theta\left(\frac{1}{C} - \frac{1}{A}\right). \tag{3.20}$$

Integrating these new equations would result in a constant precession of the spin axis of the comet nucleus about its angular momentum vector. This precession would also

be at constant nutation angle from the angular momentum vector. Since $d\phi/dt$ is constant, the spin rate of the nucleus body remains constant.

3.2.1 Averaging Over Orbit with $\alpha \leq 1/2$

When passing through perihelion the jets become active and apply a torque to the nucleus. If we assumed that the magnitudes of these torques are small, we can introduce an averaging approximation. To do this, we substitute the non-perturbed motion into the equations of motion and average the equations over the angles ϕ and ψ. Using $k = 1$ in the Fourier approximation which is appropriate for the $\alpha \leq 1/2$ case, then $f(\theta_{sun}) = a_0 + a_1 \cos\theta_{sun}$. The equations are first averaged over the nonperturbed nucleus motion (spin angle, ψ, and then precession angle, ϕ). The averaging performed uses the operator defined in equation 3.21.

$$\bar{y}(\psi, \phi, \nu) = \frac{1}{(2\pi)^2} \int_0^{2\pi} \int_0^{2\pi} y(\psi, \phi, \nu)) d\psi d\phi, \tag{3.21}$$

where y is a generic function. This averaging is possible due to the spin and precession rates being much larger in magnitude than the comet's mean motion. Note that if $a_0 = (1 - \alpha)$ and $a_1 = \alpha$, these averaged equations match the ones found in [11] for $\alpha \leq 1/2$ where special cases involving resonance between the two angles were discussed. Note that for an oblate body there will be no resonance between the angles in general because they will have different signs. First, the equations of motion are averaged over the comet rotation as described, yielding the following set

of averaged equations:

$$\frac{d\bar{\theta}}{dt} = \frac{g(r_s)\sin\bar{\theta}}{2\bar{L}}[3a_1D_1\cos\bar{\theta}(m_{Xz}\sin\nu + m_{Zz}\cos\nu) - 2a_0D_0], \quad (3.22)$$

$$\frac{d\bar{\rho}}{dt} = \frac{a_1 g(r_s)}{2\bar{L}}[D_2 m_{Xy}\cos\bar{\theta}\sin\nu + D_1 Rs(\bar{\theta})(m_{Xx}\sin\nu + m_{Zx}\cos\nu)], \quad (3.23)$$

$$\frac{d\bar{\sigma}}{dt} = \frac{a_1 g(r_s)}{2\bar{L}\sin\bar{\rho}}[D_1 Rs(\bar{\theta})m_{Xy}\sin\nu - D_2(m_{Xx}\sin\nu + m_{Zx}\cos\nu)\cos\bar{\theta}], \quad (3.24)$$

$$\frac{d\bar{L}}{dt} = -g(r_s)[a_1D_1Rs(\bar{\theta})(m_{Xz}\sin\nu + m_{Zz}\cos\nu) - a_0D_0\cos\bar{\theta}], \quad (3.25)$$

where

$$d_{jxb} = R_{jzb}v_{jyb} - R_{jyb}v_{jzb}, \quad (3.26)$$

$$d_{jyb} = R_{jxb}v_{jzb} - R_{jzb}v_{jxb}, \quad (3.27)$$

$$d_{jzb} = R_{jyb}v_{jxb} - R_{jxb}v_{jyb}, \quad (3.28)$$

$$Rs(\bar{\theta}) = \frac{1}{2}(2 - 3\sin^2\bar{\theta}), \quad (3.29)$$

$$D_0 = \sum_{j=1}^{N} S_j V_{og,j} d_{jzb}, \quad (3.30)$$

$$D_1 = \sum_{j=1}^{N} S_j V_{og,j} d_{jzb} v_{jzb}, \quad (3.31)$$

$$D_2 = \sum_{j=1}^{N} S_j V_{og,j}(d_{jyb}v_{jxb} - d_{jxb}v_{jyb}), \quad (3.32)$$

where $R_{jxb}, R_{jyb}, R_{jzb}$ are the comet body fixed components of $\vec{R}_j$, and $v_{jxb}, v_{jyb}, v_{jzb}$ are the comet body fixed components of $\hat{v}_j$. Note that D_0, D_1, and D_2 are related to the angular momentum projections in the body fixed frame and their signs determine alignment with the body fixed z-axis.

The second averaging of the equations of motion is over the comet's heliocentric motion (mean anomaly, M).

$$\overline{\bar{y}} = \frac{1}{2\pi}\int_0^{2\pi} \bar{y}(M)dM, \quad (3.33)$$

where

$$dM = \frac{(1-e^2)^{3/2} d\nu}{(1+e\cos\nu)^2}. \tag{3.34}$$

We will use the averaging operator with the defined transformation to average over the true anomaly:

$$\overline{\overline{x}} = \frac{(1-e^2)^{3/2}}{\pi} \int_0^\pi \frac{\bar{x}(\nu) d\nu}{(1+e\cos\nu)^2}. \tag{3.35}$$

This averaging will expose the long term secular drift in the variables. It is important to note that the function $g(r_s)$ is actually a function of the true anomaly, $g(r_s(\nu))$, and is accounted for in this averaging. Here the notation for the doubly averaged variables such as $\overline{\overline{x}}$ is suppressed to be x for notation simplicity.

$$\frac{d\theta}{dt} = \frac{1}{2L}[3a_1 D_1 \Phi_1 \cos\rho\cos\theta - 2a_0 D_0 \Phi_0]\sin\theta, \tag{3.36}$$

$$\frac{d\rho}{dt} = -\frac{\sin\rho}{4L} a_1 (2 - 3\sin\theta^2) D_1 \Phi_1, \tag{3.37}$$

$$\frac{d\sigma}{dt} = \frac{a_1}{2L}\cos\theta D_2 \Phi_1, \tag{3.38}$$

$$\frac{dL}{dt} = -\frac{1}{2}[a_1 D_1 \Phi_1 \cos\rho(2 - 3\sin\theta^2) - 2a_0 D_0 \Phi_0 \cos\theta], \tag{3.39}$$

where

$$\Phi_0 = \frac{(1-e^2)^{3/2}}{\pi} \int_0^\pi \frac{g(r(\nu)) d\nu}{(1+e\cos\nu)^2}, \tag{3.40}$$

$$\Phi_1 = \frac{(1-e^2)^{3/2}}{\pi} \int_0^\pi \frac{g(r(\nu))\cos\nu d\nu}{(1+e\cos\nu)^2}. \tag{3.41}$$

Equations 3.40 and 3.41 are discussed in more detail in [11].

3.2.2 Averaging Over Orbit with $\alpha > 1/2$

The previous solution for the averaged equations is only valid for $0 \leq \alpha \leq 1/2$. For $\alpha > 1/2$ the Fourier approximation of the $f(\theta_{sun})$ function has higher order terms. If $k = 2$, thus $f(\theta_{sun}) = a_0 + a_1\cos\theta_{sun} + a_2\cos(2\theta_{sun})$, the averaged equations

become:

$$\begin{aligned}
\frac{d\theta}{dt} &= \frac{1}{2L}(3a_1D_1\Phi_1\cos(\rho)\cos(\theta) - 2a_0D_0\Phi_0)\sin(\theta) \\
&+\frac{a_2\sin(\theta)}{32L}((D_0(11\Phi_0+\Phi_3) - 3D_3(\Phi_0+3\Phi_3) \\
&+(\Phi_0+3\Phi_3)((D_0-9D_3)\cos(2\rho) + (D_0-5D_3)\cos(2\theta)(1+3\cos(2\rho)) \\
&+2(\Phi_0-\Phi_3)(D_0-9D_3+3(D_0-5D_3)\cos(\theta))\cos(2\sigma)\sin(\rho)^2))), \qquad (3.42) \\
\frac{d\rho}{dt} &= \frac{\sin\rho}{4L}[-a_1(2-3\sin\theta^2)D_1\Phi_1 \\
&+2a_2\sin^2\theta(\Phi_3((D_0-D_3)\cos\theta\cos\rho(3+\cos(2\sigma)) \\
&-D_4\sin(2\sigma)) + \Phi_0(2(D_0-D_3)\cos\theta\cos\rho\sin^2\sigma + D_4\sin(2\sigma)))], \qquad (3.43) \\
\frac{d\sigma}{dt} &= \frac{1}{2L}[a_1\cos\theta D_2\Phi_1 - \frac{a_2}{4}(\Phi_3(D_4(1+3\cos(2\theta))\cos\rho(3+\cos(2\sigma)) \\
&-\cos\theta(D_3-1+(1-5D_3)\cos(2\theta))\sin(2\sigma)) \\
&+\Phi_0(2D_4(1+3\cos(2\theta))\cos\rho\sin^2\sigma \\
&-\cos\theta(1-D_3+(5D_3-1)\cos(2\theta))\sin(2\sigma)))], \qquad (3.44) \\
\frac{dL}{dt} &= -\frac{1}{2}[a_1D_1\Phi_1\cos\rho(2-3\sin\theta^2) - 2(a_0-a_2)D_0\Phi_0\cos\theta] \\
&+\frac{a_2\cos\theta}{4}[-\frac{1}{8}\Phi_3(D_0+3D_3+3(D_0-5D_3)\cos(2\theta)) \\
&(2+6\cos(2\rho) - 4\cos(2\sigma)\sin^2\rho) + \Phi_0(2D_3-3D_0-(D_0+10D_3)\cos(2\theta) \\
&+(D_0-3D_3+3(D_0+5D_3)\cos(2\theta))\sin^2\rho\sin^2\sigma)], \qquad (3.45)
\end{aligned}$$

where

$$\begin{aligned}
D_3 &= \sum_{j=1}^{N} S_jV_{og,j}d_{jzb}v_{jzb}^2, \qquad (3.46) \\
D_4 &= \sum_{j=1}^{N} S_jV_{og,j}(d_{jyb}v_{jxb} - d_{jxb}v_{jyb})v_{jzb}, \qquad (3.47) \\
\Phi_3 &= \frac{(1-e^2)^{3/2}}{\pi}\int_0^{\pi}\frac{g(r(\nu))\cos(2\nu)d\nu}{(1+e\cos\nu)^2}. \qquad (3.48)
\end{aligned}$$

Note that the additional term in the Fourier series approximation contributes an additional Φ_0 term to the averaged equations as well as a newly defined Φ_3 term. These averaged equations allow for better accuracy when modelling comets having a value of $\alpha > 1/2$. As higher order terms are included in the Fourier approximation to $f(\theta_{sun})$ additional integrals, Φ_k, and geometry combinations, D_k, will be needed.

3.2.3 Verification of Averaged Equations

To verify the averaged equations, numerically integrated rotational dynamics were compared to the analytical predictions of the averaged equations. To make a true comparison, the initial conditions of the averaged and the numerical cases need to be chosen to be consistent. Since the averaged equations may not start at the same numerical value as the full equations of motion at an arbitrary time, a small offset for the magnitude of the periodic part of the equations needs to be found to initialize the averaged equations consistently.

The full solution, $x(t)$, can be decomposed into secular and periodic parts.

$$x(t) = x_0 + \dot{\bar{x}}t + x_p(t), \tag{3.49}$$

where $x_p(t+T) = x_p(t)$ over one averaging interval. The periodic part of the equations of motion can be found as:

$$\dot{x}(x,t) = \dot{\bar{x}}(x) + \dot{x}_p(x,t), \tag{3.50}$$

where x_p is the periodic magnitude of a generic function, x, T is the period, $\dot{x}(t)$ is the equation of motion, and $\dot{\bar{x}}$ is the secular part of the equation of motion. In our approximation we will replace the state x in the equations of motion with the singly averaged state $\bar{x}$, but will only consider motion over one orbit period beyond this state. Note that since $\dot{x}_p(t)$ is periodic then $\dot{x}(t+T) = \dot{\bar{x}} + \dot{x}_p(t+T) = \dot{\bar{x}} + \dot{x}_p(t)$.

Table 3.1: Simulation Parameters

Variable	Description	Value	Unit
a	comet principal half length	3	km
b	comet principal half length	3	km
c	comet principal half length	6	km
δ	jet shape half angle	1.5	degree
r_p	cross section radius at surface	50	m
Q_*	mass ejection rate	3.4×10^6	kg/hr
a	comet orbit semi-major axis	3.44	AU
e	comet orbit eccentricity	0.54	-
i	comet orbit inclination	3.24	deg

Q_* assumed to be same as comet Wirtanen.

To find the mean value of the periodic part over a single period, equation 3.50 is rearranged and integrated.

$$x_p(t) = \int_0^t (\dot{x}(\bar{x}, \tau) - \dot{\bar{x}}) d\tau. \tag{3.51}$$

$$\bar{x}_p = \frac{1}{T} \int_0^T x_p(t) dt. \tag{3.52}$$

Since our equations are functions of true anomaly, ν, the periodic magnitude can be written in terms of ν instead of time.

$$\bar{x}_p = \frac{(1-e^2)^3}{2\pi\sqrt{a}} \int_0^{2\pi} \frac{1}{(1+e\cos\nu)^2} \left[\int_0^{\nu} \frac{\dot{x}(\nu') d\nu'}{(1+e\cos\nu')^2} \right] d\nu - \frac{T}{2}\dot{\bar{x}}. \tag{3.53}$$

Integrating these periodic magnitudes for the nutation angle, cone angle and angular momentum magnitude produces offsets to the original conditions which give a more realistic averaged value for the simulated data. The generic function x is replaced with the rotational equations of motion to find the needed initial offset.

For the verification, simulations were performed for a prolate ellipsoid comet nuclei with constant density and various values of α. The "truth model" used to verify the averaged equations is a variational integration of the full rotational equations (see

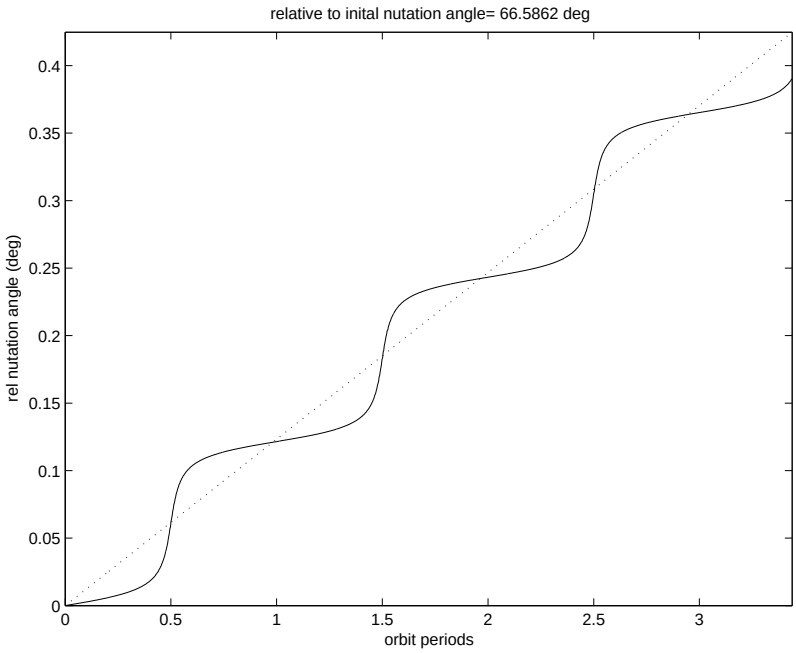

Figure 3.3: Relative Nutation Angle Comparison. Solid = Equations of Motion, Dotted = Averaged Equations for $\alpha > 1/2$ (With Periodic Magnitude Offset).

Appendix for description and algorithm used) as it has been verified to conserve the angular momentum and energy in the absence of torques[28]. Twenty randomly located jets were added to the surface with their outgassing oriented to the outward normal to the surface. The orbit defined in Table 3.1 was assumed. As seen in Figures 3.3- 3.5 for a prolate body with $\alpha = 0.7$, the cone angle, nutation angle, and angular momentum magnitude are nicely approximated by the averaged equations over several orbits. In the figures, the solid lines are the numerically integrated solution and the dotted lines are the $\alpha > 1/2$ averaged equations. It is important to note that these averaged equations may not be valid for long periods of time since changes in jet activity (new jets becoming active or others becoming dormant) are not modelled. The averaged equations assume that the active jets and their geometry are always the same for now.

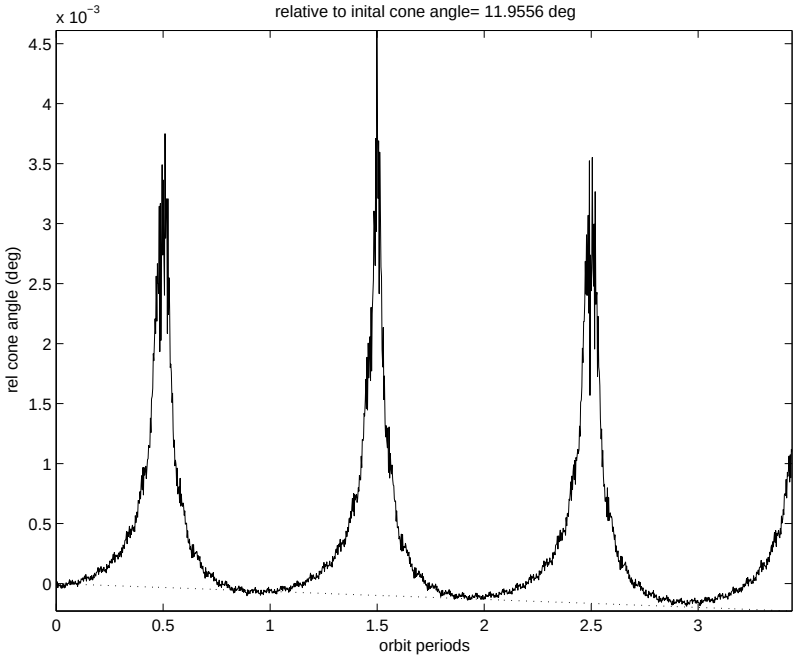

Figure 3.4: Relative Cone Angle Comparison. Solid = Equations of Motion, Dotted = Averaged Equations for $\alpha > 1/2$ (With Periodic Magnitude Offset).

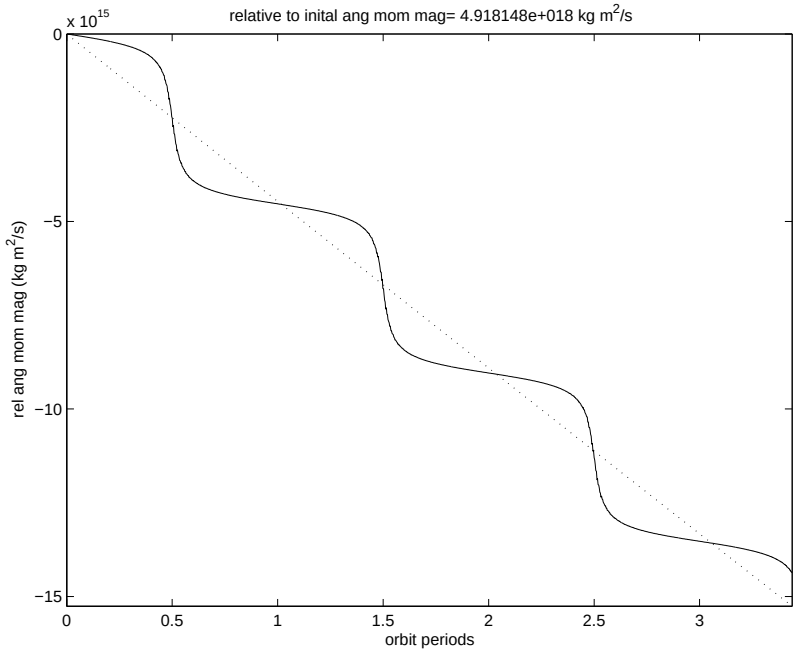

Figure 3.5: Relative Angular Momentum Magnitude Comparison. Solid = Equations of Motion, Dotted = Averaged Equations for $\alpha > 1/2$ (With Periodic Magnitude Offset).

3.2.4 Analysis of the Averaged Equations

The drift in the rotational state is captured by the averaged equations and therefore can be used to predict the behavior of the comet over time. It is useful to construct a flow field for the nutation and cone angles such as the one in figure 3.6. This figure can give the direction and relative magnitude change in these two rotation state parameters as well as the angular momentum magnitude change for any starting rotation state.

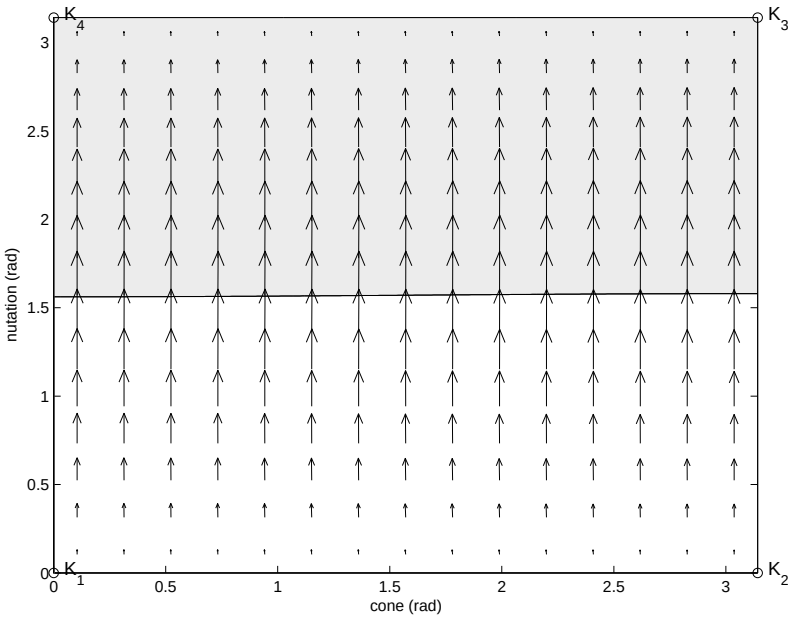

Figure 3.6: Nutation and Cone Angle Flow Field. Shaded = Angular Momentum Decreasing, Nonshaded = Angular Momentum Increasing.

Using the averaged equations for $\alpha \leq 1/2$ in [11], define a variable, κ, which is a function of the jet geometry through variables D_1 and D_0 and the comet's orbit through the variables Φ_1 and Φ_0, such that

$$\kappa = \frac{D_0 \Phi_0}{D_1 \Phi_1}. \tag{3.54}$$

It is important to note that κ is constant once the orbit and the jet geometry are determined and does not vary with time since the jet geometry is assumed to be

fixed. If $\alpha > 1/2$, then performing this transformation on the averaged equations produces variables of the form:

$$\kappa_{i,j} = \frac{D_i \Phi_j}{D_1 \Phi_1}, \tag{3.55}$$

where $i = 0, 1, 2, 3$ and $j = 0, 1, 2, 3$ and the combination of $i = 0$ and $j = 0$ is the original κ variable. These $\kappa_{i,j}$ will not be used in this analysis but are provided for completeness. Performing a change of variable for the $\alpha \leq 1/2$ averaged equations in the nutation and cone angle averaged equations results in a new set of simplified equations:

$$\frac{d\theta}{dt*} = \frac{D_1}{2}[3\alpha \cos\rho \cos\theta - 2(1-\alpha)\kappa] \sin\theta \tag{3.56}$$

$$\frac{d\rho}{dt*} = -\frac{\alpha \sin\rho}{4}(2 - 3\sin\theta^2) D_1 \tag{3.57}$$

where

$$t* = \frac{\Phi_1}{L} t. \tag{3.58}$$

The rotation state parameters θ and ρ are now only functions of D_1 and κ. Equilibrium points for this system can be found as a function of κ alone. For any κ value, there exist at least four equilibrium points which are located at the vertices of the square $K = [0 \leq \rho \leq \pi, 0 \leq \theta \leq \pi]$, $K_1 = (0, 0)$, $K_2 = (\pi, 0)$, $K_3 = (\pi, \pi)$, and $K_4 = (0, \pi)$. If $\kappa > \kappa_1 = 3\alpha/2(1-\alpha)$, where $\kappa > 0$ and $D_1 > 0$ is assumed, the point K_1 is stable, K_3 is unstable, and K_2 and K_4 are saddle points. Figure 3.7 is the flow field of the nutation and cone angles where these points can be seen.

If $\kappa = \kappa_1$, a bifurcation of the equilibrium points occurs creating two new equilibrium points, M_1 and M_2, where

$$M_1 = (0, \arccos\frac{\kappa}{\kappa_1}), \tag{3.59}$$

$$M_2 = (\pi, \pi - \arccos\frac{\kappa}{\kappa_1}). \tag{3.60}$$

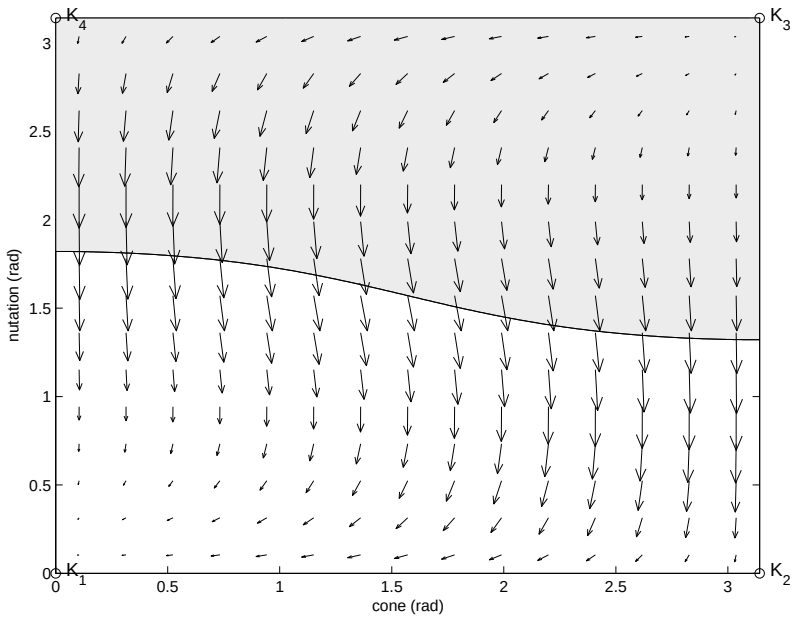

Figure 3.7: Nutation and Cone Angle Flow Field for $\kappa > \kappa_1 = 3\alpha/2(1-\alpha)$. K_1 and K_3 Are Stable and Unstable Nodes with All Other Points Being Saddle Points. Shaded = Angular Momentum Decreasing, Nonshaded = Angular Momentum Increasing.

For $\kappa_1 > \kappa > \kappa_2 = \kappa_1/\sqrt{3}$, these two equilibrium points become the stable and unstable nodes for the system, respectively, while the points K_i all become saddle points of the system, illustrated in figure 3.8.

If $\kappa = \kappa_2$, another bifurcation of the equilibrium points occurs creating two new equilibrium points, N_1 and N_2, where.

$$N_1 = (\arccos\frac{\kappa\sqrt{3}}{\kappa_1}, \arccos\frac{1}{\sqrt{3}}), \tag{3.61}$$

$$N_2 = (\pi - \arccos\frac{\kappa\sqrt{3}}{\kappa_1}, \pi - \arccos\frac{1}{\sqrt{3}}). \tag{3.62}$$

For $\kappa_2 > \kappa > \kappa_3 = \kappa_1\sqrt{2}/3$, these two equilibrium points become the stable and unstable nodes for the system, respectively, while the points K_i and M_i all become saddle points, illustrated in figure 3.9. If $\kappa_3 > \kappa > 0$, the points N_1 and N_2 become stable and unstable foci, respectively, spiraling into or away from the points, shown in figure 3.10. For the degenerate case of $\kappa = 0$, N_1 and N_2 become centers of the

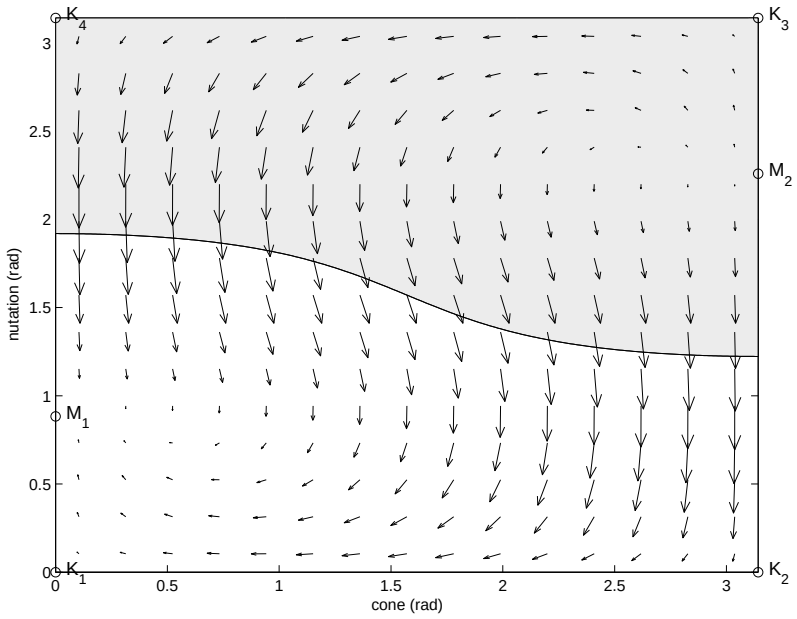

Figure 3.8: Nutation and Cone Angle Flow Field for $\kappa_1 > \kappa > \kappa_2 = \kappa_1/\sqrt{3}$. M_1 and M_2 Are Stable and Unstable Nodes with All Other Points Being Saddle Points. Shaded = Angular Momentum Decreasing, Nonshaded = Angular Momentum Increasing.

system illustrated in figure 3.11. This case arises if $D_0 = 0$ but $D_1 \neq 0$. A summary of these results can be seen in table 3.2.

For all $\kappa > 0$, the angular momentum is increasing as the system reaches the stable equilibrium. It is interesting to note the behavior of the system when κ, D_0, or D_1 changes signs. When κ becomes negative (either D_0 or D_1 is negative), the stable and unstable equilibrium points "switch sides" and the angular momentum is decreasing as the system reaches the stable equilibrium. M_1 becomes closer to a nutation angle of π and M_2 becomes closer to a nutation angle of 0 when they exist. N_1 and N_2 show a similar behavior with N_1 becoming closer to a cone angle of π and N_2 becomes closer to a cone angle of 0 when they exist. When it is D_0 that causes κ be negative, the flow direction changes from N_1 to N_2 when they exist. Figure 3.12 illustrates this case. If N_1 and N_2 do not exist, then there is no flow change. When

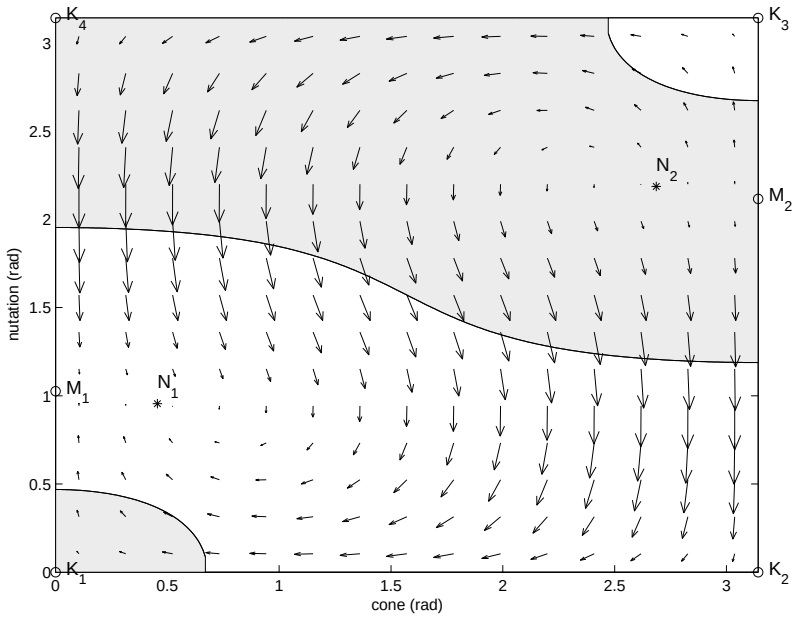

Figure 3.9: Nutation and Cone Angle Flow Field for $\kappa_2 > \kappa > \kappa_3 = \kappa_1\sqrt{2}/3$. N_1 and N_2 Are Stable and Unstable Nodes with All Other Points Being Saddle Points. Shaded = Angular Momentum Decreasing, Nonshaded = Angular Momentum Increasing.

it is D_1 that causes κ be negative, the flow direction changes from M_1 to M_2 when they exist. If both D_0 and D_1 are negative resulting in a positive κ value, the flow direction changes for both M_1 and M_2 and N_1 and N_2 , but the parameters do not "switch sides". A summary of these results can be seen in table 3.3 where $M_{1\rho} = 0$, $M_{1\theta} = \arccos(\kappa/\kappa_1)$,$M_{2\rho} = \pi$, $M_{2\theta} = \pi - \arccos\frac{(}{\kappa}/\kappa_1)$, $N_{1\rho} = \arccos(\kappa\sqrt{3}/\kappa_1)$, $N_{1\theta} = \arccos(1/\sqrt{3})$, $N_{2\rho} = \pi - \arccos(\kappa\sqrt{3}/\kappa_1)$, and $N_{2\theta} = \pi - \arccos(1/\sqrt{3})$.

The flow field constructed using the averaged equations with $\alpha > 1/2$ are qualitatively similar although they are slightly different quantitatively, as expected. To reproduce this analysis on the Fourier approximated equations would produce more κ type variables adding to the complexity of the analysis without adding significantly to the results as the trends in drift are similar.

Table 3.2: Summary of Stability Results for $\kappa > 0$ and $D_1 > 0$

eq.pt.	$\kappa > \kappa_1$	$\kappa_1 > \kappa > \kappa_2$	$\kappa_2 > \kappa > \kappa_3$	$\kappa_3 > \kappa > 0$	$\kappa = 0$
K_1	stable	saddle	saddle	saddle	saddle
K_2	saddle	saddle	saddle	saddle	saddle
K_3	unstable	saddle	saddle	saddle	saddle
K_4	saddle	saddle	saddle	saddle	saddle
M_1	dne	stable	saddle	saddle	saddle
M_2	dne	unstable	saddle	saddle	saddle
N_1	dne	dne	stable	stable focus	center
N_2	dne	dne	unstable	unstable focus	center

Table 3.3: Summary of Kappa Flows

κ	D_0	D_1	$\dot{L}_\infty$	κ value	Flow
				$\lvert\kappa\rvert > \kappa_1$	$K_3 \to K_1$
$+$	$+$	$+$	$+$	$\kappa_1 > \lvert\kappa\rvert > \kappa_2$	$M_2 \to M_1$
				$\kappa_2 > \lvert\kappa\rvert > 0$	$N_2 \to N_1$
				$\lvert\kappa\rvert > \kappa_1$	$K_1 \to K_3$
$+$	$-$	$-$	$+$	$\kappa_1 > \lvert\kappa\rvert > \kappa_2$	$M_1 \to M_2$
				$\kappa_2 > \lvert\kappa\rvert > 0$	$N_2 \to N_1$
				$\lvert\kappa\rvert > \kappa_1$	$K_2 \to K_4$
$-$	$-$	$+$	$+$	$\kappa_1 > \lvert\kappa\rvert > \kappa_2$	$(M_{2\rho}, \pi - M_{2\theta}) \to (M_{1\rho}, \pi - M_{1\theta})$
				$\kappa_2 > \lvert\kappa\rvert > 0$	$(\pi - N_{1\rho}, N_{1\theta}) \to (\pi - N_{2\rho}, N_{2\theta})$
				$\lvert\kappa\rvert > \kappa_1$	$K_4 \to K_2$
$-$	$+$	$-$	$-$	$\kappa_1 > \lvert\kappa\rvert > \kappa_2$	$(M_{1\rho}, \pi - M_{1\theta}) \to (M_{2\rho}, \pi - M_{2\theta})$
				$\kappa_2 > \lvert\kappa\rvert > 0$	$(\pi - N_{2\rho}, N_{2\theta}) \to (\pi - N_{1\rho}, N_{1\theta})$

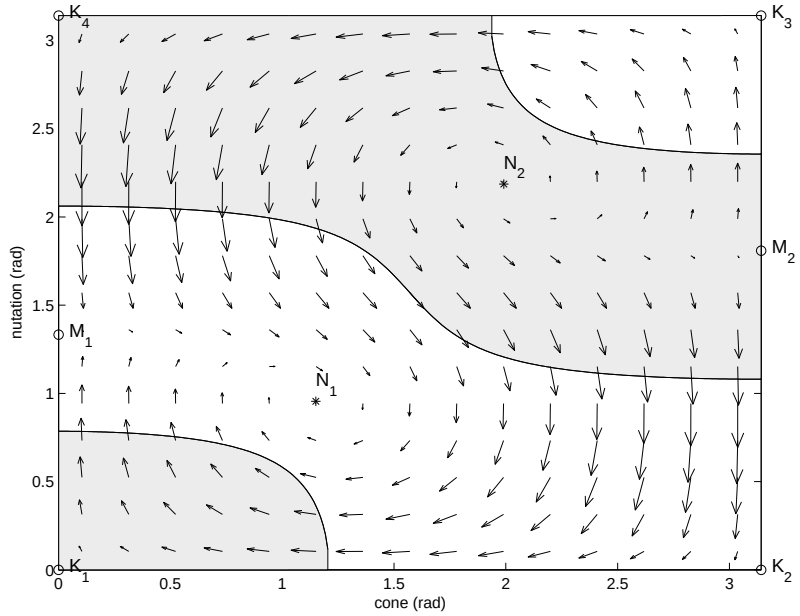

Figure 3.10: Nutation and Cone Angle Flow Field for $\kappa_3 > \kappa > 0$. N_1 and N_2 Are Stable and Unstable Nodes with All Other Points Being Saddle Points. Shaded = Angular Momentum Decreasing, Nonshaded = Angular Momentum Increasing.

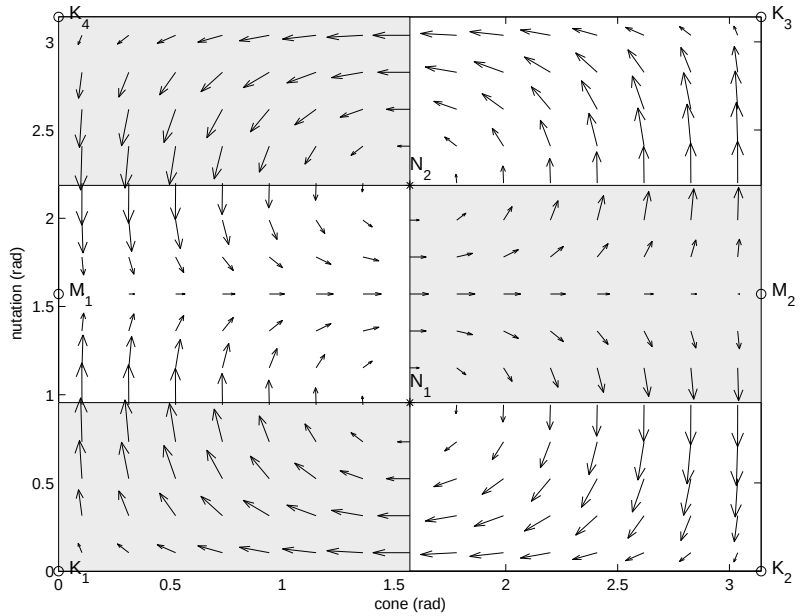

Figure 3.11: Nutation and Cone Angle Flow Field for $\kappa = 0$. N_1 and N_2 Are Stable and Unstable Nodes with All Other Points Being Saddle Points. Shaded = Angular Momentum Decreasing, Nonshaded = Angular Momentum Increasing.

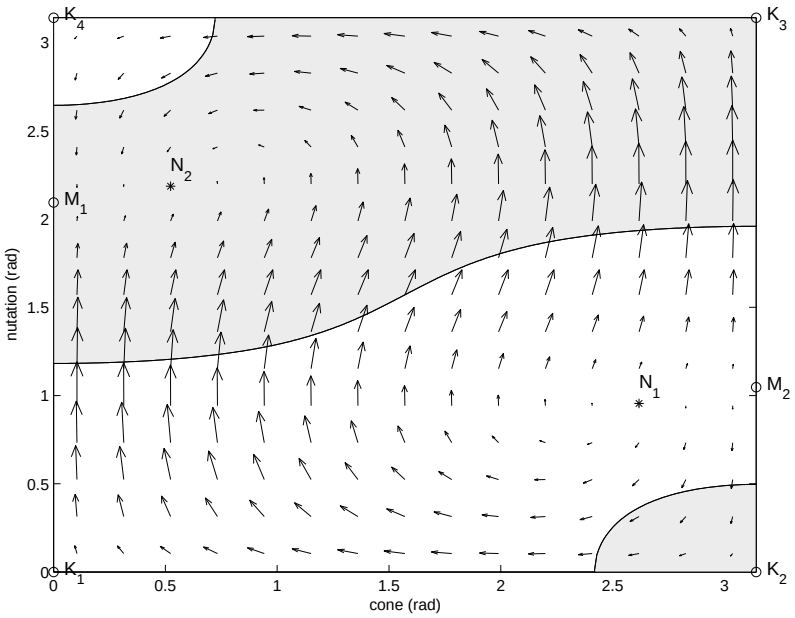

Figure 3.12: Nutation and Cone Angle Flow Field for $\kappa_2 > |\kappa| > \kappa_3 = \kappa_1\sqrt{2}/3$ and $D_0 < 0$. N_1 and N_2 Are Stable and Unstable Nodes with All Other Points Being Saddle Points. Shaded = Angular Momentum Decreasing, Nonshaded = Angular Momentum Increasing.

3.3 Applications of the Averaged Equations

The evolution of the comet's rotation state directly depends on it's κ value. Varying the κ value slowly over time can simulate changes in the jet geometry or in the comet's heliocentric orbit. It is therefore instructive to explore the distribution of κ for randomly placed jets. Multiple runs calculating the value of κ were performed randomly distributing 1, 20, 50, and 100 identically sized jets across a comet's surface. Figures 3.13- 3.15 shows that there is a peak of κ values which falls below κ_3. The negative κ values correspond to either a negative D_0 or D_1 value. Note that the false peaks in the ± 20 bins is from lumping κ values with $|\kappa| > 20$ into those bins. Figure 3.16 shows that for a single jet on the surface of the comet body, a κ value of $|\kappa| < \Phi_0/\Phi_1$ is not possible. Since, κ is proportional to $1/v_{jzb}$ for a single jet, the smallest value $1/v_{jzb}$ can hold is 1, the case where the jet is oriented along the body-fixed z-axis.

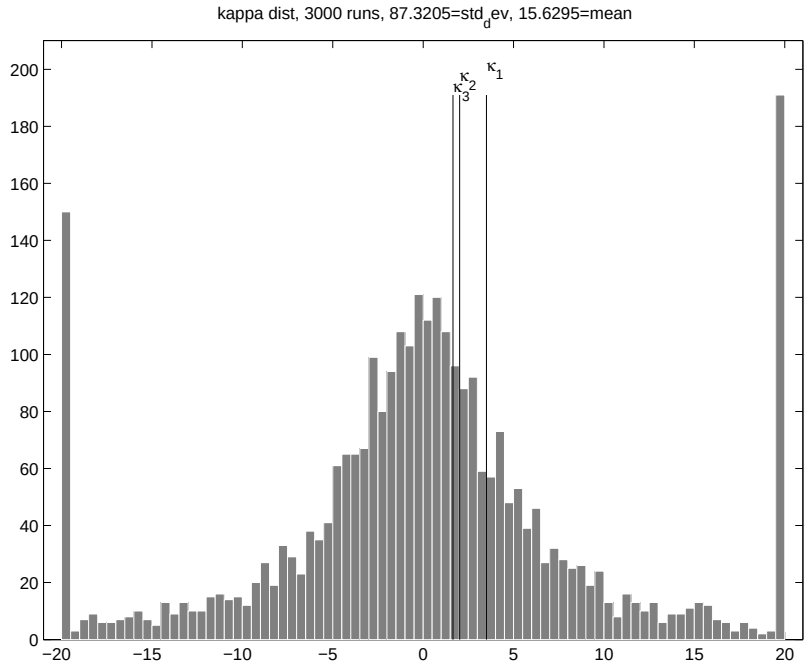

Figure 3.13: κ Distribution for 3000 Configurations of 20 Randomly Distributed Jets on a Prolate Comet Body.

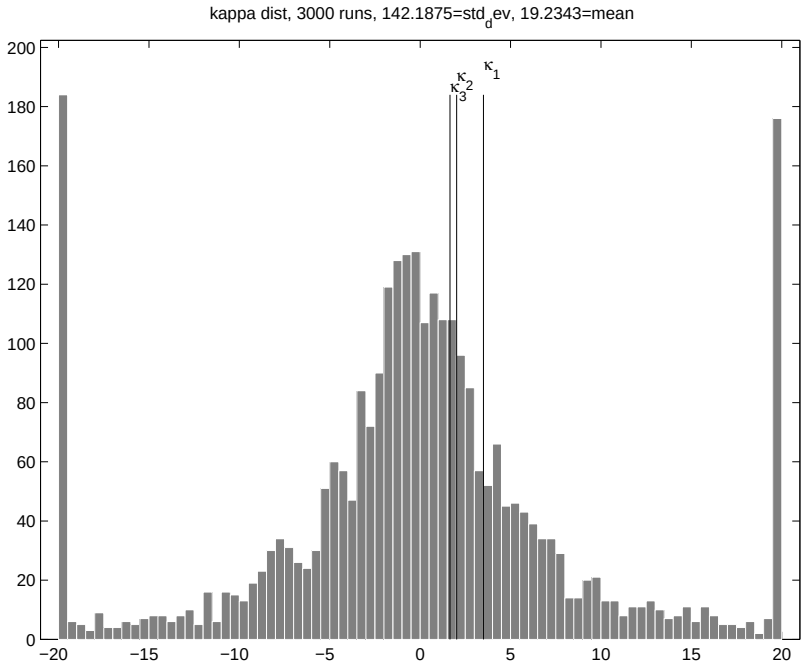

Figure 3.14: κ Distribution for 3000 Configurations of 50 Randomly Distributed Jets on a Prolate Comet Body.

For a given heliocentric orbit, 20 jets randomly distributed on the surface yields a κ value distribution similar to a Gaussian distribution seen in figure 3.13 where $\sim$ 50% spin up and $\sim$ 50% spin down. Table 3.4 gives a representative example of the end state distribution for an oblate body. Note that this distribution of end states is similar for the different jet numbers except for the single jet case where $\kappa_3 > |\kappa| > 0$ is not possible. This distribution holds for a prolate body as well. Since over half of the cases fall within $|\kappa| > \kappa_1$, it could be assumed that if the κ value lies within this interval for a comet then small changes in its jet geometry or heliocentric orbit would cause the new κ value to remain within this interval where the angular momentum vector drifts to align with the symmetric moment of inertia along the inertial perihelion vector. This predicts that oblate nuclei will have an asymptotic spin state that is fully relaxed, but a prolate body will have a fully excited asymptotic spin state. Note that energy dissipation in not included in this analysis and may

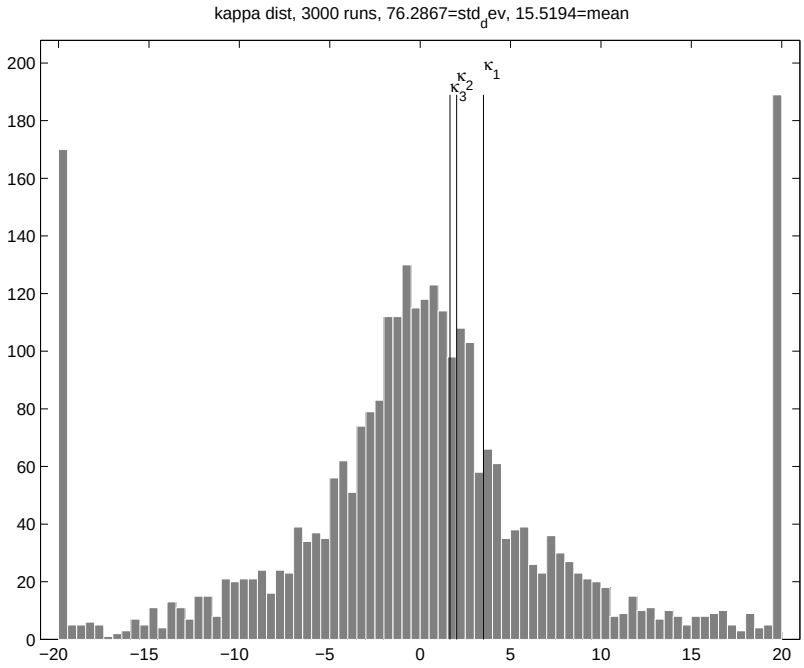

Figure 3.15: κ Distribution for 3000 Configurations of 100 Randomly Distributed Jets on a Prolate Comet Body.

Table 3.4: Distribution of End States

$jets$	$\lvert\kappa\rvert > \kappa_1$	$\kappa_1 > \lvert\kappa\rvert > \kappa_2$	$\kappa_2 > \lvert\kappa\rvert > 0$
1	38%	46%	17%
20	55%	16%	29%
50	54%	15%	31%
100	54%	16%	30%

change the end state of the system.

In summary, we see that this theory predicts a variety of outcomes for comet nuclei. We see that at least half migrate towards an increasing spin rate over time, which could eventually lead to the bursting phenomenon commonly seen among comets. Conversely, there is also a population that tends towards a decreasing angular momentum, which could comprise a class of more slowly rotating nuclei. It is expected that when the rotation period of such nuclei is decreased significantly that the averaging assumptions made would no longer apply. Based on the theory we also

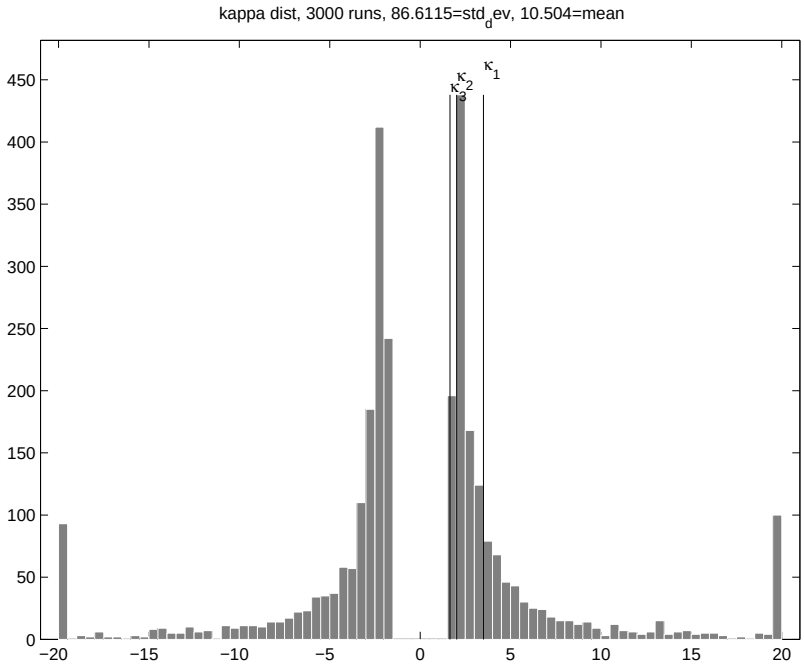

Figure 3.16: κ Distribution for 3000 Configurations of 1 Randomly Distributed Jet on a Prolate Comet Body.

see a variety of different rotation states that a nucleus could tend towards. When non-symmetric inertia moments are assumed there should be additional final states that can be found, as discussed and derived using the simpler insolation model in [29]. Note that these are asymptotic results for the end state that will be applied to specific studies later.

3.3.1 Variable Jet Geometry

Finally, by allowing the κ parameters to slowly shift stochastically over time it may be possible to develop a statistical model for the evolution of a comet nuclei's rotation state. In the following, we implement a simple version of this as a proof of concept. Up to this point, it has been assumed that the jet geometry of the comet remains fixed with time. This is a somewhat unrealistic assumption as we would expect that the surface of the comet could possibly change as a result of the jets' sublimation relocating jets or, as the rotation axis evolves, new portions of the comet's surface will be exposed or shadowed allowing for the activation or deactivation of jets respectively. Therefore, it is useful to study a variable jet geometry with respect to the averaged equations. We explore stochastic jet distributions which lead to a stochastic view of a comet's time evolution.

We consider a comet with a fixed finite number of jets at randomly distributed locations on the surface oriented in the outward normal to the surface. We assume that each jet can expire after some random number of perihelion passages and when a jet expires, a new randomly located jet is created keeping the number of jets on the surface constant. This relocation happens at aphelion where the jets are minimally outgassing. Except for location, orientation, and expiration time, the jets are assumed to be identical in size and outgassing speed. This setup allows for a randomly variable jet geometry (thus a variable κ) although it does not correlate with a jet being activated as a result of a portion of the surface becoming sunlit. Figures 3.17- 3.19 illustrate that the averaged equations can be adjusted for the variable κ with time to predict the evolution of the rotation pole over multiple orbits. The averaged equations begin to deviate from the full equations of motion after many orbital periods due to the periodic offset at each κ change not being

adjusted. This example illustrates the effect that the jet locations have on the end spin state of the comet nucleus as well as on its evolutionary path. This however is only part of the bigger picture. The jets are allowed to relocate to any random location but realistically it would be informative to have the jets relocate only to areas which receive sunlight or to allow the number of jets to decrease over time.

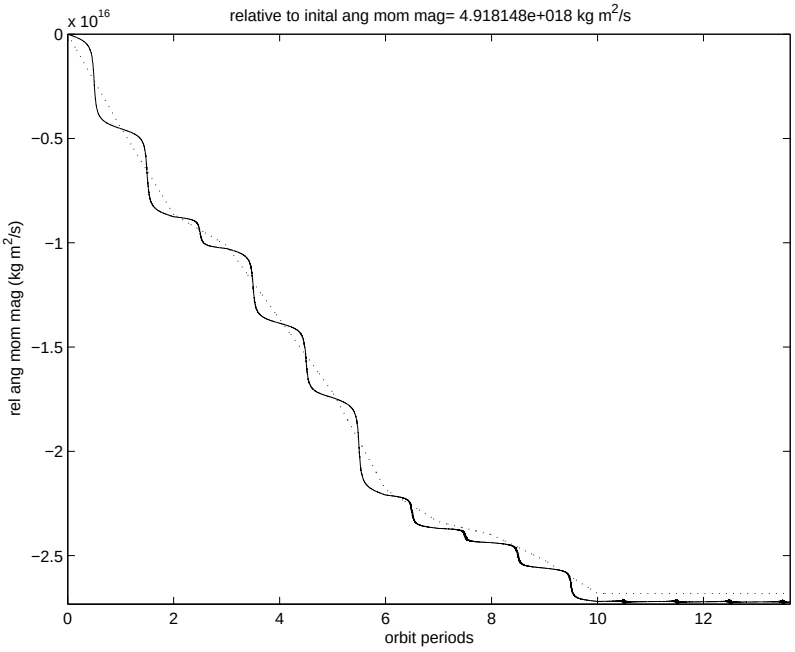

Figure 3.17: Relative Angular Momentum Magnitude for Variable κ with 20 Jets Randomly Expiring and Relocating at Intervals of $10 - 15$ Perihelion Passages. Solid = Equations of Motion, Dashed = Averaged Equations.

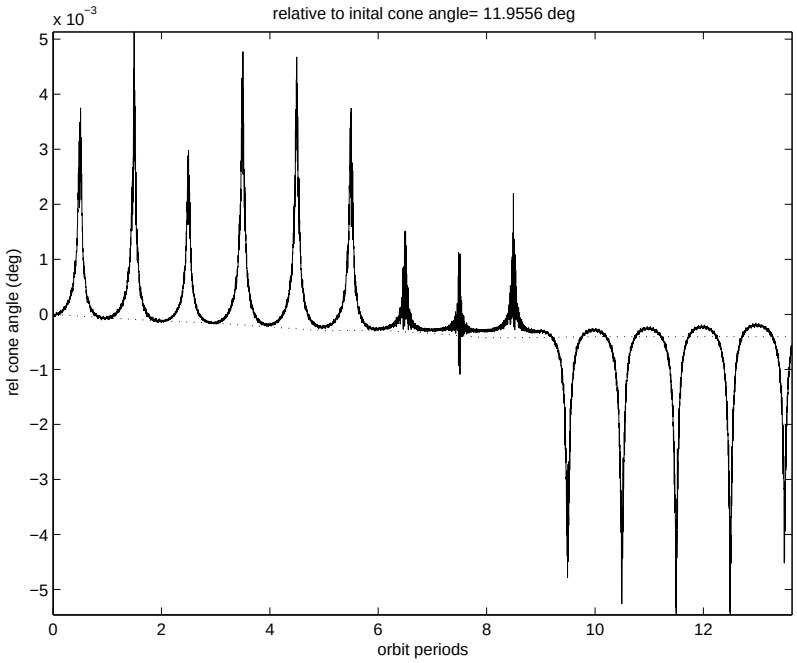

Figure 3.18: Relative cone for for Variable κ with 20 Jets Randomly Expiring and Relocating at Intervals of $10-15$ Perihelion Passages. Solid = Equations of Motion, Dashed = Averaged Equations.

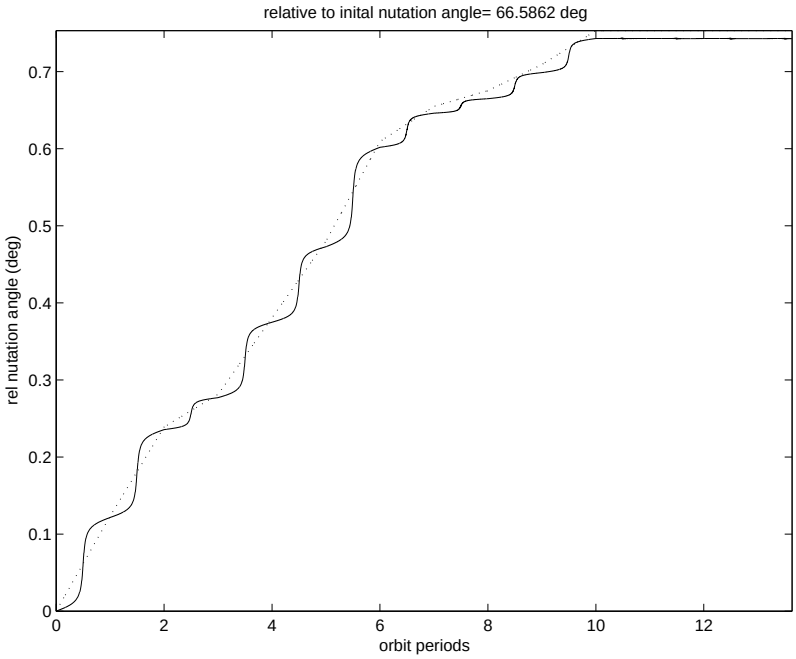

Figure 3.19: Relative nutation angle for for Variable κ with 20 Jets Randomly Expiring and Relocating at Intervals of $10 - 15$ Perihelion Passages. Solid = Equations of Motion, Dashed = Averaged Equations.

3.4 Summary

In this chapter, we derived improved averaged equations for rotationally symmetric bodies as a result of reactive torques produced by jets. The averaged equations were compared to the full equations of motion, integrated using a variational algorithm, and were shown to capture the drift in the rotational state of the comet. This can be used to predict the rotational state of the comet nucleus as it passes through perihelion. With a small correction in the initial conditions, the averaged equations accurately capture the long term drift in the comet's rotation state assuming fixed jet geometry over multiple perihelion passages. The theory allows the comet nucleus dynamics to be propagated over long time spans as a function of a few parameters. A variable jet geometry's effect on the evolution was explored and compared to the

averaged equations' prediction with similar results. By examining these averaged equations over long time spans, insight into comet spin up and spin down can be gained.

CHAPTER IV

Outgassing Jet Passage Dynamics

The outgassing jets on a comet provide a unique dynamical environment for an orbiting spacecraft. Strong jets have the ability to significantly modify a spacecraft's orbit about a comet and may create the possibility to escape the comet's weak gravitational field while weaker jets may only slightly change the spacecraft's trajectory. Therefore, the effects of passage through outgassing jets on an orbiting spacecraft need to be carefully explored and will be the focus of this chapter.

4.1 Orbit Mechanics in the Presence of an Outgassing Jet

4.1.1 Orbital Elements with Radial Impulse

In order to predict what will happen when a spacecraft passes through a jet outgassing field, consider small changes in orbital elements. First, note that for large distances from the comet, the radial component of the outgassing is dominant and therefore the outgassing due to a jet passage can be considered a radial impulse. We begin with the orbital parameter, p:

$$p = a(1 - e^2) \tag{4.1}$$

where a is the spacecraft's semimajor axis and e is it's eccentricity. First we note that p has been shown to be conserved [4] through a jet passage as it is related to

the angular momentum which does not change under a radial impulse; a proof is presented later. Taking a small change in p, Δp, yields:

$$\Delta p = \Delta a(1 - e^2) - 2ae\Delta e. \tag{4.2}$$

Next, if we consider the orbital energy, E, it can be rearranged to find a small change in the semimajor axis, a.

$$E = -\frac{\mu}{2a}, \tag{4.3}$$

$$\Delta E = \frac{\mu \Delta a}{2a^2}, \tag{4.4}$$

$$\Delta a = \frac{2a^2 \Delta E}{\mu}, \tag{4.5}$$

where μ is the gravitational parameter for the comet.

As seen in equation 4.5, a positive change in energy increases the semimajor axis and a negative change in energy results in a decrease in the semimajor axis. Substituting this result into equation 4.2 and setting $\Delta p = 0$, yields the result:

$$\Delta e = \frac{a\Delta E}{\mu e}(1 - e^2). \tag{4.6}$$

Note that a positive change in energy increases the eccentricity and that a negative change in energy results in a decrease in the eccentricity. In terms of a jet passage, rewriting the energy equation as a function of the spacecraft's velocity provides additional insight.

$$E = \frac{1}{2}v^2 - \frac{\mu}{|\vec{r}|}, \tag{4.7}$$

where v is the magnitude of the spacecraft's velocity. Variations in energy will arise due to impulsive changes in the spacecraft's velocity:

$$\Delta E = v \cdot \Delta v. \tag{4.8}$$

Substituting this result into equations 4.5 and 4.6, produces:

$$\Delta a = \frac{2a^2 v \cdot \Delta v}{\mu}, \tag{4.9}$$

$$\Delta e = \frac{av \cdot \Delta v}{\mu e}(1 - e^2). \tag{4.10}$$

From equations 4.9 and 4.10, it can be seen that an increase in velocity increases the semimajor axis and the eccentricity and that a decrease in velocity results in a decrease in the semimajor axis and the eccentricity of an orbiting spacecraft. Since the outgassing primarily acts in the radial direction when the spacecraft is at a large distance from the comet body, the radial component of the spacecraft's velocity is the only effected component. Therefore, if the spacecraft has a negative radial velocity component (figure 4.1) such as when it is travelling from apoapsis to periapsis, the outgassing jet will tend to circularize the orbit, or decrease the semimajor axis and eccentricity. Likewise, if the spacecraft has a positive radial velocity component such as when it is travelling from periapsis to apoapsis, the outgassing jet will tend to make the orbit more eccentric and increase the semimajor axis.

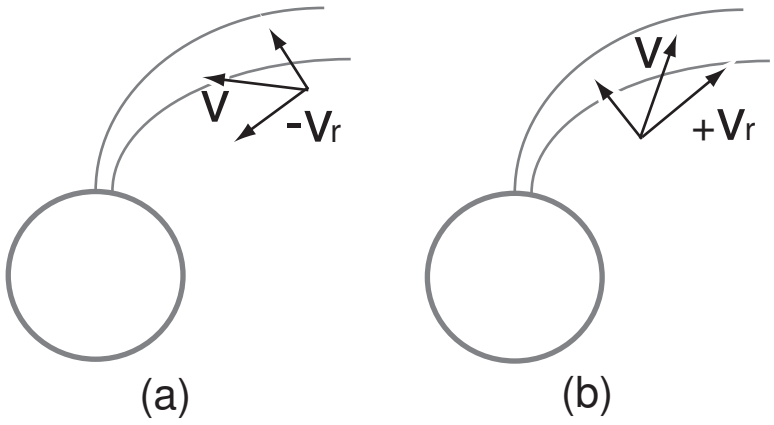

Figure 4.1: Spacecraft Velocity Components: (a) Negative Radial Component, (b) Positive Radial Component

The radius of periapsis, $q = a(1 - e)$, is also of interest when considering the

effects of an outgassing jet passage. For a small change in the radius of periapsis:

$$\Delta q = \Delta a(1-e) - a\Delta e. \tag{4.11}$$

This can be related to a change in velocity by substituting for the semimajor axis and eccentricity from equations 4.9 and 4.10.

$$\Delta q = \frac{-q^2 v \cdot \Delta v}{\mu e}. \tag{4.12}$$

There is an increase in radius of periapsis when the spacecraft has a negative radial velocity component during a jet passage. Likewise, a decrease in radius of periapsis occurs when the spacecraft has a positive radial velocity component during a jet passage. These orbital changes have the possible application of controlling a spacecraft's trajectory by targeting known jets.

4.1.2 Lagrange Planetary Equations

Changes in the full set of orbital elements for a spacecraft can be explored by considering the Lagrange planetary equations. Starting with these equations in the Gaussian form:

$$\begin{aligned}
\frac{da}{dt} &= \frac{2a^2 e}{h}\sin\nu\hat{F}_R + \frac{2a^2 h}{\mu r}\hat{F}_T, && (4.13)\\
\frac{de}{dt} &= \frac{h}{\mu}\left(\sin\nu\hat{F}_R + \frac{e+2\cos\nu+e\cos^2\nu}{1+e\cos/nu}\hat{F}_T\right), && (4.14)\\
\frac{di}{dt} &= \frac{r}{h}\cos\varpi\hat{F}_N, && (4.15)\\
\frac{d\Omega}{dt} &= \frac{r\sin\varpi}{h\sin i}\hat{F}_N, && (4.16)\\
\frac{d\omega_p}{dt} &= -\frac{h}{\mu e}\cos\nu\hat{F}_R - \frac{r}{h}\cot i\sin\varpi\hat{F}_N + \frac{(h^2+r\mu)\sin\nu}{\mu e h}\hat{F}_T, && (4.17)\\
\frac{d\bar{M}}{dt} &= n - \frac{1}{na}\left(\frac{2r}{a} - \frac{(1-e^2)}{e}\cos\nu\right)\hat{F}_R \\
&\quad -\frac{(1-e^2)}{nae}\left(1+\frac{r}{p}\right)\sin\nu\hat{F}_T, && (4.18)
\end{aligned}$$

where

$$h = na^2\sqrt{1-e^2}, \tag{4.19}$$

$$n = \sqrt{\frac{\mu}{a^3}}, \tag{4.20}$$

$$\varpi = \omega_p + \nu, \tag{4.21}$$

$$r = |\vec{r}|, \tag{4.22}$$

and $\hat{F}_R$, $\hat{F}_T$, and $\hat{F}_N$ are accelerations in the radial, transverse, and orbit normal directions, respectively, and ν is the true anomaly. For jet passages, we have assumed that the spacecraft is located far from the comet body such that the outgassing component in the radial direction is dominant, therefore the acceleration terms in equations 4.13 to 4.18 become:

$$\hat{F}_R = a_p = p_0 \frac{1}{B}\left(\frac{r_0}{|\vec{r}_j|}\right)^2, \tag{4.23}$$

$$\hat{F}_T = 0, \tag{4.24}$$

$$\hat{F}_N = 0, \tag{4.25}$$

where r_0 is the comet radius at the jet location, and $\vec{r}_j$ is the position of the spacecraft relative to the virtual center of the jet. Substituting in these force components into the Lagrange planetary equations for a spacecraft during an outgassing jet passage

become:

$$\frac{da}{dt} = \frac{2a^2e}{h}\sin\nu p_0\frac{1}{B}\left(\frac{r_0}{|\vec{r}_j|}\right)^2, \tag{4.26}$$

$$\frac{de}{dt} = \frac{h}{\mu}\sin\nu p_0\frac{1}{B}\left(\frac{r_0}{|\vec{r}_j|}\right)^2, \tag{4.27}$$

$$\frac{di}{dt} = 0, \tag{4.28}$$

$$\frac{d\Omega}{dt} = 0, \tag{4.29}$$

$$\frac{d\omega_p}{dt} = -\frac{h}{\mu e}\cos\nu p_0\frac{1}{B}\left(\frac{r_0}{|\vec{r}_j|}\right)^2, \tag{4.30}$$

$$\frac{d\bar{M}}{dt} = n - \frac{1}{na}\left(\frac{2r}{a} - \frac{(1-e^2)}{e}\cos\nu\right)p_0\frac{1}{B}\left(\frac{r_0}{|\vec{r}_j|}\right)^2. \tag{4.31}$$

Note that the radial acceleration will always be positive since the outgassing pressure acts only in the outward radial direction. It can be seen that the outgassing pressure affects only four of the orbital elements: the semimajor axis, a, the eccentricity, e, the argument of perigee, ω_p, and the mean anomaly, $\bar{M}$. As seen in equations 4.26 and 4.27, the semimajor axis and the eccentricity will increase while the spacecraft's radial velocity is positive and will decrease while the spacecraft's radial velocity is negative. The $\sin\nu$ term in equation will be positive while the spacecraft is located along the periapsis to apoapsis portion of its orbit where it has a positive radial component of its velocity. Likewise, the $\sin\nu$ term will be negative while the spacecraft is located along the apoapsis to periapsis portion of its orbit where it has a negative radial component of its velocity. This agrees with the previous analysis of the semimajor axis and the eccentricity. As noted previously, the parameter p is conserved. This can be proven using the results of a radial acceleration in the Lagrange planetary equations.

$$\frac{dp}{dt} = \frac{da}{dt}(1-e^2) - 2ae\frac{de}{dt}, \tag{4.32}$$

$$\frac{dp}{dt} = \frac{2a^2e}{h}\sin\nu p_0\frac{1}{B}\left(\frac{r_0}{|\vec{r}_j|}\right)^2(1-e^2) - 2ae\frac{h}{\mu}\sin\nu p_0\frac{1}{B}\left(\frac{r_0}{|\vec{r}_j|}\right)^2 = 0. \tag{4.33}$$

Estimates for changes in the orbit parameters due to a jet passage can be obtained. If we assume that the comet spin period is faster than the spacecraft orbital period, the time it takes for the jet to sweep over a spacecraft located at the jet longitude, λ_0, is approximately:

$$\Delta t = \frac{2\delta}{\omega \cos \lambda_0}. \tag{4.34}$$

This leads to impulsive changes in orbital elements of

$$\Delta a = \frac{da}{dt}\Delta t = \frac{2a^2 e}{h} \sin \nu p_0 \frac{1}{B} \left(\frac{r_0}{|\vec{r}_j|} \right)^2 \frac{2\delta}{\omega \cos \lambda_0}, \tag{4.35}$$

$$\Delta e = \frac{de}{dt}\Delta t = \frac{h}{\mu} \sin \nu p_0 \frac{1}{B} \left(\frac{r_0}{|\vec{r}_j|} \right)^2 \frac{2\delta}{\omega \cos \lambda_0}, \tag{4.36}$$

$$\Delta \omega_p = \frac{d\omega_p}{dt}\Delta t = -\frac{h}{\mu e} \cos \nu p_0 \frac{1}{B} \left(\frac{r_0}{|\vec{r}_j|} \right)^2 \frac{2\delta}{\omega \cos \lambda_0}. \tag{4.37}$$

$$\tag{4.38}$$

Note that if the spacecraft travels opposite to the comet's rotation, the impulse will be less than if the spacecraft travels in the same sense as the comet's rotation.

If the spacecraft is close to the comet where the outgassing acceleration cannot always be assumed to be in the radial direction, the Lagrange planetary equations need to be carefully examined to determine the dominating acceleration term. Consider the Lagrange equations for semimajor axis and eccentricity:

$$\frac{da}{dt} = \frac{2a^2 e}{h} \sin \nu \hat{F}_R + \frac{2a^2 h}{\mu r} \hat{F}_T, \tag{4.39}$$

$$\frac{de}{dt} = \frac{h}{\mu} \left(\sin \nu \hat{F}_R + \frac{e + 2\cos \nu + e \cos^2 \nu}{1 + e \cos /nu} \hat{F}_T \right). \tag{4.40}$$

$$\tag{4.41}$$

If $\hat{F}_T \neq 0$, then an impulse in the transverse direction can affect a and e. Depending on the magnitudes of $\hat{F}_R$ and $\hat{F}_T$, it is possible for the semimajor axis to decrease while the eccentricity increases and vice versa. This however will need to be determined on a case by case basis.

Table 4.1: Simulation Parameters

Variable	Description	Value	Unit
a	comet principle length	2.75	km
b	comet principle length	2.00	km
c	comet principle length	1.65	km
P	comet period	12	hr
V_{og}	outgassing radial velocity	0.5	km/s
ω	comet rotation rate	$\frac{2\pi}{T}$	rad/s
δ	jet shape half angle	1.5	degree
Q_*	mass ejection rate for entire comet$^+$	3.4×10^6	kg/hr
B	spacecraft mass to area ratio	30^*	kg/m^2

* assumed to be same as comet Wirtanen.
$^+$ mass ejection rate for each jet determined by jet surface area.

4.2 Simulation of Passages through Outgassing Jets

A Matlab script was written incorporating the outgassing jet model and the comet body model. The spacecraft was assumed to follow the trajectory described by solving the standard two-body problem while the spacecraft is not within an outgassing region. The pressure acceleration, $\vec{a}_p$, is applied to the spacecraft when it is determined that the angle between the outgassing pressure vector (at the same radius as the spacecraft) and the spacecraft position vector, θ_{rel}, is within a defined angle error tolerance, $\Delta\theta_{err}$, of the half angle describing the active region's size. The angle θ_{rel} is determined by:

$$\theta_{rel} = \arccos \frac{\vec{r}_{og} \cdot \vec{r}}{\|\vec{r}_{og}\|\|\vec{r}\|}, \tag{4.42}$$

where $\vec{r}$ is the position vector of the spacecraft given in the same coordinate frame as $\vec{r}_{og}$.

The simulation presented is of an idealized comet 81P/Wild2 (values in tables 4.1 and 2.1) where the mass ejection rate is from Neishtadt, et al.[11], with 20 discrete outgassing jets located on the surface in the comet. The jets are assumed to be

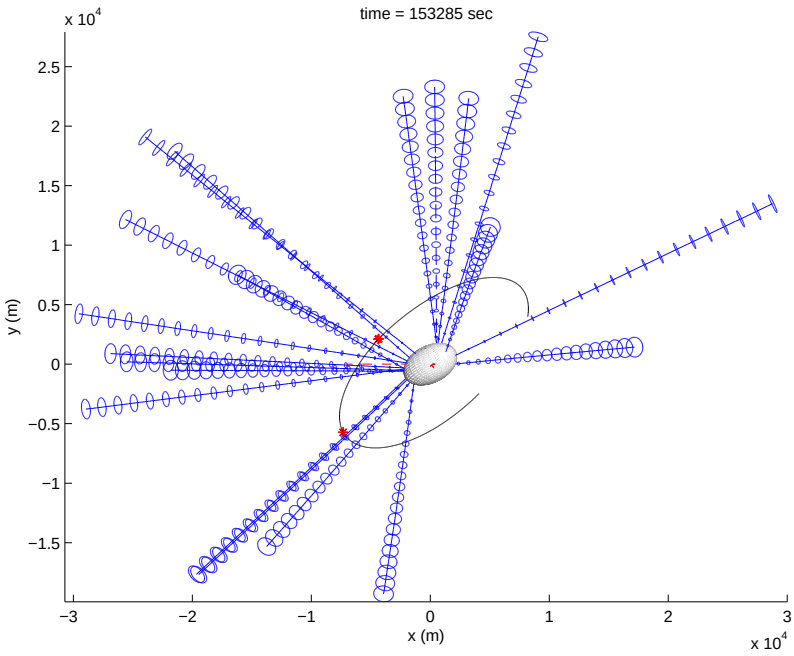

Figure 4.2: Spacecraft Trajectory in Inertial Frame for Interaction with Outgassing Jets with a Half Angle of 1.5° and V_{og} of 0.5 km/s on the Idealized 81P/Wild2

identical with a jet half angle of 1.5 degrees and an outgassing velocity of 0.5 km/s although the script is written to allow for each jet to have a unique geometry. Figures 4.2 to 4.5 show the results of this simulation where the thicker sections of the spacecraft's trajectory illustrate the portion of the trajectory where the spacecraft is passing though an outgassing jet field. Figure 4.5 shows the changes in the orbital elements, semimajor axis and eccentricity, when the spacecraft encounters an outgassing jet. The two jet passages can clearly be identified by the sharp changes in the orbital elements. Since the spacecraft is located close to the comet, we note that the radial impulse assumption is not valid for the first jet passage where the jet outgassing orientation is clearly not radial but is a better approximation for the second jet passage where the jet orientation is much closer to the radial direction. This simulation assumes that the location, size, and orientation of each jet is known.

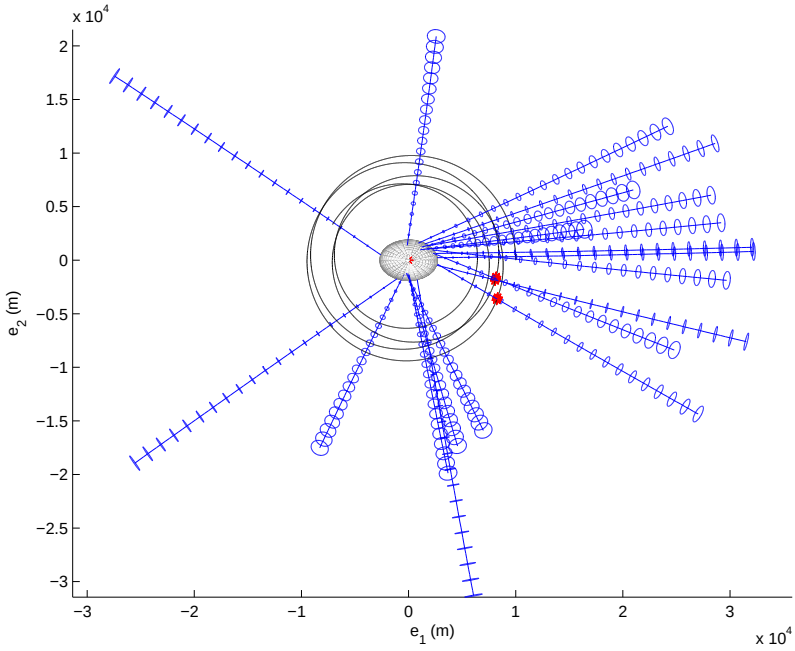

Figure 4.3: Spacecraft Trajectory in Body Fixed Frame for Interaction with Outgassing Jets with a Half Angle of 1.5° and V_{og} of 0.5 km/s on the Idealized 81P/Wild2

This will rarely be the case for an orbiting spacecraft and, therefore, it is informative to use the trajectory data to determine the jet's parameter. A method for estimating some of the jet characteristics will be the focus of the next chapter.

4.3 Summary

In this chapter, a model of a triaxial ellipsoidal comet was simulated using 20 discrete jets based on the comet Wild 2 model to verify the analytical results found by assuming small changes in the orbital elements of the spacecraft relative to the comet. The first case considered was when a spacecraft passes though a nearly radially outgassing jet, such as when it is far from the comet. It was shown that if the spacecraft has a negative radial velocity component, the outgassing jet will decrease the semimajor axis and eccentricity and vice versa for a radial impulse when the spacecraft is located significantly far from the comet. If, on the other

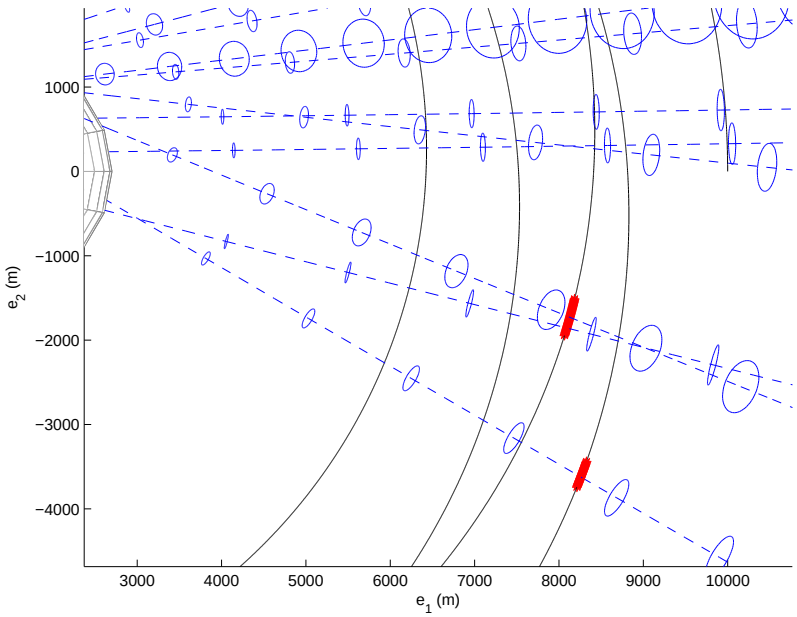

Figure 4.4: Spacecraft Trajectory in Body Fixed Frame for Interaction with Outgassing Jets with a Half Angle of 1.5° and V_{og} of 0.5 km/s on the Idealized 81P/Wild2 (Detail)

hand, the spacecraft is in close proximity to the comet nucleus, it has been shown that the transverse component of the outgassing can affect the semimajor axis and eccentricity of the spacecraft oppositely depending therefore the orientations of the jets should be known prior to attempting to land on the comet surface to properly predict the trajectory of the spacecraft.

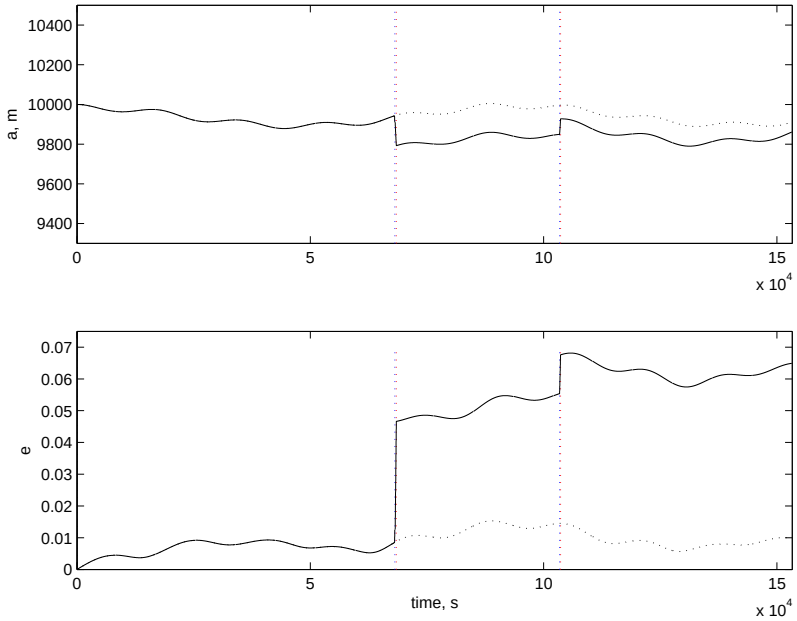

Figure 4.5: Semimajor Axis and Eccentricity for Spacecraft with Interaction with Outgassing Jets with a Half Angle of 1.5° and V_{og} of 0.5 km/s on the Idealized 81P/Wild2 with the Dotted lines Showing the Orbital Elements for Encountering No Jets. Note that There are Natural Variations Due to the Non-Point Mass Gravity Field.

CHAPTER V

Outgassing Jet Parameter Estimation

One important use of the outgassing jet model is to aid in spacecraft navigation. This model can be used to estimate the defining jet parameters from spacecraft passages through a discrete jet outgassing field. Based on Doppler tracking and a standard navigation solution for the spacecraft's trajectory, the jet's basic describing parameters: the jet's location and the half angle, δ, and the pressure of the outgassing, $|\vec{p}|$, can be estimated. By providing a specific model with parameters that can be estimated from tracking data, we both enable future trajectories to be predicted more accurately, and provide measurements of scientific interest. In this chapter, we explore how to estimate some of the outgassing jet parameters based on our model from trajectory data.

5.1 Outgassing Acceleration on Spacecraft

Identifying an outgassing jet passage is crucial to being able to estimate its characteristics. Therefore, a spacecraft is assumed to begin passage through an outgassing field when the Doppler tracking detects an acceleration larger than $1.667 \times 10^{-5} m/s^2$ (the accuracy to which Doppler data can unambiguously detect change in velocity). Since the acceleration is directly measured, if we can estimate the spacecraft's mass

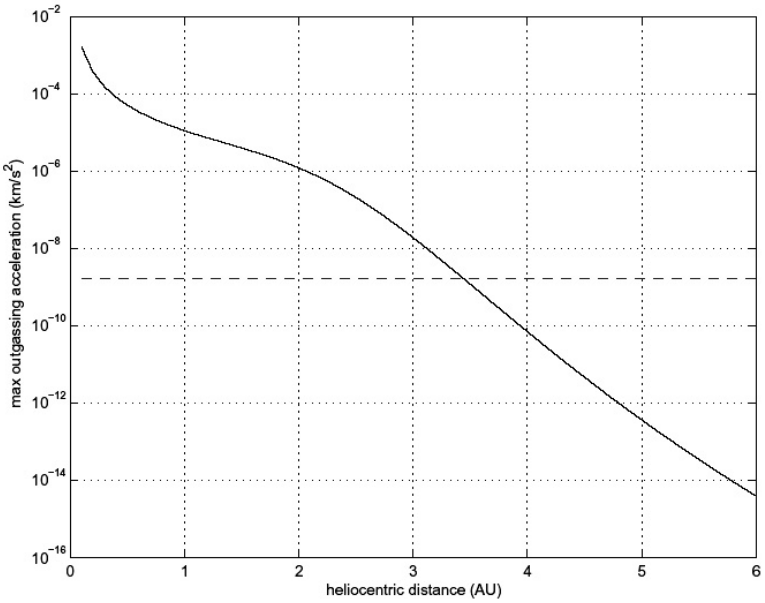

Figure 5.1: Outgassing Acceleration as a Function of Comet Orbital Radius for $V_{og} = 0.5$ km/s. Solid = Maximum Outgassing Acceleration. Dotted = Doppler Tracking Threshold.

to area ratio of the side facing the comet, B, and the mass flux rate of the jet, Q_j, (using a mass spectrometer), we can also gain a direct estimate of the outgassing speed using the relationship:

$$|\vec{a_p}| = Q_j V_{og} \frac{1}{B} \left(\frac{r_0}{|\vec{r_j}|} \right)^2 . \tag{5.1}$$

Some knowledge of the jet geometry would be needed for this estimate but could be obtained from images of the comet prior to the jet fly-through. In addition to estimating the outgassing velocity, this detection can also be used to identify boundary crossings of the jet outgassing field. These crossings can be used to create unit vectors in the direction of a crossing in the body fixed frame, $\hat{u}_i$, to aid in estimation of other jet parameters (to be discussed in detail in the next section). The creation of the crossing unit vectors assumes that a navigation solution for the spacecraft is available.

As mentioned in the jet model description, the outgassing strength is a function

of the distance of the comet from the Sun. Therefore it is necessary to determine the maximum heliocentric distance allowed for Doppler tracking to be able to detect this boundary crossings. If we assume an outgassing velocity of 0.5 km/s, the magnitude of the outgassing acceleration can be detected by Doppler tracking when the comet's orbital radius is less then 3 AU as seen in figure 5.1. The spikes in the spacecraft's acceleration components (seen in figure 5.2 from simulation data) illustrate jet passages. Since the magnitude of the acceleration spikes are on the order of $10^{-5}m/s^2$, the jet passages should be able to be identified by the Doppler tracking producing estimates of not only the outgassing speed but also mapping boundary points of outgassing jet fields. This calculated maximum heliocentric distance will change assuming different outgassing speeds.

5.2 Jet Location and Half Angle, δ

The model definition describes the parameters for a single jet, but realistically there would exist multiple jets on a comet similar to the Wild2 model[6] and the one used in the model simulations. When developing an estimation method for the jet parameters, this was carefully taken into account. With multiple jets emanating from the surface of the comet, it becomes necessary to appropriately identify each crossing with a probable jet location. Naturally these jet boundary crossings occur in pairs, one crossing classified as entering and one as exiting the outgassing field. The degenerate case of "skimming" the boundary producing a single point for both entering and exiting the field can be applied in the methods considered. The pairs can be mapped to the surface of the comet in the body fixed frame as unit vectors that lie on the surface boundary of the jet if the rotation of the comet and the outgassing velocity, V_{og}, is assumed to be known. The time since ejection, s, can be

found using the assumed outgassing velocity and the radial distance from the surface of the comet. This time gives the angular rotation of the comet from the rotation rate, ω_{com}. Rotating the comet back in time and translating the crossing point to the surface of the comet gives the mapping method to the body fixed frame.

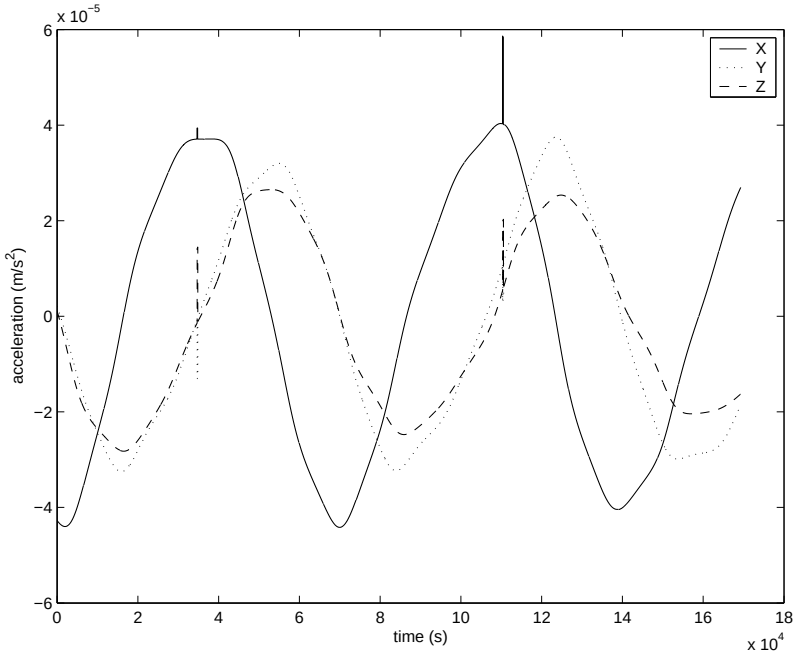

Figure 5.2: Spacecraft Acceleration Components in an Inertial Frame

After the pairs have been mapped to the comet surface, they are identified with a possible jet location by checking the proximity of the unit vector which defines the pair's bisector with possible jets' estimated centerlines which have already been identified. If the bisector unit vector falls within the jet's estimated size (defined as the estimated half angle, δ, with some allowable tolerance) then the pair is grouped with other identified pairs for the possible jet location. If the bisector unit vector does not match with an existing possible jet location, the pair define a new possible jet location to be tested for subsequent crossings.

Once a crossing pair has been identified with a possible jet location, the number of pairs identified with that jet location determines the estimation process as illustrated

in figure 5.3. If only a single pair has been identified, then the jet centerline location is assumed to be the unit vector which bisects the pair of unit crossing vectors, and the half angle of the jet is estimated as half of the angle between the pair of crossing unit vectors as in jet 1 of figure 5.3. If multiple pairs are associated with a possible jet location, three possible methods to estimate the jet location and half angle are explored. All of these estimation methods allow for the spacecraft to fly-through at different altitudes and allows for curved paths through the outgassing field. Two of the methods are based on the geometry of the circular cross section and the third utilizes the directly determined unit vectors. There is a detailed discussion of each method in the following sections.

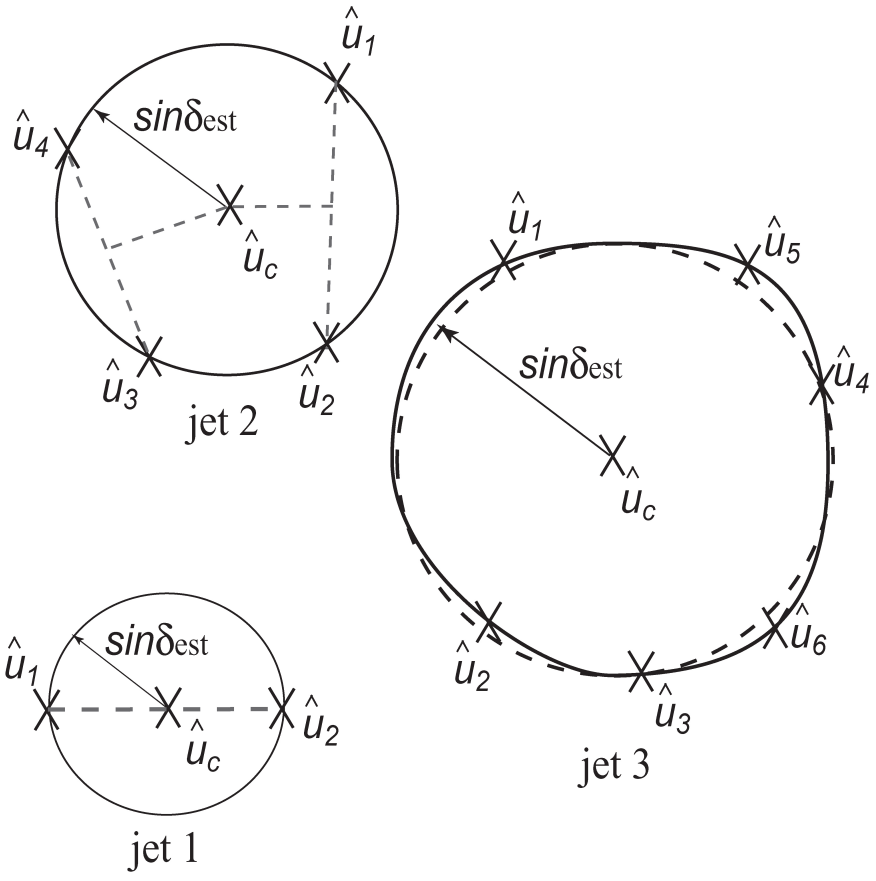

Figure 5.3: Illustration of Jet Identification Methods.

5.2.1 Geometrical Approach 1

The first geometrical approach needs only two pair of crossings to estimate the centerline position and jet half angle. The pairs are connected to form two chords. The crossing of the bisecting perpendiculars to these chords will give an estimate of the center of the jet. Using Pythagoras' theorem on one of the chords yields the estimate of the half angle as seen in figure 5.4. If the spacecraft is known to be in the plane of the outgassing jet then the chord constructed is the diameter of the jet cross section and reduces to the method used for a single pair crossing. This method has a maximum of two boundary crossing pairs and would not yield better estimations with subsequent passages.

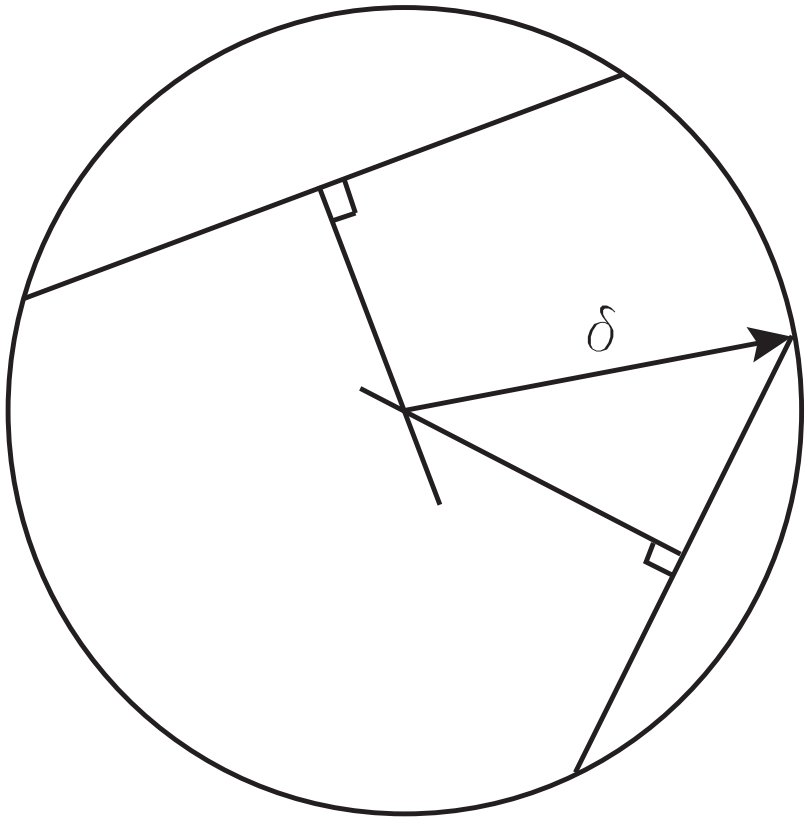

Figure 5.4: Perpendicular Bisectors Method of Estimating Jet Half Angle

5.2.2 Geometrical Approach 2

The second geometrical approach requires only one and a half crossing pairs of the jet outgassing field (three unit crossing vectors). Using the three unit vectors in the body fixed frame as vertices of a triangle, the geometrical formula for finding the radius of an circumscribed circle about a triangle can be used to estimate the jet half angle, δ, as seen in figure 5.5.

$$r_0 \sin\delta = \frac{1}{2}\frac{a_t b_t c_t}{\sqrt{s(s-a_t)(s-b_t)(s-c_t)}}, \tag{5.2}$$

$$s = \frac{1}{2}(a_t + b_t + c_t), \tag{5.3}$$

where a_t, b_t, and c_t are the chord lengths created by connecting the three crossings. Once the half angle is known, the center of the jet can be inferred by finding the common intersection point of circle of radius δ drawn about each crossing point. This approach could be used if one of the boundary crossings is ill-defined such as in the "skimming" case. Again, this method has a finite maximum of crossing points and would not yield better estimations with subsequent passages.

5.2.3 Least Squares Approach

The third approach is the most general of the estimation methods presented. It allows for non-circular cross-sections of the outgassing jet to be ideally estimated such as jet 3 in figure 5.3 and does not need finite boundary crossing points to be used in the estimate. Using the mapped boundary crossing unit vectors in the body fixed frame (illustrated in figure 5.6), another unit vector pointing in the direction of the estimated center of the cross-section is defined. The nominal cone angle is then found as:

$$\hat{u}_i.\hat{u}_c = \cos(\delta), \tag{5.4}$$

where $\hat{u}_i$ is the unit vector in the direction of crossing number i and $\hat{u}_c$ is a unit vector in the direction of the cross-section's estimated center. A pair of boundary crossings will produce a plane of possible solutions to $\hat{u_c}$. The location of the center of the outgassing jet can be estimated uniquely by a third crossing giving an estimated solution to $\hat{u}_c$ and thus the half angle, δ. Therefore, a minimum of three boundary crossings is needed.

These estimates for the jet center location and the half angle can be refined when subsequent boundary crossings occur by using a least squares approach to incorporate newly detected crossing unit vectors. First define a cost function as:

$$J_c = \frac{1}{2}\sum_{i=1}^{N}(\hat{u}_i \cdot \hat{u}_c - \cos\delta)^2. \tag{5.5}$$

Taking the partial derivative of this with respect to the center unit vector and setting it equal to zero yields an estimate for $\vec{u}_c$.

$$\frac{\partial J_c}{\partial \hat{u}_c} = \sum_{i=1}^{N}(\hat{u}_i \cdot \hat{u}_c - \cos\delta)\hat{u}_i = 0, \tag{5.6}$$

$$\vec{u}_c = \cos\delta(\sum_{i=1}^{N}\hat{u}_i\hat{u}_i)^{-1}\sum\hat{u}_i. \tag{5.7}$$

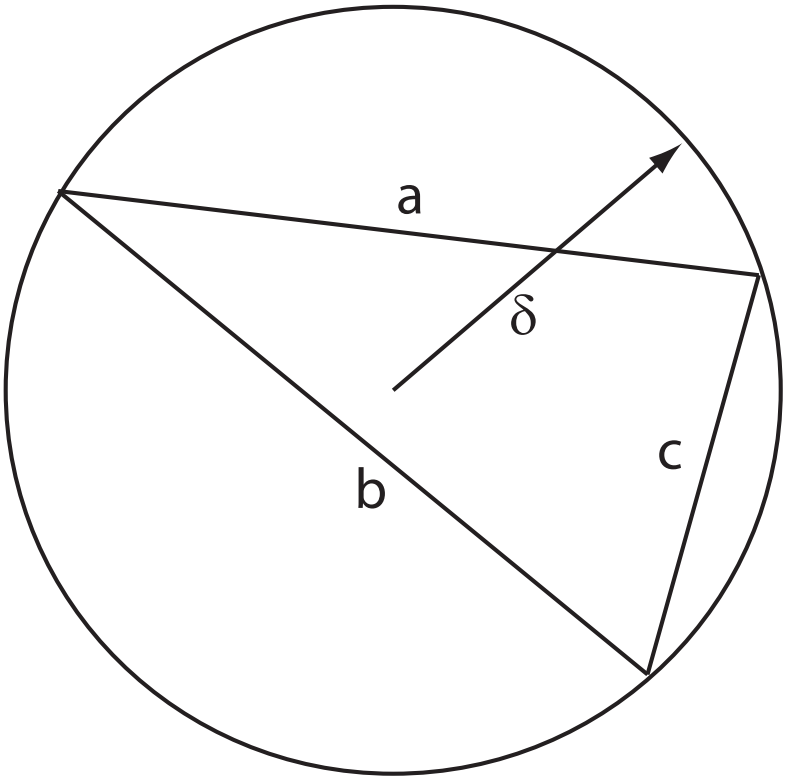

Figure 5.5: Circumscribed Triangle Method of Estimating Jet Half Angle

Note that this solution will point in the direction of the proper solution, but may not be a unit vector. Normalizing the estimate for $\vec{u}_c$ yields a function only of the boundary crossing unit vectors.

$$\hat{u}_c = \frac{(\sum_{i=1}^{N} \hat{u}_i \hat{u}_i)^{-1} \sum \hat{u}_i}{|(\sum_{i=1}^{N} \hat{u}_i \hat{u}_i)^{-1} \sum \hat{u}_i|}. \tag{5.8}$$

For $N < 3$, the term $\sum_{i=1}^{N} \hat{u}_i \hat{u}_i$ will not be invertible in general, but for $N \geq 3$ and a properly measured set of $\hat{u}_i$, it will produce a unique solution. Taking the partial derivative of the cost function with respect to the jet half angle, δ, yields an estimate for the half angle which is dependent on the estimate for the center unit vector found previously in equation 5.8.

$$\frac{\partial J_c}{\partial \delta} = \sum_{i=1}^{N} (\hat{u}_i \cdot \hat{u}_c - \cos\delta) \sin\delta, \tag{5.9}$$

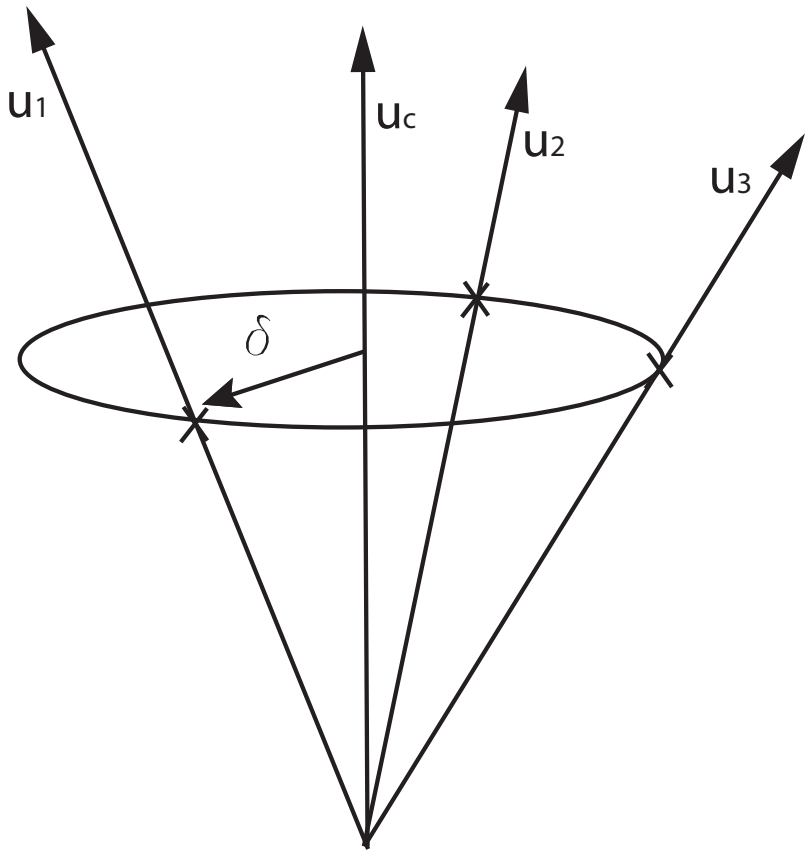

Figure 5.6: Body Fixed Unit Vectors Method of Estimating Jet Half Angles

$$\cos\delta = \frac{1}{N}(\sum_{i=1}^{N}\hat{u}_i)\cdot\hat{u}_c, \tag{5.10}$$

$$\delta = \arccos(\frac{1}{N}\hat{u}_c\cdot\sum_{i=1}^{N}\hat{u}_i). \tag{5.11}$$

These new estimates for the jet centerline unit vector and half angle can be used to identify subsequent jet crossing pairs with the jet in the case of multiple jet encounters. This iterative process allows for the mapped pairs to be identified properly to the correct jet and the estimated jet parameters to be updated each time the spacecraft passes though the jet's outgassing field.

Once the location and half angle of the jets have been estimated, the mapped boundary crossing vectors can be intersected with the surface of the comet to define the boundary of an active surface patch associated with the jet. Correlating this

surface patch with images of the comet's surface can yield insight into the orientation or source of the jet from surface features such cavities or sharp inclines.

5.2.4 Estimation Errors

The errors in these estimations can be caused by uncertainty in the spacecraft's position, uncertainty in the comet's rotation, or from lack of detailed knowledge of the outgassing jet's structure. Uncertainty in the spacecraft's position and in the comet's rotation can produce errors in the mapped unit vectors yielding errors in the boundary crossings. The spacecraft's position and comet rotation will have the largest uncertainties when the spacecraft arrives at the comet and will be better known as the spacecraft orbits the comet and will need to be updated within the estimation algorithm.

Lack of knowledge of the jet's structure is a more complicated error as it can lead to errors in the identification of jet locations. Consider that the jet's outgassing pressure profile is not a solid cone of pressure but has another profile such as a hollow cone similar to a tube. A spacecraft passing through this type of profile will produce more "boundary crossings" than actually exist. This would yield the appearance of crossing two jets instead of one. Then leading the estimation algorithm to identify two pairs of boundary crossings and in turn producing two possible jet center locations although realistically there is only one. The methods described above would need to be modified if a hollow cone pressure profile or another pressure profile is suspected.

5.3 Estimation Simulation

Utilizing the jet model simulation data, the boundary crossing positions and times are collected and passed on to estimate the jet parameters. The estimation

simulation uses the unit vector least squares approach to estimate the jet center unit vector and the jet half angle assuming that the outgassing velocity and comet rotation are already known. Note that the locations of the jets are not assumed to be initially known and are estimated as well. If only a single pair has been identified with a possible jet location, then the half angle of the jet is estimated as half of the angle between the pair of boundary crossing unit vectors.

Using simulation data for a single trajectory encountering multiple jets with a half angle of 1.5 degrees and outgassing velocity of 0.5 km/s, seen in figure 5.7, the jet half angle is estimated by changing the maximum allowable angle error in the simulation of the spacecraft's trajectory. The maximum allowable angle error is defined as the largest angle with respect to the jet boundary such that the spacecraft is considered to have crossed the boundary. This replicates the spacecraft's measurement error.

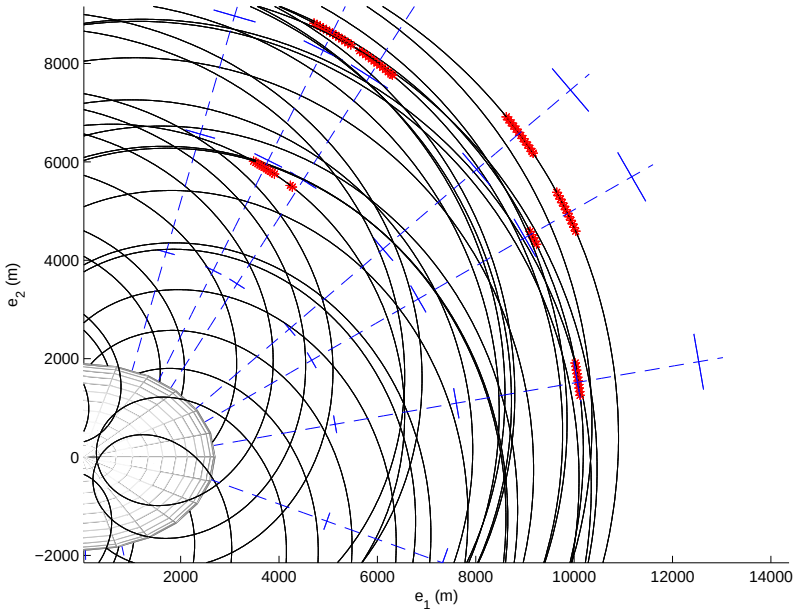

Figure 5.7: Detailed View of Simulation of Jets with Half Angle of 1.5 degrees and Outgassing Velocity of 0.5 km/s Used for Estimation Simulation.

For the half angle estimate, a small angle error in the measurement results, in general, in a smaller half angle estimate error as seen in table 5.1. The jet half-angles

Table 5.1: Outgassing Half Angle Estimation in Degrees Using ≥ 4 Boundary Crossing Points

Jet No.	Crossings pts.	Maximum Angle Error 1 degree	0.5 degree	0.1 degree
1	2	2.3337	2.3337	2.5458
2	4	2.3120	2.4327	2.8134
3	4	0.6354*	2.2614	2.4815
4	2	1.9073	1.9073	1.9073
5	2	0.4227	0.4227	0.4227
6	2	1.6908	1.6908	1.6908
7	2	1.9236	1.9236	2.1373
8	4	2.9108	2.9108	1.9160
9	2	2.4646	2.4646	2.2406
10	2	0.4206	0.6309	0.8412
11	2	2.5279	2.5279	2.5279
12	2	1.6857	1.4750	1.6857

* estimated with two crossing points.

which remained constant with varying angle error tolerance are caused by the initial boundary crossing detections already residing within the smallest angle error tolerance for the simulated cases. The time step used in the simulation can affect the estimates since they determine the detected boundary crossing position. The algorithm reduces the time step of the integration until the boundary crossing detected resides within the angle error tolerance. The boundary crossing position detected may also be affected by whether or not the simulation has already encountered a jet and has varied the time step previously. The errors in the estimation can also be caused by uncertainty in the spacecrafts position, uncertainty in the comets rotation, or from lack of detailed knowledge of the outgassing jets structure as discussed previously.

5.4 Estimation Applications

The described estimation methods have many applications as navigation tools for a spacecraft. The estimates can be used to identify jets and map their locations on the surface of the comet as well as determine their size as described. These parameters can give the spacecraft better trajectory fits and predictions for orbiting spacecrafts' passages through jets. The location of the jet also allows for targeted scientific measurements, turning on measurement instruments only when the spacecraft is in the vicinity of an outgassing jet field and off when not needed. In conjunction with mass spectrometer measurements, we can determine the gas velocity with simple relationships. This also holds if we are given a gas velocity from which we can determine the gas mass flux.

Applications of measuring and determining the outgassing field and jet structure can also be obtained once the field boundary has been crossed. The spacecraft can measure the variation of the outgassing within a jet's field. It may not be a solid cone structure as assumed in the model, but may actually have an inactive or less active interior or another activity profile across the jet. Multiple passes can uncover complex jet boundaries that may be related to the outgassing conditions or features the comet surface.

5.5 Summary

In this chapter, estimation methods were presented to not only estimate the jet locations, but also the outgassing velocity and the half angle. The outgassing velocity can be determined by taking a measurement of the mass flux and the change in the spacecraft's acceleration using Doppler tracking depending on the outgassing strength and thus the heliocentric distance. The half angle can be estimated by

using boundary crossing points mapped to the surface of the comet. The method for estimating the half angle of the jet includes an algorithm for identifying jet locations when multiple jet outgassing fields have been crossed and for ideally estimating non-circular cross sections. These estimates help to provide a better trajectory fit for the spacecraft as well as to better predict future trajectories. By knowing probable jet locations, the spacecraft can target these areas for scientific measurements or avoid them to maintain particular orbital parameters.

CHAPTER VI

Solar Radiation Pressure and Third Body Effects

In Chapter IV, the effect of outgassing jets on an orbiting spacecraft was considered for the dynamical setup of the 2-body problem. We will now revisit this topic and consider the more complex dynamical setup of the 3-body problem with the gravitational attraction of the Sun and under the perturbation of solar radiation pressure. These effects will be important for a spacecraft to maintain a stable orbit in the vicinity of a comet. The focus of this chapter will be to identify and analyze stable Sun synchronous orbits in a rotating frame which can be used to orbit any small body in the solar system. Previously, Dankowicz[7] found an orbit offset from the comet's center of mass and explored the stability in a non-rotating system. Scheeres and Marzari[8] investigated the stability of such motions accounting for the orbit of the comet, while Scheeres[9] investigated the definition and stability of Sun-synchronous orbits started from the terminator plane. This analysis combines the offset orbits of Dankowicz[7] with the averaging analysis and rotation present in the analysis by Scheeres[9]. The stability of identified orbits will be tested for outgassing jet accelerations in the case of comets, and the effects of a non-spherical comet body will be considered. Once these orbits have been shown to be stable, different control schemes to restrict their allowable motion will be explored.

6.1 Equations of Motion

Consider the general case of a spacecraft in the vicinity of a comet and significantly far from any other celestial body. The spacecraft is assumed to have negligible mass relative to the comet (modelled as a point mass for now) and is subject to solar radiation pressure acting in the anti-sunward direction, $\hat{x}$. In an inertial frame, the equations of motion for the spacecraft are:

$$\ddot{\vec{r}}_I = \frac{\partial U}{\partial \vec{r}_I} + g\hat{x}, \tag{6.1}$$

where $\vec{r}_I$ is the position vector in an inertial frame, U is the comet's gravitational potential, and g is the solar radiation pressure magnitude computed as:

$$g = \frac{\beta}{d_c^2}, \tag{6.2}$$

where $\beta = (1+\eta)G_1/B$, $G_1 = 1x10^8 kg - km^3/(s^2 - m^2)$, B is the spacecraft mass to area ratio in kg/m^2, η is the reflectance of the spacecraft, and d_c is the heliocentric distance of the comet in km[9]. The Hill equations of motion are appropriate to use in this case given the dynamical setup. They are as follows in the comet orbit frame assuming a constant rotation about the Sun, ω.

$$\ddot{x} = 2\omega\dot{y} + 3\omega^2 x - \frac{\mu x}{r^3} + g, \tag{6.3}$$

$$\ddot{y} = -2\omega\dot{x} - \frac{\mu y}{r^3}, \tag{6.4}$$

$$\ddot{z} = -\omega^2 z - \frac{\mu z}{r^3}, \tag{6.5}$$

where x is along the Sun-comet line, z is out of the orbital plane, and $r = \sqrt{x^2 + y^2 + z^2}$. The Hill equations of motion in cartesian coordinates have a Jacobi integral of:

$$J = \frac{1}{2}(\dot{x}^2 + \dot{y}^2 + \dot{z}^2) - \frac{\mu}{r} - \frac{1}{2}\omega^2(3x^2 - z^2) - gx. \tag{6.6}$$

Note that for a constant rotation rate, ω, this integral is conserved. Although, cometary orbits do not generally have a constant angular rate, over the short times spans considered in this paper, a constant rate is a good approximation. A cylindrical frame will gain us more insight, therefore we apply the following transformation:

$$x = x, \tag{6.7}$$

$$y = \rho\cos\theta, \tag{6.8}$$

$$z = \rho\sin\theta, \tag{6.9}$$

$$\dot{x} = \dot{x}, \tag{6.10}$$

$$\dot{y} = \dot{\rho}\cos\theta - \rho\dot{\theta}\sin\theta, \tag{6.11}$$

$$\dot{z} = \dot{\rho}\sin\theta + \rho\dot{\theta}\cos\theta. \tag{6.12}$$

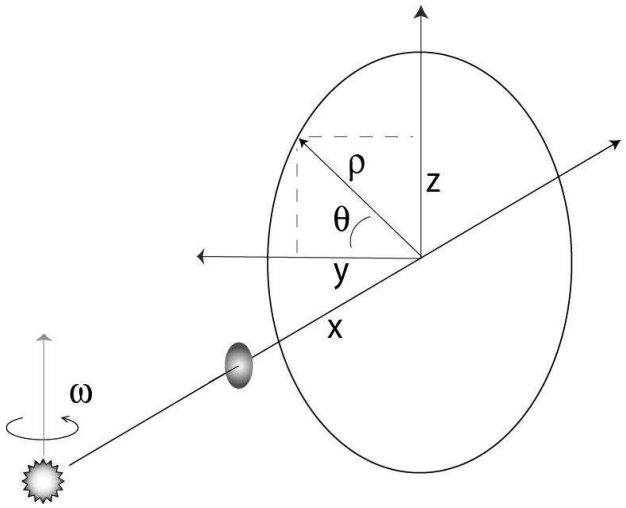

Figure 6.1: Relative Hill Coordinate Frames: Cartesian and Cylindrical.

Converting to the cylindrical coordinates, the equations of motion become:

$$\ddot{x} = 2\omega(\dot{\rho}\cos\theta - \rho\dot{\theta}\sin\theta) + 3\omega^2 x + g - \frac{x\mu}{r^3}, \tag{6.13}$$

$$\ddot{\rho} = -2\dot{x}\omega\cos\theta + \rho\dot{\theta}^2 - \rho\omega^2\sin^2\theta - \frac{\rho\mu}{r^3}, \tag{6.14}$$

$$\rho\ddot{\theta} = 2\dot{x}\omega\sin\theta - 2\dot{\rho}\dot{\theta} - \rho\omega^2\sin\theta\cos\theta, \tag{6.15}$$

where $r = \sqrt{x^2 + \rho^2}$. Note that a symmetry in the evolution of the x and ρ states exists for $+\dot{\theta}$ and $-\dot{\theta}$ when $\theta_0 = 0, \pi$. This is expected due to the term $\dot{\theta}\sin\theta = -\dot{\theta}\sin(-\theta)$ in the $\ddot{x}$ equation and $\dot{\theta}^2 = (-\dot{\theta})^2$ in the $\ddot{\rho}$ equation. For completeness, the Hill equations of motion in cylindrical coordinates have a Jacobi integral of:

$$J = \frac{1}{2}(\dot{x}^2 + \dot{\rho}^2 + \rho^2\dot{\theta}^2) - \frac{\mu}{r} - \frac{1}{2}\omega^2(3x^2 - \rho^2\sin(\theta)^2) - gx. \tag{6.16}$$

6.1.1 Non-Rotating Equilibrium Solution

The system studied by Dankowicz[7] is a non-rotating two-body problem with the addition of solar radiation pressure to the secondary body. The equations of motion used are (in cylindrical coordinates):

$$\ddot{x} = -\frac{\mu x}{r^3} + g, \tag{6.17}$$

$$\ddot{\rho} = \rho\dot{\theta}^2 - \frac{\mu\rho}{r^3}, \tag{6.18}$$

$$\rho\ddot{\theta} = \frac{-2\dot{\rho}\dot{\theta}}{\rho}. \tag{6.19}$$

Note that these are the same equations of motion described above if ω is set to 0. Directly integrating equation 6.19 leads to $\rho^2\dot{\theta} = h$ which is a constant angular momentum about the Sun-comet line. Dankowicz[7] found relative equilibrium solutions to these equations as a class of circular with the following conditions

$$0 = \frac{\mu}{r^3} - \frac{g}{x}, \tag{6.20}$$

$$0 = \frac{h^2}{\rho^4} - \frac{g}{x}. \tag{6.21}$$

This non-rotating system's equilibrium solutions will be the basis for the exploration of averaging the Hill equations of motion. These solutions produce a family of Sun-synchronous circular orbits offset from the comet body and perpendicular to the Sun-comet line. The orbits which are closest to the body are stable and as the x

offset gets large the orbits become unstable with equilibrium solutions not existing for all values of x. At a given equilibrium x_0 and ρ_0, the angle varies as $\theta = \theta_0 + ht/\rho_0^2$. Note that it is the addition of the solar radiation pressure that produces the offset orbit solutions.

6.1.2 Averaging Procedure and Results

If we assume that the rotation rate of the comet about the Sun, ω, is small, then we can derive a set of equations incorporating the rotational terms and eliminating the time-varying θ term. If we assume the nominal motion is along the circular orbit found for the non-rotating system, the equations of motion for the rotating system can be rewritten as

$$\dot{\mathbf{x}} = f(\mathbf{x}) + \omega^2 g(\mathbf{x}, t), \tag{6.22}$$

where $\mathbf{x}$ are the states of the system, $f(\mathbf{x})$ are the non-rotating terms of the equations of motion and $\omega^2 g(\mathbf{x}, t)$ are the rotational terms. Note that only the $g(\mathbf{x}, t)$ terms are a function of t through the θ coordinate. We introduce an averaging operator to extract the effect of the $g(\mathbf{x}, t)$ function over one spacecraft orbit.

Lets consider a generic function, $\chi(\theta)$, which is a function of the cylindrical coordinate θ. If this function is averaged over a full rotation through the θ variable then the averaging procedure is of the form:

$$\overline{\chi} = \frac{1}{2\pi} \int_0^{2\pi} \chi(\theta) d\theta. \tag{6.23}$$

If equations 6.13 through 6.15 are averaged over θ in this way, a system similar to the two body non-rotating system from Dankowicz[7], equations 6.17 through 6.19,

is recovered with the additional terms of $3\omega^2\overline{x}$ and $-\frac{1}{2}\overline{\rho}\omega^2$.

$$\ddot{\overline{x}} = g - \frac{\overline{x}\mu}{r^3} + 3\omega^2\overline{x}, \tag{6.24}$$

$$\ddot{\overline{\rho}} = \overline{\rho}\dot{\overline{\theta}}^2 - \frac{1}{2}\overline{\rho}\omega^2 - \frac{\overline{\rho}\mu}{r^3}, \tag{6.25}$$

$$\overline{\rho}\ddot{\overline{\theta}} = -2\dot{\overline{\rho}}\dot{\overline{\theta}}, \tag{6.26}$$

where $\overline{r} = \sqrt{\overline{x}^2 + \overline{\rho}^2}$. Note that equation 6.26 can be directly integrated as:

$$\overline{\rho}^2\dot{\overline{\theta}} = h, \tag{6.27}$$

where h is a constant and in this case is the averaged angular momentum magnitude. Therefore the averaged equations of motion reduce to functions of $\overline{x}$ and $\overline{\rho}$ with constant h:

$$\ddot{\overline{x}} = g - \frac{\overline{x}\mu}{\overline{r}^3} + 3\omega^2\overline{x}, \tag{6.28}$$

$$\ddot{\overline{\rho}} = \overline{\rho}\left(\frac{h^2}{\overline{\rho}^4} - \frac{1}{2}\omega^2 - \frac{\mu}{\overline{r}^3}\right), \tag{6.29}$$

$$\tag{6.30}$$

with an averaged Jacobi integral of:

$$\bar{J} = \frac{1}{2}(\dot{\overline{x}}^2 + \dot{\overline{\rho}}^2) - \frac{\mu}{\overline{r}} - \frac{1}{2}\omega^2(3\overline{x}^2 - \frac{1}{2}\overline{\rho}^2) - g\overline{x} + \frac{h^2}{2\overline{\rho}^2}, \tag{6.31}$$

where $\dot{\overline{\theta}} = h/\overline{\rho}^2$. Note this is the same Jacobi integral that can be obtained by examining the averaged equations alone where $V = \frac{\mu}{\overline{r}} + \frac{1}{2}\omega^2(3\overline{x}^2 - \frac{1}{2}\overline{\rho}^2) + g\overline{x} - \frac{h^2}{2\overline{\rho}^2}$. Dankowicz[7] discovered that the angular momentum projected along the Sun-comet line was constant for the non-rotating system. The angular momentum projected along the solar radiation direction, $\hat{x}$, for this rotating frame system is:

$$h_d = \hat{x} \cdot (\vec{r} \times \dot{\vec{r}}), \tag{6.32}$$

where its projected time derivative has the form:

$$\dot{h}_d = \hat{x} \cdot (\vec{r} \times \ddot{\vec{r}}). \tag{6.33}$$

If $\vec{r} = (x, y, z)$ and $\dot{\vec{r}} = (\dot{x}, \dot{y}, \dot{z})$, then this time derivative simply reduces to:

$$\dot{h_d} = \hat{x} \cdot (2\omega\dot{x}z - \omega^2 yz, gz + 2\omega\dot{y}z + 4\omega^2 xz, -gy - 2\omega(x\dot{x} + y\dot{y}) - 3\omega^2 xy), \quad (6.34)$$

$$\dot{h_d} = 2\omega\dot{x}z - \omega^2 yz. \quad (6.35)$$

Changing variables to cylindrical coordinates results in an angular momentum derivative of:

$$\dot{h_d} = 2\omega\dot{x}\rho\sin\theta - \frac{1}{2}\omega^2\rho^2\sin(2\theta). \quad (6.36)$$

Applying the averaging procedure, equation 6.23, to the projected angular momentum derivative shows that the average value of $\dot{h_d}$ over 2π in θ is 0 due to the $\sin\theta$ and $\sin(2\theta)$ terms if we assume constant values for ρ and ω and a zero or periodic value for $\dot{x}$. This means that the projected angular momentum along $\hat{x}_s$ is conserved on average when orbiting along one of the offset terminator orbits. This conservation of the projected angular momentum implies that on average the dynamics in this rotating system have similarities to the non-rotating system found in Dankowicz[7].

6.2 Equilibrium Solutions

To find the equilibrium solutions to this set of equations, we set $\ddot{\overline{x}}$ and $\ddot{\overline{\rho}}$ to zero and find that the following conditions must hold:

$$3\omega^2 = \frac{\mu}{\overline{r}^3} - \frac{g}{\overline{x}}, \quad (6.37)$$

$$\frac{7}{2}\omega^2 = \frac{h^2}{\overline{\rho}^4} - \frac{g}{\overline{x}}. \quad (6.38)$$

Note that these conditions are similar to the ones found by Dankowicz[7] with a perturbation from the rotation, ω. For a given value of initial averaged x-offset, $\overline{x}_0$, then the variables $\overline{\rho}_0$, $\dot{\overline{\theta}}_0$, and h_0 can be found as functions of $\overline{x}_0$ yielding a family of

circular orbits perpendicular to the Sun line which are Sun synchronous:

$$\overline{\rho}_0 = \sqrt{\left(\frac{\overline{x}_0\mu}{3\omega^2\overline{x}_0 + g}\right)^{2/3} - \overline{x}_0^2}, \tag{6.39}$$

$$\dot{\overline{\theta}}_0 = \frac{7\omega^2}{2} + \frac{g}{\overline{x}_0}, \tag{6.40}$$

$$h_0 = \overline{\rho}_0^2\dot{\overline{\theta}}_0. \tag{6.41}$$

Note that these solutions are dependent on the values of μ, ω, and g resulting in different family profiles for each system. Again, these solutions do not exist for all x_0. An example profile of the family of circular orbits with a 0.25 km diameter body with 200 kg/m^3 bulk density at approximately 3 AU yielding values of $\mu = 1.1972e-10$ km^3/s^2, $\omega = 3.7749e-8$ rad/s, and $g = 1.4749e-11$ km/s^2 can be seen in figure 6.2 while figures 6.3- 6.6 illustrate trajectory examples in the vicinity of these circular orbits. Note that the larger the x offset, the more the trajectory deviates from the averaged solution. The stability as a function of the x_0 offsets is studied later. These orbits can be considered to be generalizations of the terminator orbits described in Scheeres[9]. It is important to note that these orbits are sun-synchronous and will ideally always present the same orientation to the Sun.

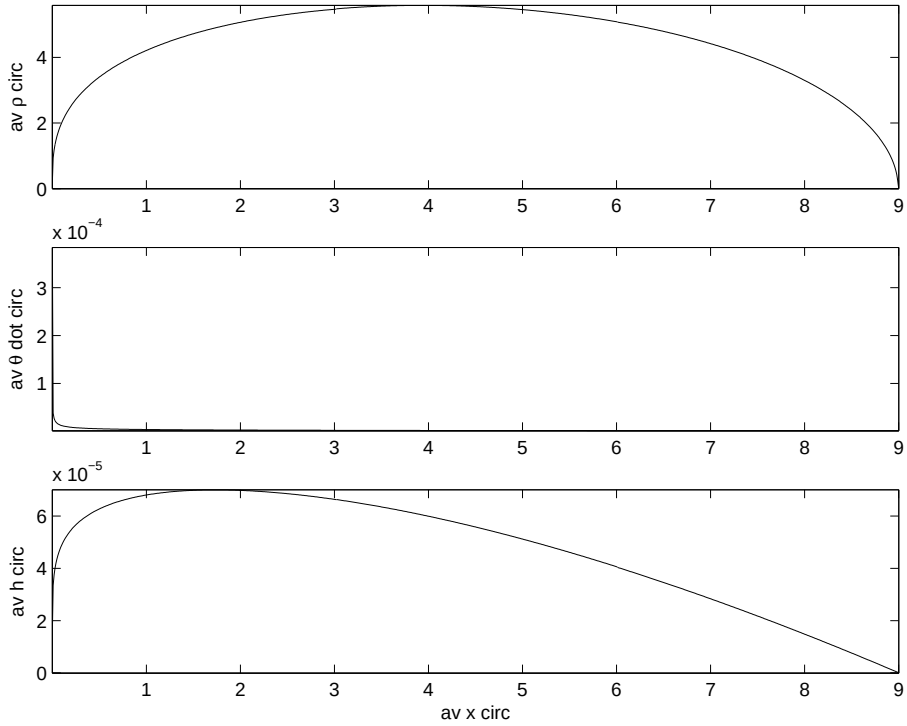

Figure 6.2: Example of Circular Orbit Equilibrium Solutions of the Averaged equations as a Function of the x Offset.

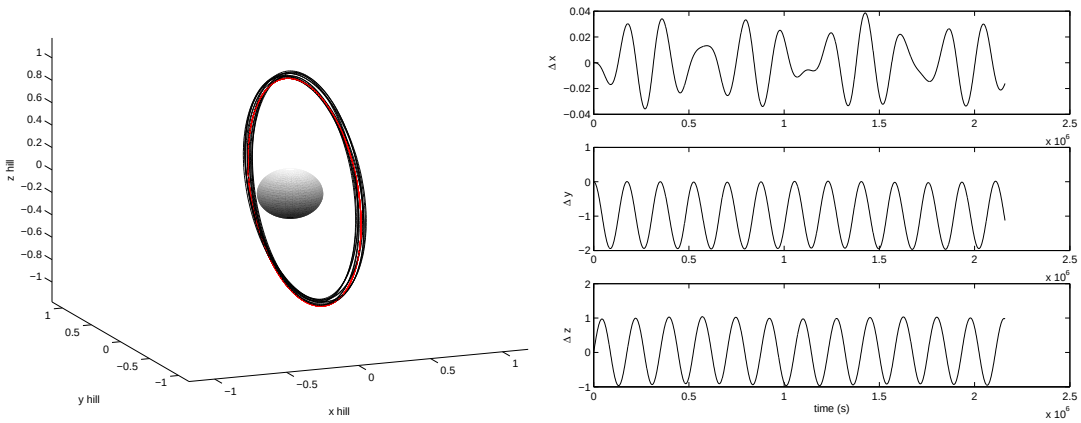

Figure 6.3: Initial Offset (x_0=0.1 km) Orbit About a Comet with a Regular Gravity Field in the Rotating Frame. Black = Full Hill Equations of Motion Trajectory. Red = Averaged Hill Equations of Motion Trajectory. Shown with Full Equations' Position Deviation (Δx,Δy,Δz) from the Averaged Solution.

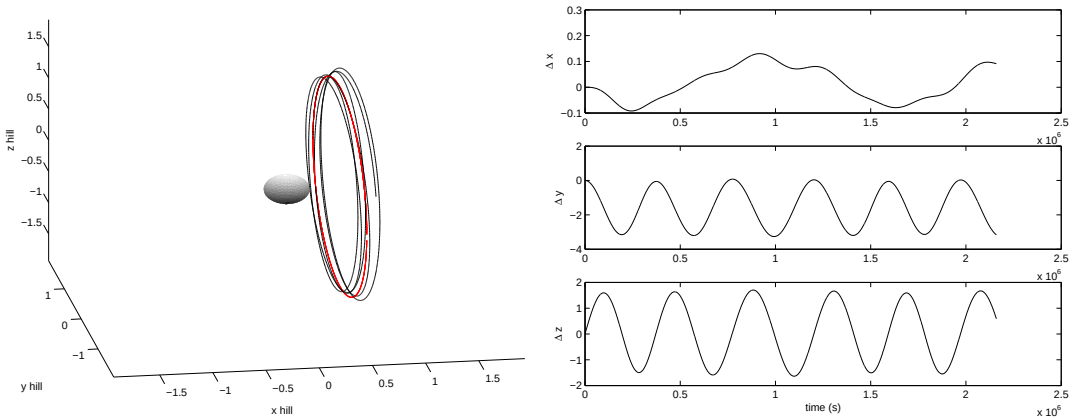

Figure 6.4: Initial Offset (x_0=0.5 km) Orbit About a Comet with a Regular Gravity Field in the Rotating Frame. Black = Full Hill Equations of Motion Trajectory. Red = Averaged Hill Equations of Motion Trajectory. Shown with Full Equations' Position Deviation (Δx,Δy,Δz) from the Averaged Solution.

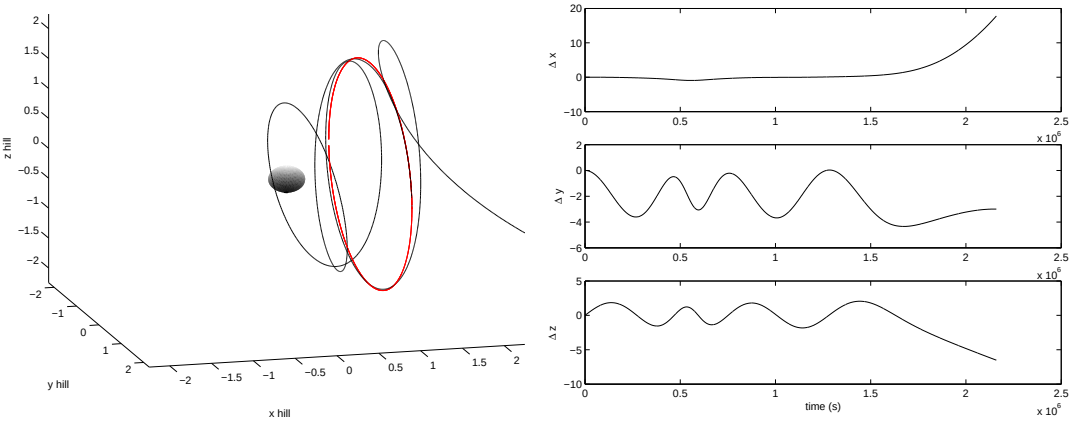

Figure 6.5: Initial Offset (x_0=1 km) Orbit About a Comet with a Regular Gravity Field in the Rotating Frame. Black = Full Hill Equations of Motion Trajectory. Red = Averaged Hill Equations of Motion Trajectory. Shown with Full Equations' Position Deviation (Δx,Δy,Δz) from the Averaged Solution.

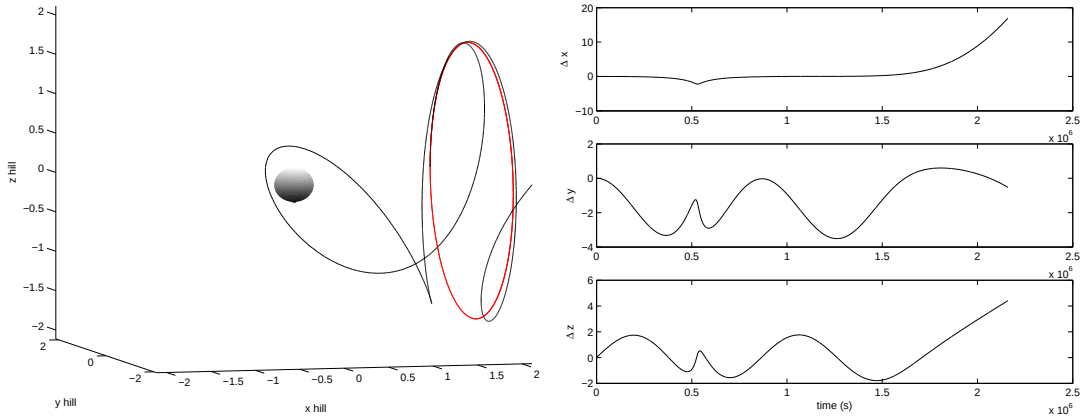

Figure 6.6: Initial Offset (x_0=2 km) Orbit About a Comet with a Regular Gravity Field in the Rotating Frame. Black = Full Hill Equations of Motion Trajectory. Red = Averaged Hill Equations of Motion Trajectory. Shown with Full Equations' Position Deviation (Δx,Δy,Δz) from the Averaged Solution.

6.3 Zero Velocity Curves

It is instructive to construct the zero velocity curves that exist for this problem to gain insight into the dynamics of the system. These curves will also help determine if there are any trajectories that may be trapped. To find the zero velocity curves, we set the averaged Jacobi integral, Equation 6.31, to some arbitrary constant, C, and the velocities to zero.

$$C = -\frac{\mu}{\overline{r}} - \frac{1}{2}\omega^2(3\overline{x}^2 - \frac{1}{2}\overline{\rho}^2) - g\overline{x} + \frac{h^2}{2\overline{\rho}^2}. \tag{6.42}$$

Note that $C = -V$ as expected and therefore for a given value of C, the spacecraft's motion can occur where

$$C + V \geq 0. \tag{6.43}$$

To find the zero velocity curves, we consider the simplified equation:

$$C_m + \frac{\mu}{\overline{r}} + \frac{1}{4}\omega^2\overline{\rho}^2 - \frac{h^2}{2\overline{\rho}^2} = 0, \tag{6.44}$$

where

$$C_m = C + \frac{3}{2}\omega^2\overline{x}^2 + g\overline{x}. \tag{6.45}$$

C_m is considered a constant for a given value of $\overline{x}$. Rearranging equation 6.44, the zero velocity curves can be found by solving for the roots of the following polynomial:

$$\begin{aligned} 0 \;=\; & \left(\frac{1}{16}\omega^4\right)\overline{\Gamma}^5 + \left(-\frac{1}{2}C_m\omega^2 + \frac{1}{16}\omega^4\overline{x}^2\right)\overline{\Gamma}^4 \\ & + \left(C_m^2 + \frac{1}{4}h^2\omega^2 - \frac{1}{2}C_m\omega^2\overline{x}^2\right)\overline{\Gamma}^3 + \left(-\mu^2 - C_m h^2 + C_m^2\overline{x}^2 + \frac{1}{4}h^2\omega^2\overline{x}^2\right)\overline{\Gamma}^2 \\ & + \left(\frac{1}{4}h^4 - C_m h^2\overline{x}^2\right)\overline{\Gamma} + \left(\frac{1}{4}h^4\overline{x}^2\right). \end{aligned} \tag{6.46}$$

Note that only values of $\overline{\rho} \geq 0$ are appropriate in cylindrical coordinates so the variable $\overline{\Gamma} = \overline{\rho}^2$ is used in the polynomial. For a given, $\overline{x}$, h, C, and g, the zero

velocity curves can therefore be computed. Figure 6.7 (detailed view in figure 6.8) shows the zero velocity curves for various circular orbit equilibrium solutions within a family. Note that as the x offset gets small, the area of allowable motion on the Sun side of the equilibrium solution reduces until the equilibrium solution becomes a disconnected stable point from the zero velocity curve. Visually this limit appears to be a stable/unstable boundary for the circular orbit equilibrium solutions although this will be analytically verified in the next section. Figure 6.9 shows the curves for differing values of C while holding h, ω, and g constant. For an h value associated with a stable equilibrium solution, increasing the energy opens up the allowable area for motion around the equilibrium point and a large enough value leads to the two areas merging together at a conjugate unstable equilibrium point which has the same h value.

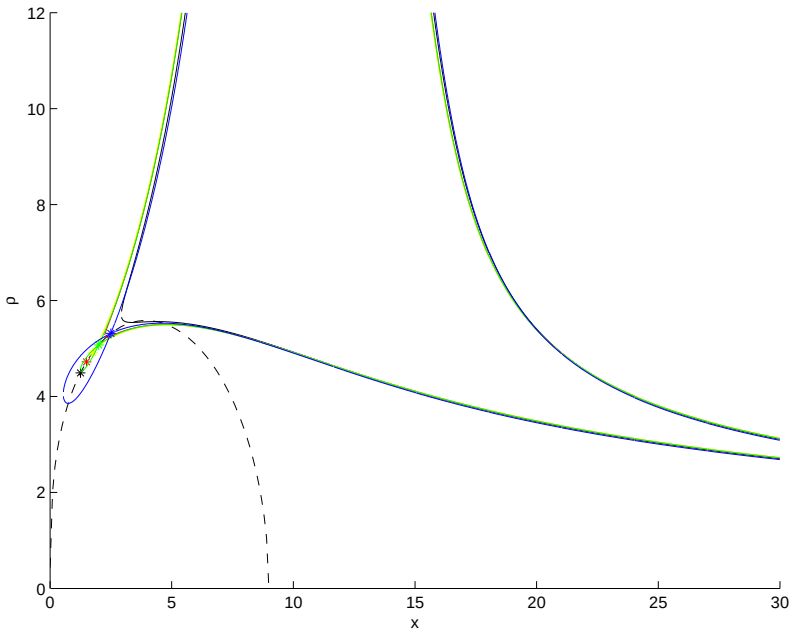

Figure 6.7: Zero Velocity Curves for Various Equilibrium Solutions. * = equilibrium solution at each C Energy Level. Dashed = Circular Orbit Equilibrium Solutions Curve. Black→Blue = Decreasing C Value.

The shape or curvature of the zero velocity curves is determined by the solar

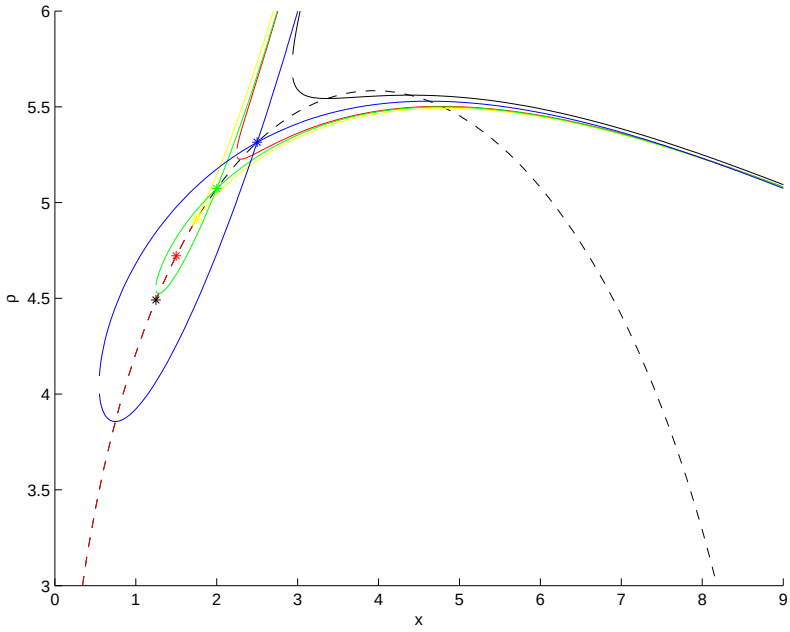

Figure 6.8: Detail of Zero Velocity Curves for Various Equilibrium Solutions. * = equilibrium solution at each C Energy Level. Dashed = Circular Orbit Equilibrium Solutions Curve. Black→Blue = Decreasing C Value.

radiation pressure magnitude, g. Larger values of g (which can occur for larger spacecraft surface area facing the Sun) will tend to straighten the upper portion of the zero velocity curve and shrink the area of allowable motion for a fixed value of h as seen in figure 6.10 for a system with constant h and ω and varied the solar radiation pressure magnitude.

The zero velocity curves are dependant on the heliocentric orbit. As the semi-major axis of the orbit decreases, the x offset range for the family of circular orbits as well as the stable region shrinks. Figure 6.11 illustrates how the zero velocity curves change for varying a values. Note that for a circular orbit at the same x offset distance for all three case, the larger the semimajor axis cases have a stable solution while the orbit closest to the Sun is unstable.

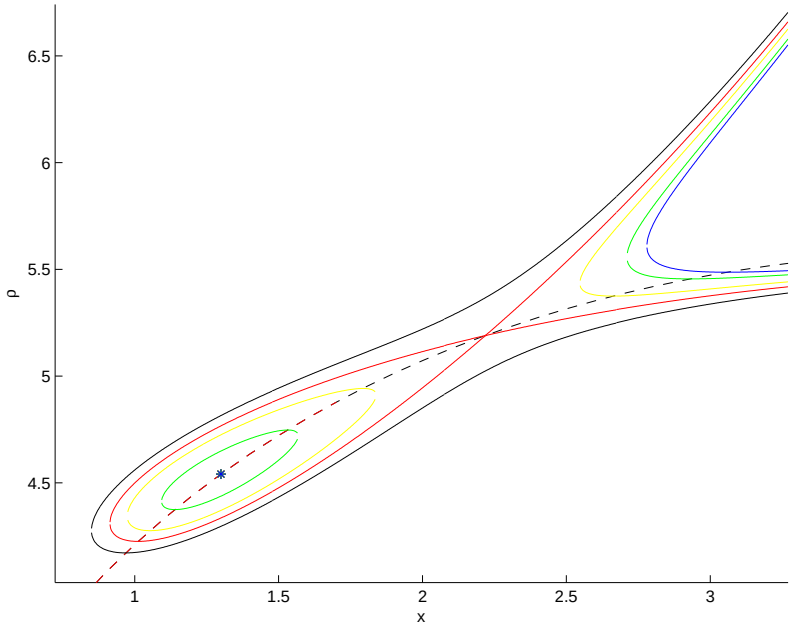

Figure 6.9: Zero Velocity Curves with Constant h. * = Equilibrium Solution at Each C Energy Level. Dashed = Circular Orbit Equilibrium Solutions Curve (Red = Stable. Black = Unstable). Black→Blue = Decreasing C Value.

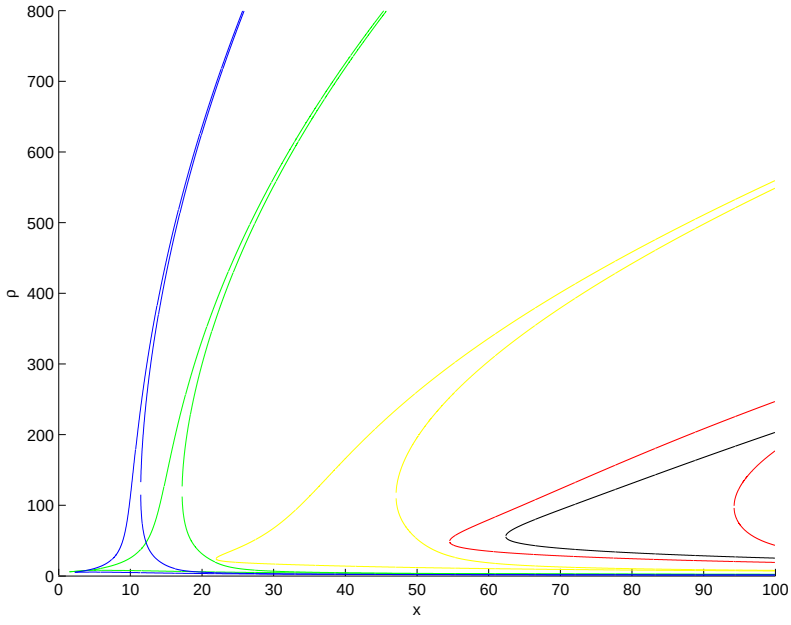

Figure 6.10: Zero Velocity Curves for Fixed ω varied g. Black→Blue = Increasing g Value.

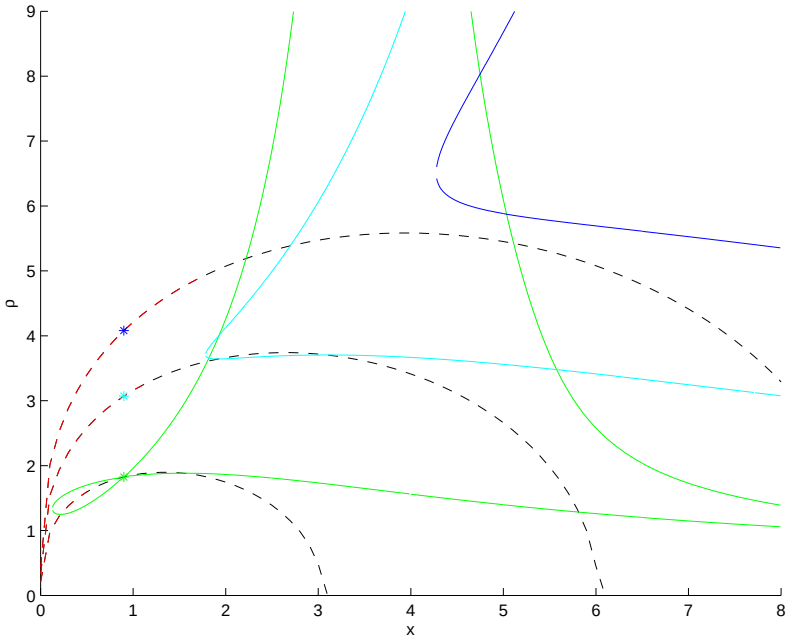

Figure 6.11: Zero Velocity Curves for Varying Semimajor Axis Values. Green (1 AU) →Blue (3 AU) = Increasing a Value.

The zero velocity curves appear to have an open shape, so it is only natural to determine if there exist any other conditions for the curves to close up and bound the motion of the spacecraft inside. First, consider the partial derivatives of the Jacobi integral:

$$\bar{J}_{\overline{x}} = \frac{\partial \bar{J}}{\partial \overline{x}} = -g - 3\omega^2 \overline{x} + \frac{\mu \overline{x}}{(\overline{\rho}^2 + \overline{x}^2)^{3/2}}, \tag{6.47}$$

$$\bar{J}_{\overline{\rho}} = \frac{\partial \bar{J}}{\partial \overline{\rho}} = -\frac{h^2}{\overline{\rho}^3} + \frac{1}{2}\omega^2 \overline{\rho} + \frac{\mu \overline{\rho}}{(\overline{\rho}^2 + \overline{x}^2)^{3/2}}. \tag{6.48}$$

To find a point of closure, $\bar{J}_{\overline{x}} = 0$ and $\bar{J}_{\overline{\rho}} = 0$ must hold. Note that equations 6.47 and 6.48 are exactly the conditions used to find the circular orbit equilibrium solutions. First consider the case of negligible solar radiation pressure, $g = 0$, these partial equations become:

$$-3\omega^2 \overline{x} + \frac{\mu \overline{x}}{(\overline{\rho}^2 + \overline{x}^2)^{3/2}} = 0, \tag{6.49}$$

$$-\frac{h^2}{\overline{\rho}^3}+\frac{1}{2}\omega^2\overline{\rho}+\frac{\mu\overline{\rho}}{(\overline{\rho}^2+\overline{x}^2)^{3/2}}=0. \tag{6.50}$$

Rearranging yields:

$$3\omega^2=\frac{\mu}{(\overline{\rho}^2+\overline{x}^2)^{3/2}}, \tag{6.51}$$

$$\frac{h^2}{\overline{\rho}^4}-\frac{1}{2}\omega^2=\frac{\mu}{(\overline{\rho}^2+\overline{x}^2)^{3/2}}. \tag{6.52}$$

By substitution, the following solution is found:

$$\overline{\rho}^4=\frac{2h^2}{7\omega^2}, \tag{6.53}$$

$$\overline{x}^2=\left(\frac{\mu}{3\omega^2}\right)^{2/3}-\sqrt{\frac{2}{7}}\frac{h}{\omega}. \tag{6.54}$$

Note that for a real valued solution to exist, $\overline{x}^2>0$. This condition on $\overline{x}$ becomes a condition on the angular momentum magnitude, h, for the system:

$$h<\left(\frac{\mu}{3\omega^2}\right)^{2/3}\sqrt{\frac{7}{2}}\omega. \tag{6.55}$$

Since we are mostly interested in the circular orbit equilibrium solutions, we can substitute $h=\overline{\rho}_0^2\dot{\overline{\theta}}_0$, using the solutions for $\overline{\rho}_0$ and $\dot{\overline{\theta}}_0$ into this condition and find the condition to be a function of $\overline{x}_0$:

$$\left(\left(\frac{\overline{x}_0\mu}{3\omega^2\overline{x}_0+g}\right)^{2/3}-\overline{x}_0^2\right)\left(\frac{7\omega^2}{2}+\frac{g}{\overline{x}_0}\right)<\left(\frac{\mu}{3\omega^2}\right)^{2/3}\sqrt{\frac{7}{2}}\omega. \tag{6.56}$$

If we now consider that the solar radiation pressure is non-negligible then the rearranged equations are:

$$3\omega^2+\frac{g}{\overline{x}}=\frac{\mu}{(\overline{\rho}^2+\overline{x}^2)^{3/2}}, \tag{6.57}$$

$$\frac{h^2}{\overline{\rho}^4}-\frac{1}{2}\omega^2=\frac{\mu}{(\overline{\rho}^2+\overline{x}^2)^{3/2}}. \tag{6.58}$$

These equations are the same as the conditions for the circular orbit equilibrium solutions. This implies that closure points occur at equilibrium solutions with the

same angular momentum magnitude as predicted by the zero velocity curves and that there do not exist any other closure points of the system allowing a spacecraft to escape in unbounded areas.

6.4 Stability of Averaged Equations of Motion

The zero velocity curves provide a graphical look at the stability of the system, we now verify these results analytically. To begin the averaged equations are linearized about a circular orbit equilibrium solution ($\overline{\rho}_0$, $\overline{x}_0$, and $\dot{\overline{\theta}}_0$ from the above relations) yielding the following linear equations with time invariant coefficients:

$$\delta\ddot{\overline{x}} = \left(\frac{3\overline{x}_0^2\mu}{\overline{r}_0^5} - \frac{\mu}{\overline{r}_0^3} + 3\omega^2\right)\delta\overline{x} + \left(\frac{3\overline{x}_0\overline{\rho}_0\mu}{\overline{r}_0^5}\right)\delta\overline{\rho}, \tag{6.59}$$

$$\delta\ddot{\overline{\rho}} = \left(\frac{3\overline{x}_0\overline{\rho}_0\mu}{\overline{r}_0^5}\right)\delta\overline{x} + \left(\frac{3\overline{\rho}_0^2\mu}{\overline{r}_0^5} - \frac{\mu}{\overline{r}_0^3} + \dot{\overline{\theta}}_0^2 - \frac{1}{2}\omega^2\right)\delta\overline{\rho} + (2\overline{\rho}_0\dot{\overline{\theta}}_0)\delta\dot{\overline{\theta}}, \tag{6.60}$$

$$\delta\ddot{\overline{\theta}} = \left(\frac{2\dot{\overline{\rho}}_0\dot{\overline{\theta}}_0}{\overline{\rho}_0^2}\right)\delta\overline{\rho} + \left(\frac{-2\dot{\overline{\theta}}_0}{\overline{\rho}_0}\right)\delta\dot{\overline{\rho}} + \left(\frac{-2\dot{\overline{\rho}}_0}{\overline{\rho}_0}\right)\delta\dot{\overline{\theta}}. \tag{6.61}$$

Note that for a circular orbit, $\dot{\overline{\rho}}_0 = 0$ therefore equation 6.61 becomes:

$$\delta\ddot{\overline{\theta}} = \left(\frac{-2\dot{\overline{\theta}}_0}{\overline{\rho}_0^2}\right)\delta\dot{\overline{\rho}}. \tag{6.62}$$

For notational simplicity, these equations are rewritten as:

$$\delta\ddot{\overline{x}} = a\delta\overline{x} + b\delta\overline{\rho}, \tag{6.63}$$

$$\delta\ddot{\overline{\rho}} = c\delta\overline{x} + d\delta\overline{\rho} + e\delta\dot{\overline{\theta}}, \tag{6.64}$$

$$\delta\ddot{\overline{\theta}} = f\delta\dot{\overline{\rho}}, \tag{6.65}$$

where a, b, c, d, e, f are defined by the original linearized averaged equations and $c = b$. In state space form, the linearized averaged equations are:

$$\begin{pmatrix} \delta\dot{\overline{x}} \\ \delta\dot{\overline{\rho}} \\ \delta\dot{\overline{\theta}} \\ \delta\ddot{\overline{x}} \\ \delta\ddot{\overline{\rho}} \\ \delta\ddot{\overline{\theta}} \end{pmatrix} = \begin{pmatrix} 0 & 0 & 0 & 1 & 0 & 0 \\ 0 & 0 & 0 & 0 & 1 & 0 \\ 0 & 0 & 0 & 0 & 0 & 1 \\ a & b & 0 & 0 & 0 & 0 \\ b & d & 0 & 0 & 0 & e \\ 0 & 0 & 0 & 0 & f & 0 \end{pmatrix} \begin{pmatrix} \delta\overline{x} \\ \delta\overline{\rho} \\ \delta\overline{\theta} \\ \delta\dot{\overline{x}} \\ \delta\dot{\overline{\rho}} \\ \delta\dot{\overline{\theta}} \end{pmatrix}, \tag{6.66}$$

$$\dot{\overline{\mathbf{X}}} = \mathbf{A}\overline{\mathbf{X}}. \tag{6.67}$$

To determine the spectral stability of this system, let's examine the eigenvalues of the $\mathbf{A}$ matrix, which are determined by its characteristic polynomial:

$$\lambda^6 + (-a - d - ef)\lambda^4 + (-b^2 + ad + aef)\lambda^2 = 0. \tag{6.68}$$

It is obvious from the characteristic polynomial that there exist two eigenvalues at 0. Therefore, the system is by definition unstable, but the eigenvector associated with the zero eigenvalues is $(0, 0, 1, 0, 0, 0)$ or the θ direction, which does not affect the stability of the circular orbit but only yields a downtrack drift. Therefore, the other eigenvalues need to be used to determine the stability of the orbit. Eliminating the zero roots of the characteristic polynomial results in:

$$\lambda^4 + (-a - d - ef)\lambda^2 + (-b^2 + ad + aef) = 0, \tag{6.69}$$

which has the roots:

$$\lambda = \pm\sqrt{\frac{(a + d + ef) \pm \sqrt{(4b^2 + (-a + d + ef)^2)}}{2}}, \tag{6.70}$$

where

$$(4b^2 + (-a + d + ef)^2) = \frac{36\mu^2\overline{x}_0^2\overline{\rho}_0^2}{(\overline{x}_0^2 + \overline{\rho}_0^2)^5} + \left(3\dot{\overline{\theta}}_0^2 + \frac{3\mu(\overline{x}_0 - \overline{\rho}_0)(\overline{x}_0 + \overline{\rho}_0)}{(\overline{x}_0^2 + \overline{\rho}_0^2)^{5/2}} + \frac{7\omega^2}{2}\right)^2 > 0, \tag{6.71}$$

$$(a + d + ef) = -3\dot{\overline{\theta}}_0^2 + \frac{\mu}{(\overline{x}_0^2 + \overline{\rho}_0^2)^{3/2}} + \frac{5\omega^2}{2}. \tag{6.72}$$

With two of these roots always having positive signs, only purely imaginary roots will allow for a stable solution and they depend on the comet's specific orbit. Therefore to have purely imaginary roots, the following condition needs to hold for the comet's orbit:

$$(a + d + ef) < -\sqrt{4b^2 + (-a + d + ef)^2}, \tag{6.73}$$

since $\sqrt{4b^2 + (-a + d + ef)^2} > 0$ always.

As an example, figure 6.12 illustrates the stable and unstable circular orbit equilibrium solutions based on this analysis. The eigenvalues are indeed either zero or purely imaginary for the stable solutions.

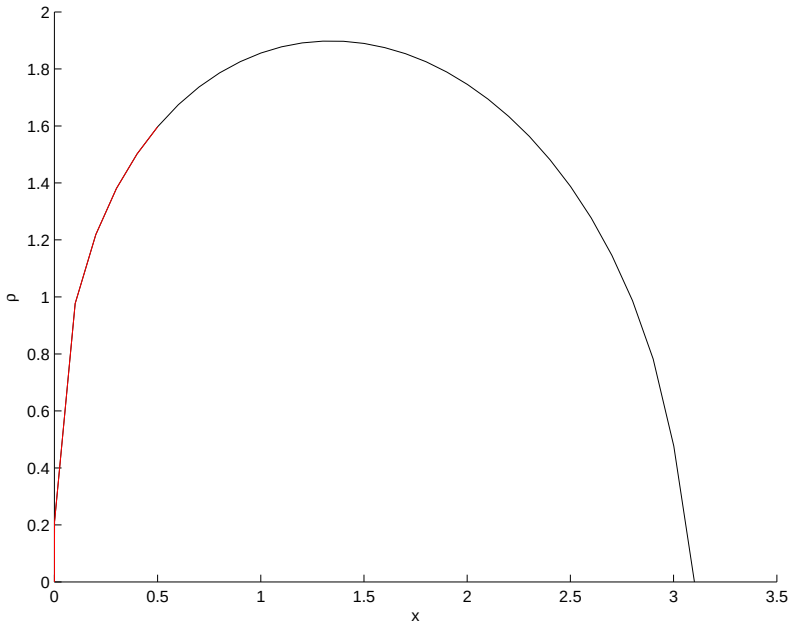

Figure 6.12: Possible Circular Orbit Solutions as a Function of x from averaged equations. Red = Stable. Black = Unstable.

To test this stability criteria, example simulations of stable and unstable solutions as determined by equation 6.73 were performed and their trajectories were plotted on the appropriate zero-velocity curve. Figure 6.13 shows a stable trajectory remaining close to the equilibrium point. Note that the zero-velocity curves are computed for the averaged equations with a slightly different energy (a result of terms which have been averaged out) from the non-averaged equations yielding a curve around the averaged equilibrium solution instead of a single point. Figure 6.14 shows an unstable trajectory wandering far from the equilibrium point as expected and eventually escaping. These results provide an analytical method of determining stable orbits in the Hill rotating system about a small body under solar radiation pressure. In general, the stable orbits exist near the body (small x offset).

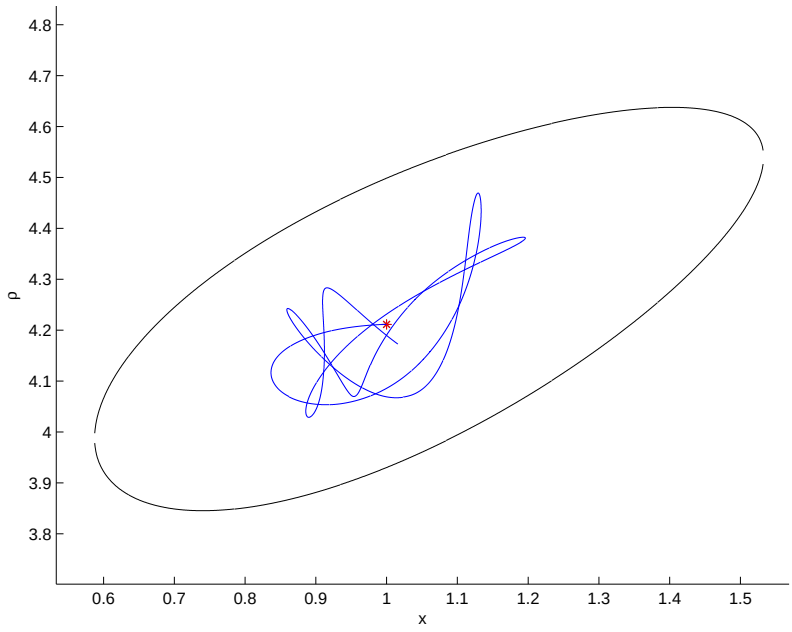

Figure 6.13: Stable Trajectory Plotted on Zero Velocity Curves. Blue = Trajectory. Black = Trajectory Zero velocity Curve. Red = Averaged Equilibrium Zero Velocity Curve.

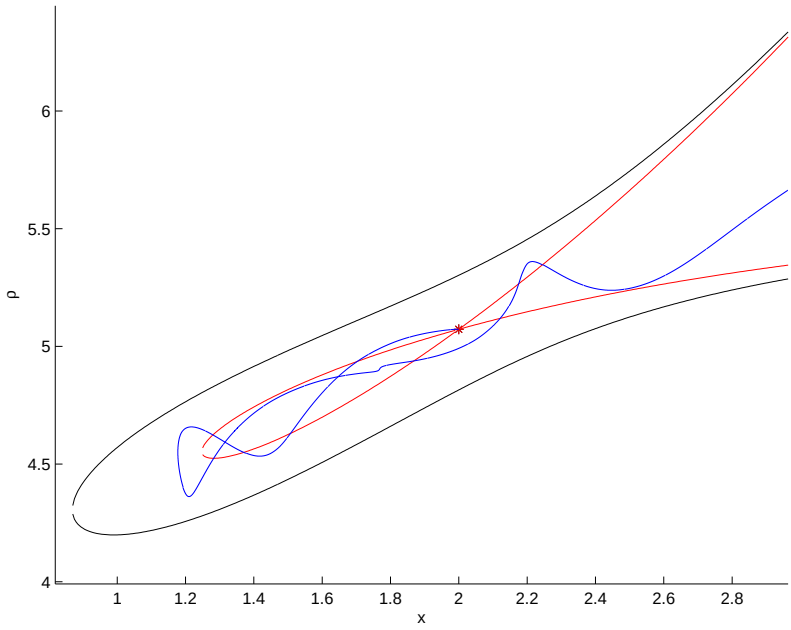

Figure 6.14: Unstable Trajectory Plotted on Zero Velocity Curves. Blue = Trajectory. Black = Trajectory Zero velocity Curve. Red = Averaged Equilibrium Zero Velocity Curve.

6.4.1 Stability in Presence of Outgassing Jet

Until this point, the analysis presented could be applied to any small body without disturbing forces other than solar radiation pressure. Lets shift our focus to a comet with outgassing jets which produce a varied pressure field in the vicinity of the comet nucleus. The acceleration due to an outgassing jet will be considered as a radial force with the acceleration vector defined as[32]:

$$\vec{a}_{oj} = \frac{A_{og}}{|\vec{r}|^3}\vec{r}, \tag{6.74}$$

where A_{og} is the strength of the outgassing jet. The new equations of motion become:

$$\ddot{\vec{r}}_I = \frac{\partial U}{\partial \vec{r}_I} + g\hat{x} + \vec{a}_{oj}. \tag{6.75}$$

When broken down into cylindrical coordinates, it becomes obvious that only the x and ρ directions are affected by the outgassing jet's acceleration.

$$\ddot{x} = 2\omega(\dot{\rho}\cos\theta - \rho\dot{\theta}\sin\theta) + 3\omega^2 x + g - \frac{x\mu}{r^3} + \frac{xA_{og}}{r^3}, \tag{6.76}$$

$$\ddot{\rho} = -2\dot{x}\omega\cos\theta + \rho\dot{\theta}^2 - \rho\omega^2\sin^2\theta - \frac{\rho\mu}{r^3} + \frac{\rho A_{og}}{r^3}, \tag{6.77}$$

$$\rho\ddot{\theta} = 2\dot{x}\omega\sin\theta - 2\dot{\rho}\dot{\theta} - \rho\omega^2\sin\theta\cos\theta. \tag{6.78}$$

Therefore the new Jacobi integral is:

$$J_{og} = \frac{1}{2}(\dot{x}^2 + \dot{\rho}^2 + \rho^2\dot{\theta}^2) - \frac{\mu}{r} - \frac{1}{2}\omega^2(3x^2 - \rho^2\sin(\theta)^2) - gx + \frac{A_{og}}{r}. \tag{6.79}$$

Averaging this over θ as before yields:

$$\bar{J}_{og} = \frac{1}{2}(\dot{\bar{x}}^2 + \dot{\bar{\rho}}^2) - \frac{\mu}{\bar{r}} - \frac{1}{2}\omega^2(3\bar{x}^2 - \frac{1}{2}\bar{\rho}^2) - g\bar{x} + \frac{h^2}{2\bar{\rho}^2} + \frac{A_{og}}{\bar{r}}. \tag{6.80}$$

If we consider that the spacecraft passes through an outgassing jet's pressure field, we can determine a bound on the strength of the jet for which the spacecraft is contained within an area about stable equilibrium solutions. As determined previously,

the stable equilibrium solution has a conjugate h-valued unstable equilibrium solution which defined the closure point on the zero velocity curve with increased energy. Define C_s as the energy associated with a stable equilibrium solution having angular momentum magnitude, h, and C_u as the energy associated with the conjugate unstable equilibrium solution. Therefore the condition $C_s \leq C_{og} \leq C_u$, where C_{og} is the energy while within an outgassing jet, must hold to keep a spacecraft bounded near the stable equilibrium. This implies a bound on the outgassing magnitude, A_{og}:

$$\frac{A_{og}}{\overline{r}} \leq C_u - C_s, \tag{6.81}$$

or

$$A_{og} \leq (C_u - C_s)\overline{r}. \tag{6.82}$$

Therefore, if the strength of an outgassing jet, A_{og}, can be estimated, this bound gives insight into whether the spacecraft will remain trapped in the vicinity of the stable equilibrium. For example, figure 6.15 illustrates the trajectory of a spacecraft which has passed though an outgassing jet with a magnitude which does not violate the criteria and allows for the spacecraft to remain bounded near the equilibrium solution. The magnitude of the outgassing jet in figure 6.16 is too large and forces an instability in the orbit allowing it to escape.

Ellipsoidal Body Effects

Since comet bodies are rarely spherical or produce point mass gravity, let's now consider the effect an ellipsoidal body has on this type of orbit. Using the method in Broschart et al.[33] for finding the gravitational force, the effect of an ellipsoidal comet body was incorporated into the equations of motion. For comparison, the μ value was kept constant by using a biaxial ellipsoid body and varying the radius of one of the sides. The comet rotational period was set to 12 hours with constant spin

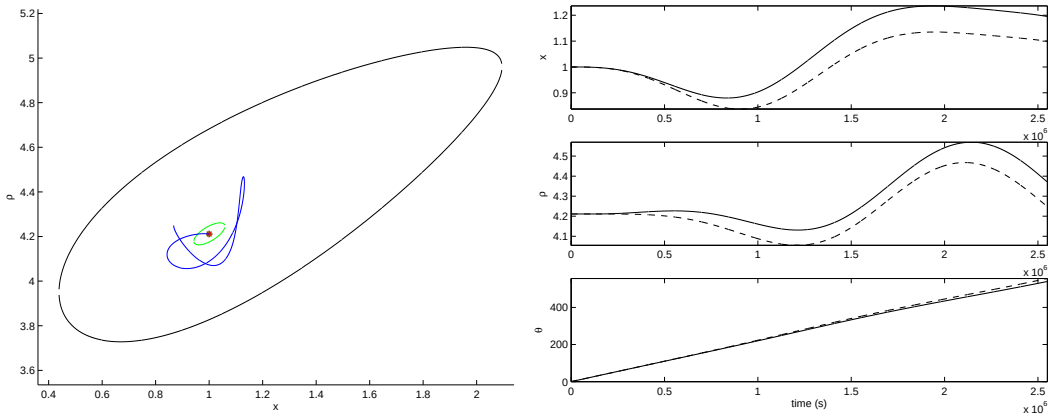

Figure 6.15: Stable Trajectory in the Presence of an Outgassing Jet on Appropriate Zero Velocity Curve (Two Jet Passages). Blue = Trajectory. Black = Zero velocity Curve with Outgassing. Black = Zero velocity Curve without Outgassing. Shown with Position Components. Solid = Trajectory with Outgassing. Dashed = Trajectory Without Outgassing.

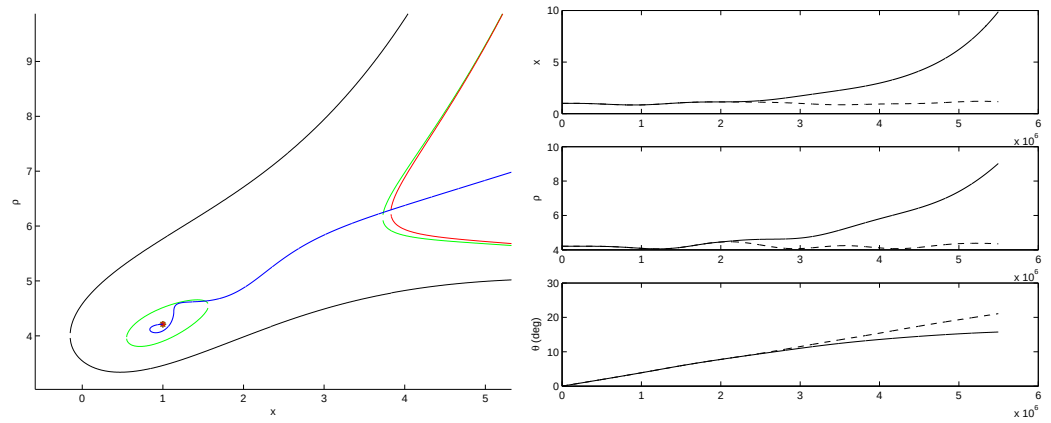

Figure 6.16: Unstable Trajectory in the Presence of an Outgassing Jet on Appropriate Zero Velocity Curve (Two Jet Passages). Blue = Trajectory. Black = Zero velocity Curve with Outgassing. Black = Zero velocity Curve without Outgassing. Shown with Position Components. Solid = Trajectory with Outgassing. Dashed = Trajectory Without Outgassing.

about the z axis. For a varied radius in the orbital plane (with initial position of longest radius aligned along the x direction as shown in the figures and identical initial conditions for the spacecraft across the simulations), figures 6.18 to 6.20 show the deviation from the spherical model, figure 6.17. As expected, the more ellipsoidal the body becomes, the more the trajectory deviates from the spherical body's trajectory (seen in figure 6.21) until it appears to become unstable and escape the vicinity of the circular orbit as in figure 6.20, although the stability was not analytically verified.

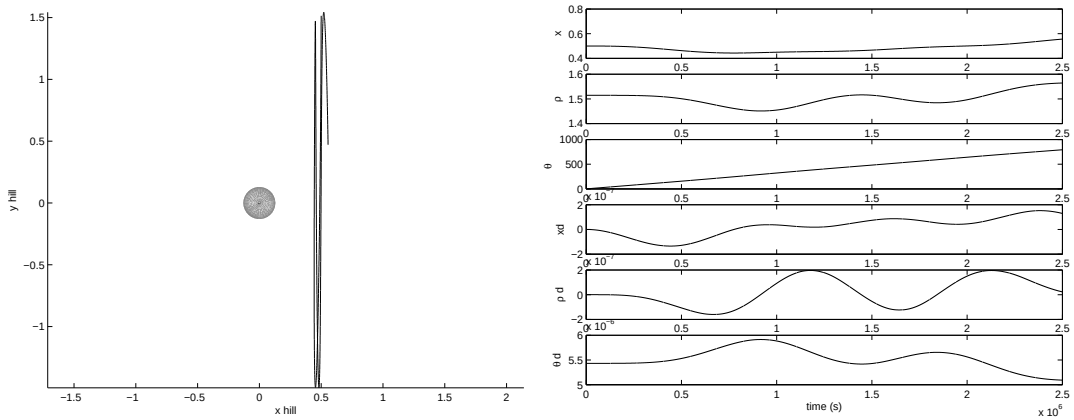

Figure 6.17: Orbit with Initial Offset of $x = 0.5$km with Spherical Comet Body of Radius 0.129 km. Solid = Trajectory.

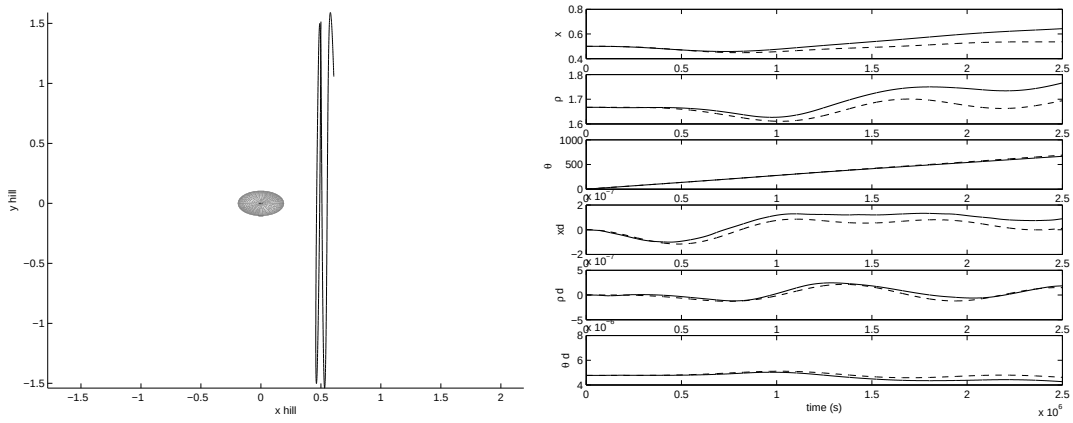

Figure 6.18: Orbit with Initial Offset of $x = 0.5$km with Ellipsoidal Body with Radii 0.193, 0.105, and 0.105 km. Solid = Trajectory. Dashed = Trajectory Assuming a Spherical Body.

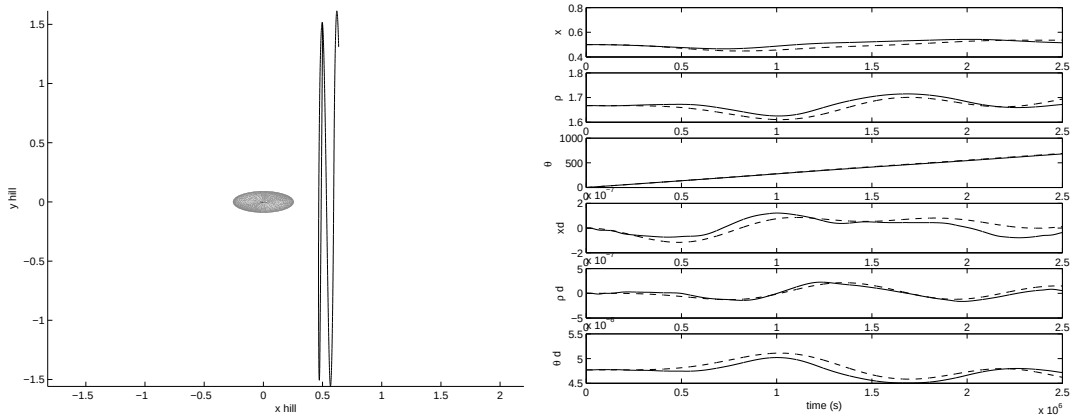

Figure 6.19: Orbit with Initial Offset of $x = 0.5$km with Ellipsoidal Body with Radii 0.258, 0.091, and 0.091 km. Solid = Trajectory. Dashed = Trajectory Assuming a Spherical Body.

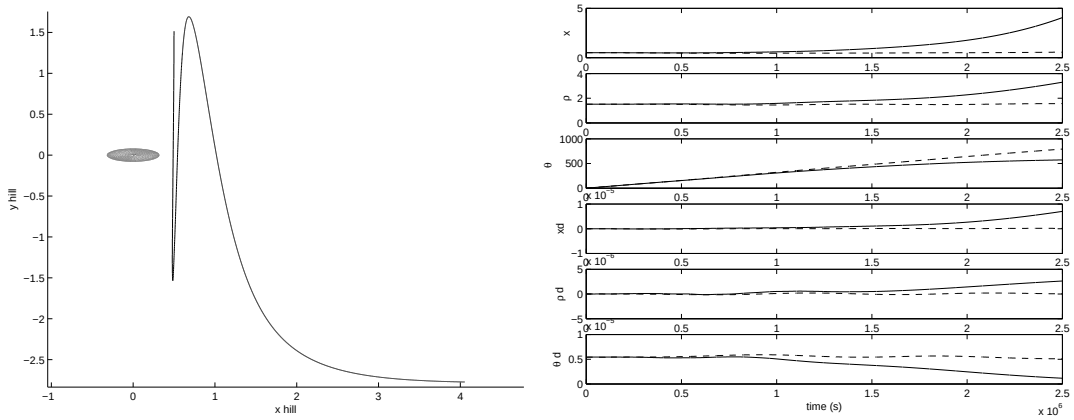

Figure 6.20: Orbit with Initial Offset of $x = 0.5$km with Ellipsoidal Body with Radii 0.322, 0.082, and 0.082 km. Solid = Trajectory. Dashed = Trajectory Assuming a Spherical Body.

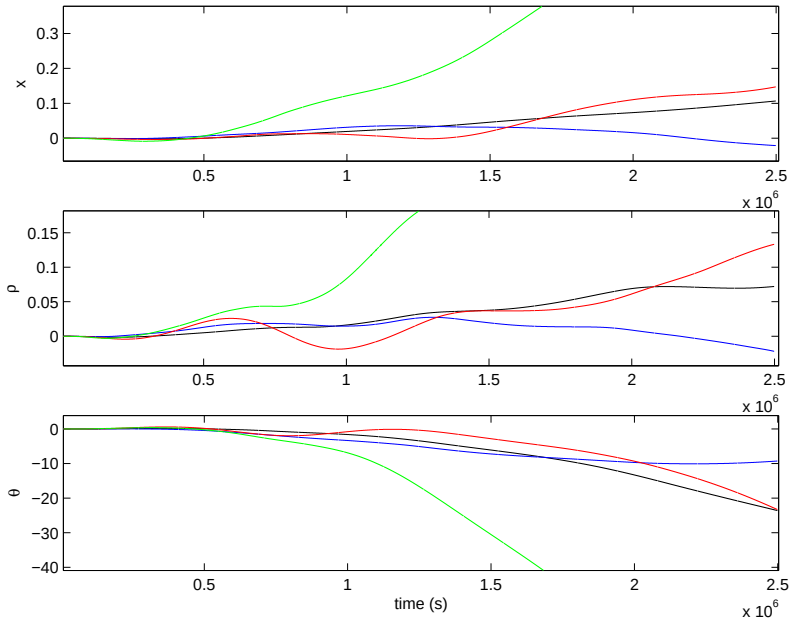

Figure 6.21: Comparison of Effects of Ellipsoidal Body with Radii in the Plane Varied. Black→ Blue → Red→ Green = Increasingly Ellipsoidal.

If the ellipsoidal radius is varied in the out of orbital plane direction, as in figure 6.22 through 6.26, the trajectory appears to remain stable for a more ellipsoidal body then for the case of the body varied in plane. Figure 6.27 shows the deviations of the trajectories from the spherical model (figure 6.17) illustrating that this configuration allows for the spacecraft to remain in a stable orbit for a more elongated body then when the comet is elongated in the plane.

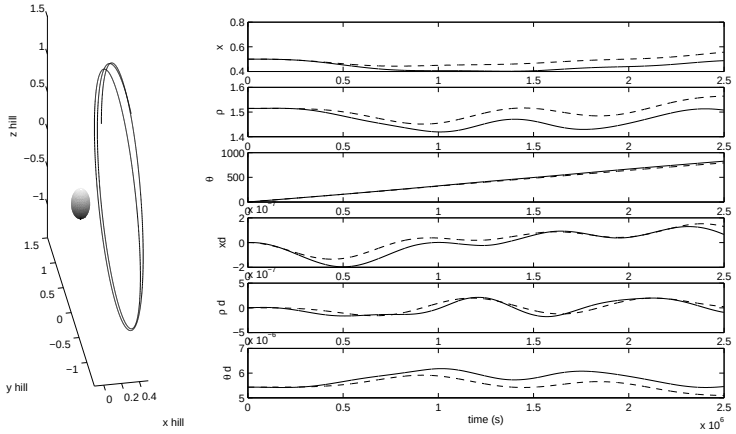

Figure 6.22: Orbit with Initial Offset of $x = 0.5$km with Ellipsoidal Body with Radii 0.105, 0.105, and 0.193 km. Solid = Trajectory. Dashed = Trajectory Assuming a Spherical Body.

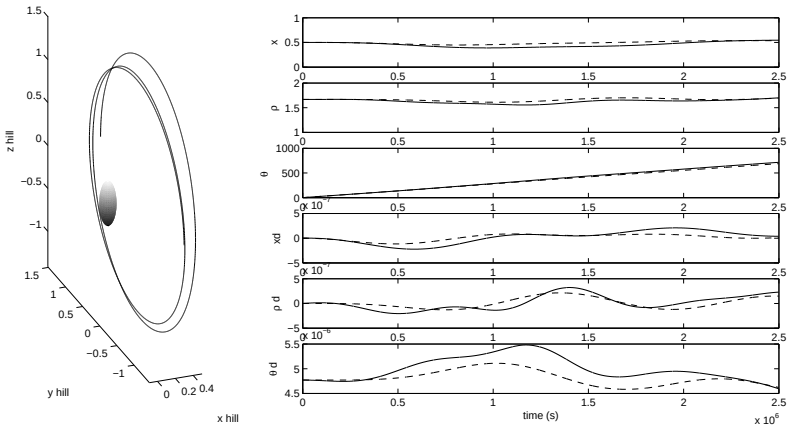

Figure 6.23: Orbit with Initial Offset of $x = 0.5$km with Ellipsoidal Body with Radii 0.091, 0.091, and 0.258 km. Solid = Trajectory. Dashed = Trajectory Assuming a Spherical Body.

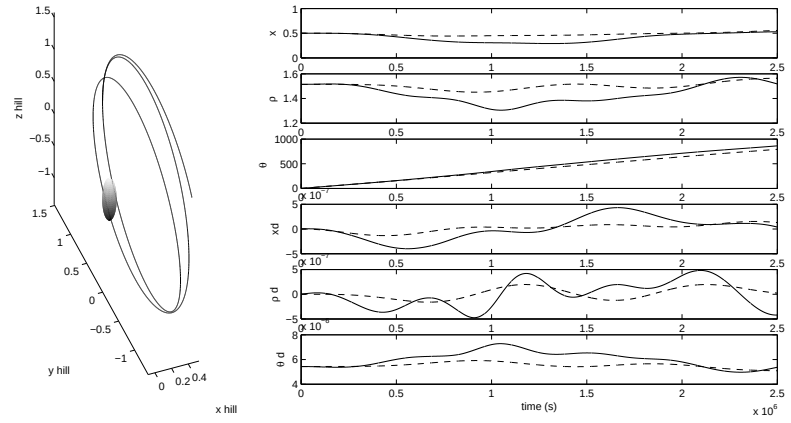

Figure 6.24: Orbit with Initial Offset of $x = 0.5$km with Ellipsoidal Body with Radii 0.082, 0.082, and 0.322 km. Solid = Trajectory. Dashed = Trajectory Assuming a Spherical Body.

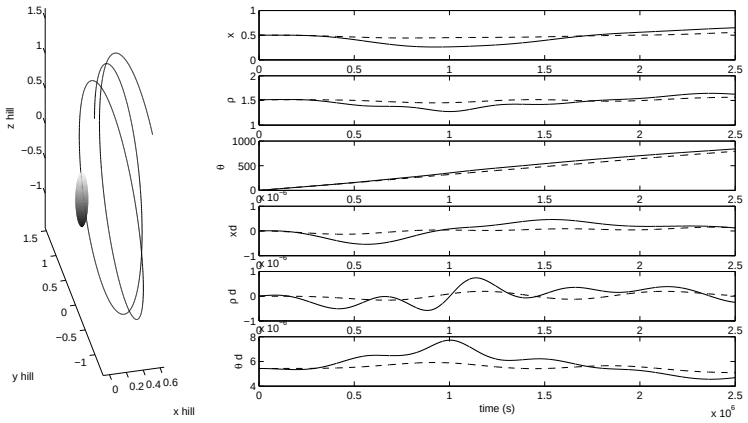

Figure 6.25: Orbit with Initial Offset of $x = 0.5$km with Ellipsoidal Body with Radii 0.074, 0.074, and 0.388 km. Solid = Trajectory. Dashed = Trajectory Assuming a Spherical Body.

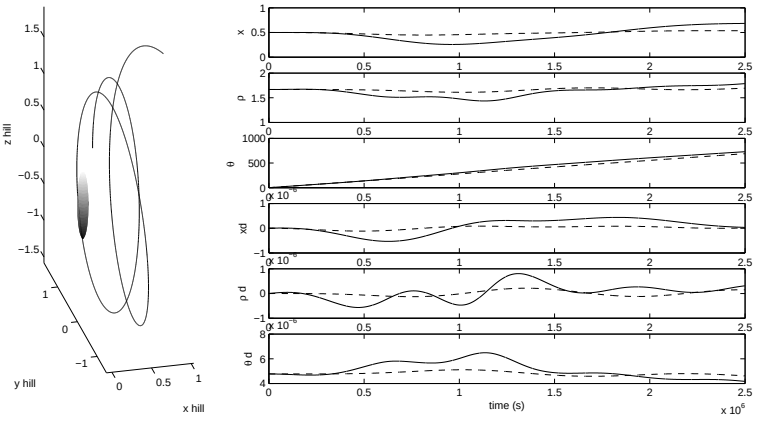

Figure 6.26: Orbit with Initial Offset of $x = 0.5$km with Ellipsoidal Body with Radii 0.069, 0.069, and 0.451 km. Solid = Trajectory. Dashed = Trajectory Assuming a Spherical Body.

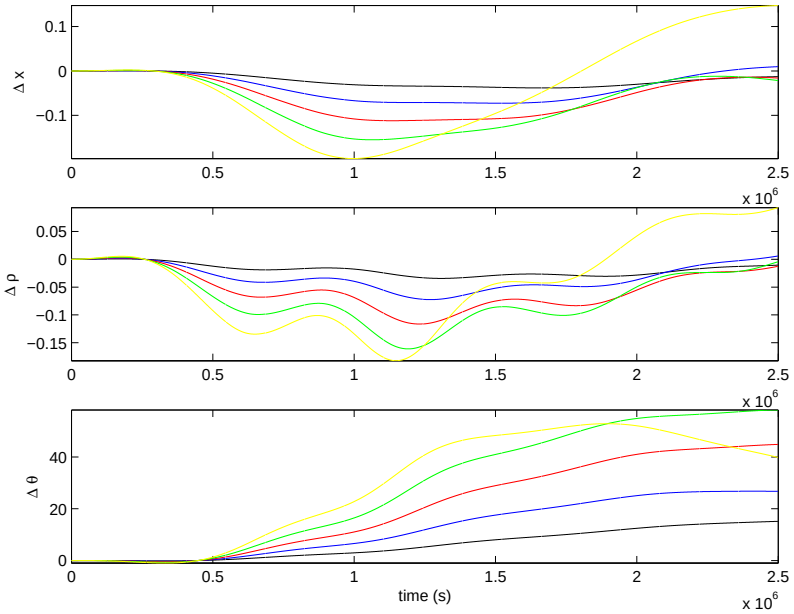

Figure 6.27: Comparison of Effects of Ellipsoidal Body with Radii out of the Plane Varied. Black→ Blue → Red→ Green→ Yellow = Increasingly Ellipsoidal.

Since these simulations all assumed an identical initial circular orbit which is close to the comet body and within the stable region, we now consider how the initial x offset of the circular orbit is affected by an ellipsoidal body. To produce a wider stable x offset region, a larger body will be considered for these comparisons. We consider a single ellipsoid body with lengths 1, 0.253, and 0.253 km and vary the initial x offset to determine the effects of the ellipsoidal body, as seen in figures 6.28 though 6.31. As expected, figure 6.32 shows that the ellipsoidal body effects lessen and the position components appear to converge as the initial x offset of the circular orbit increases.

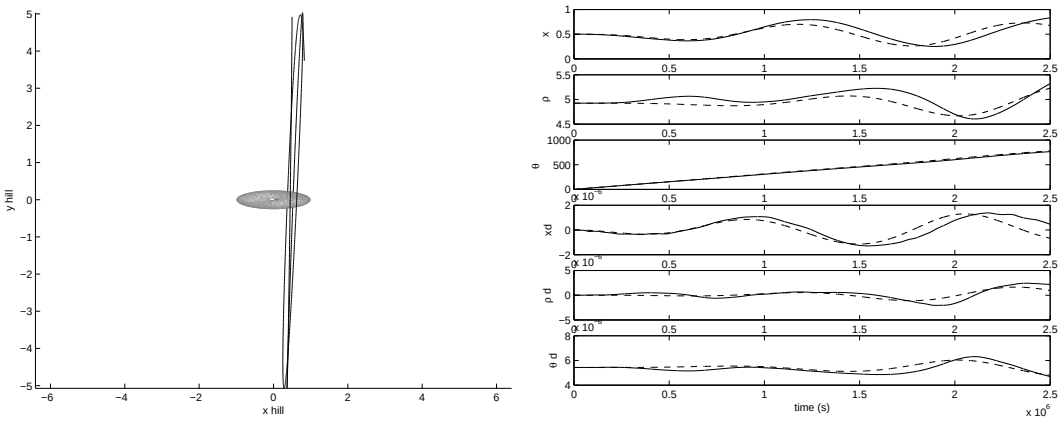

Figure 6.28: Orbit with Initial Offset of $x = 0.5$km with Ellipsoidal Body with Radii 1, 0.253, and 0.253 km. Solid = Trajectory. Dashed = Trajectory Assuming a Spherical Body.

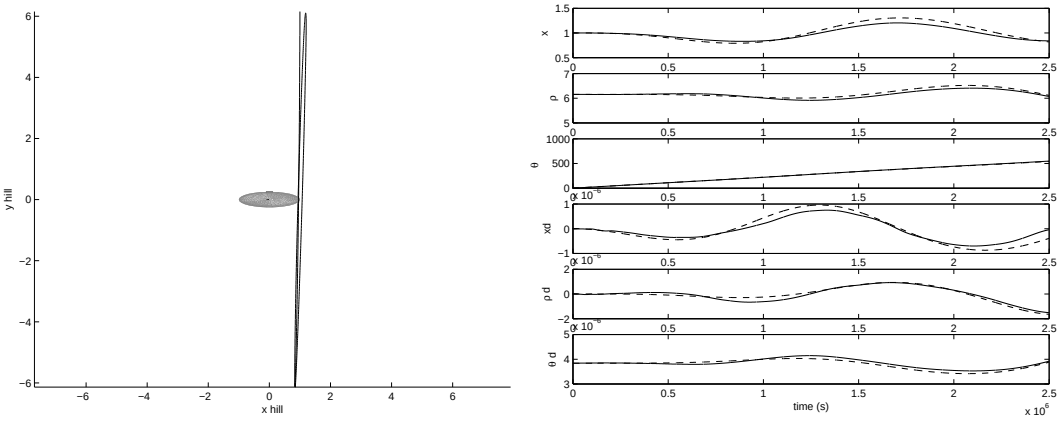

Figure 6.29: Orbit with Initial Offset of $x = 1.0$km with Ellipsoidal Body with Radii 1, 0.253, and 0.253 km. Solid = Trajectory. Dashed = Trajectory Assuming a Spherical Body.

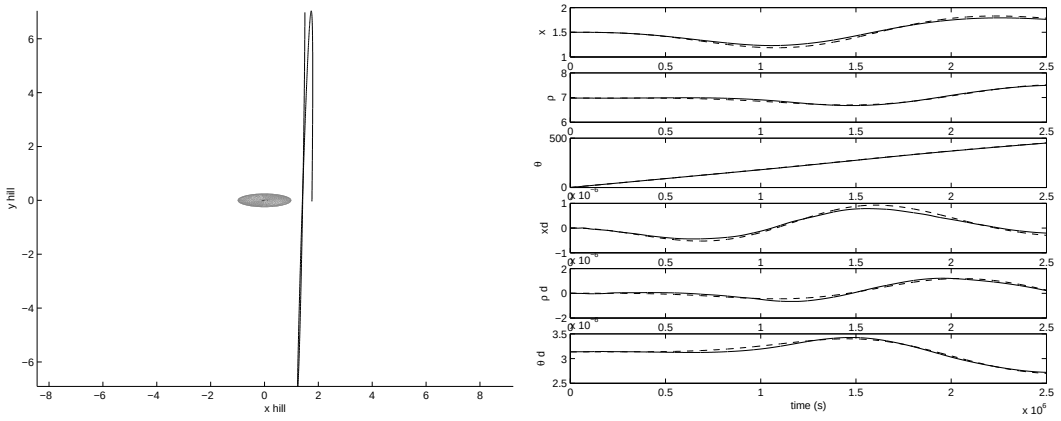

Figure 6.30: Orbit with Initial Offset of $x = 1.5$km with Ellipsoidal Body with Radii 1, 0.253, and 0.253 km. Solid = Trajectory. Dashed = Trajectory Assuming a Spherical Body.

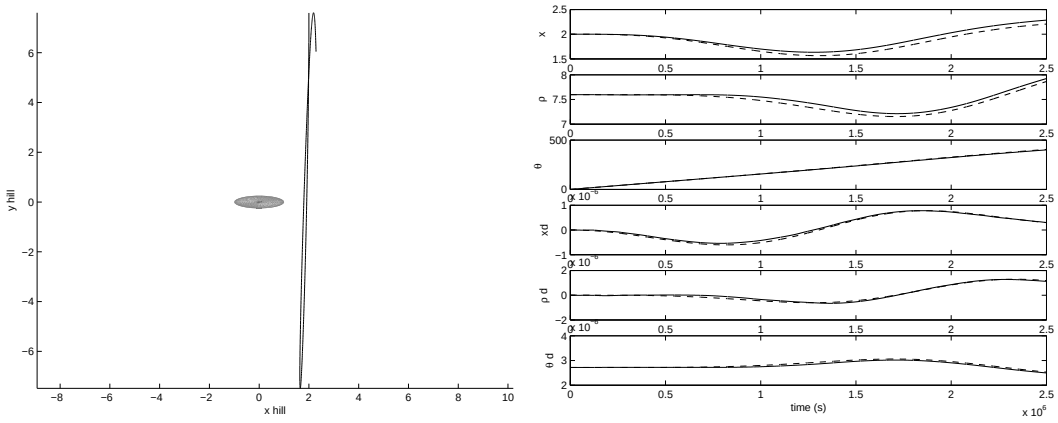

Figure 6.31: Orbit with Initial Offset of $x = 2.0$km with Ellipsoidal Body with Radii 1, 0.253, and 0.253 km. Solid = Trajectory. Dashed = Trajectory Assuming a Spherical Body.

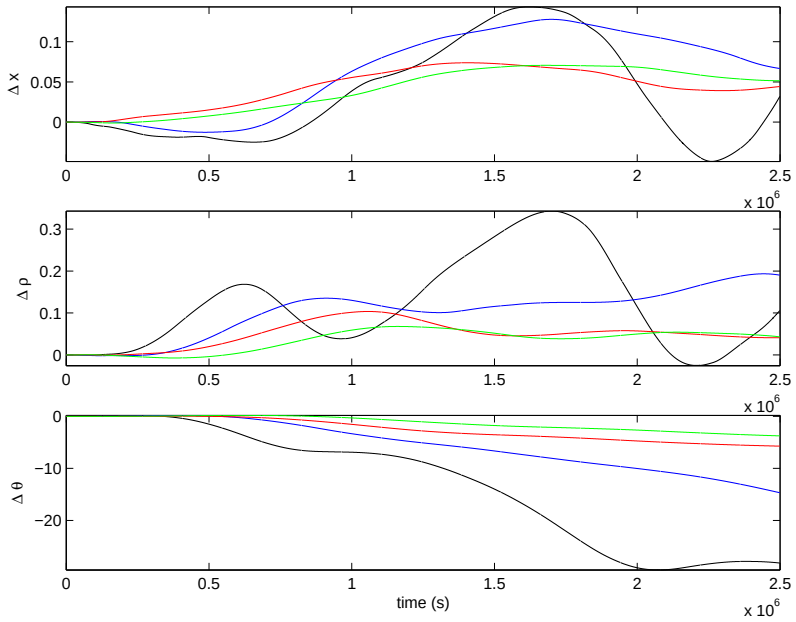

Figure 6.32: Comparison of Effects of Ellipsoidal Body with Radii 1, 0.253, and 0.253 km and Varied x Offset. Black→ Blue → Red→ Green = Increasing x Offset.

For comparison to the simulations in chapter IV, the idealized comet body for Wild 2 was tested. Figure 6.33 shows the trajectory and the difference in position components (compared to a spherical body with the same gravitational parameter, μ) for a spacecraft in orbit about the Wild 2. Note that since this body is much larger in size then the previous bodies considered, the initial circular orbit is also much larger with an initial offset of 4 km and radius of 53 km.

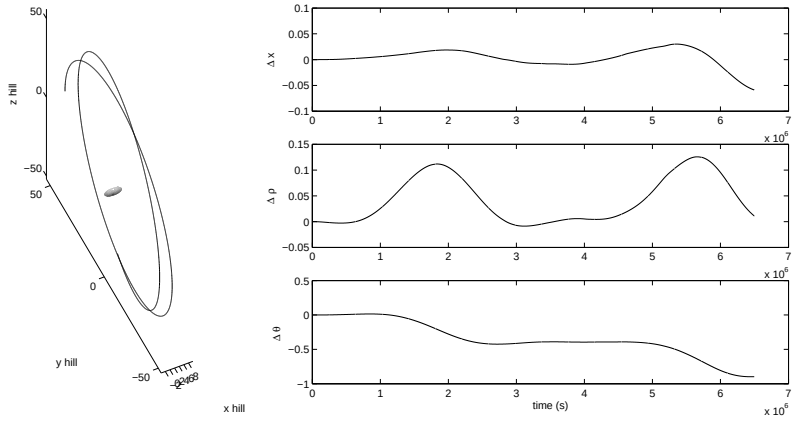

Figure 6.33: Orbit with Initial Offset of $x = 4.0$km on Idealized Wild2 Ellipsoidal Body with Radii 2.7, 1.9, and 1.5 km. Solid = Difference in Trajectory Components from a Spherical Body.

6.5 Summary

In this chapter, the effects of the heliocentric motion about the Sun using the Hill three-body problem are examined. We have shown that on average Sun synchronous circular orbits offset from the center of mass of the comet body exist in the Hill equations of motion when solar radiation pressure is present. The stability of these orbits were determined through the construction of zero velocity curves and verified using spectral stability analysis. In direct connection to the topic of this thesis, a bound on the outgassing magnitude was determined such that the stability of an

orbit is maintained as a spacecraft passes though a jet field. This bound only allows for the spacecraft to remain in a stable orbit which is not necessarily the original orbit it was following or even in the vicinity of the original orbit. The number of passages through jet fields (either the same one or multiple different ones) has no limit as long as the outgassing magnitude for each jet remains within the given bound. An ellipsoidal body was then incorporated into the equations of motion to determine the effect on the identified stable orbits. Different effects were explored by varying the radii of the ellipsoidal body and changing it's orientation to the orbits. As expected, the more non-spherical the body became the larger the deviation from the nominal spherical body became. Also, as the spacecraft orbit is located farther from the body, the less the ellipsoidal body affected the deviation from the nominal.

CHAPTER VII

Restricted Orbital Motion

Since it has been shown that stable orbits exist, we now consider controlling these orbits. Orbits that are restricted to an interval of θ on the comet's terminator would be useful for monitoring the comet's surface at sunrise or sunset, where interesting surface activity occurs. Several control schemes are presented to restrict the motion of an orbiting spacecraft using a one or two dimensional surface to define the boundary of the allowable orbit. Different control boundaries will be considered when developing a control scheme. The first case is for the motion to be restricted by an angle in the cylindrical coordinate formulation of the equations of motion. This produces a long wedge shaped allowable area with the possibility of impact with the nucleus. Finally, boundaries defined by both an angle and a minimum radius which also restrict impacting are tested. In each case, an acceleration is applied when the spacecraft violates the defined boundary to push the spacecraft back into the allowable motion area[33]. Both impulsive and finite burn control schemes are explored with the addition of outgassing accelerations and gravitational perturbations from an ellipsoidal body.

7.1 Impulsive Maneuvers

For our initial analysis we consider a theoretical control method that is commonly used to test the feasibility of the control boundaries, an impulsive thrust. First consider the case where a Δv is applied to reverse the direction of the full velocity vector while holding the magnitude constant. This will reverse the motion of the spacecraft, ideally retracing its orbital path. This result, as seen in figure 7.1, does not maintain the orbit perpendicular to the Sun line, evidenced by the drift in x in figure 7.1, although the impulsive maneuver is successful at not violating the boundaries.

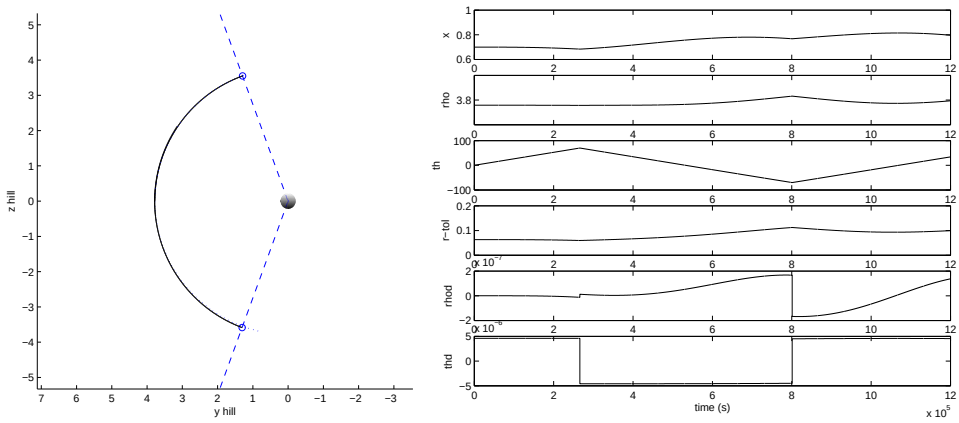

Figure 7.1: Orbit Control with Full Reversed Velocity Impulse with Angle Boundary. Solid = Controlled Trajectory. Blue = Angle Boundary. o = Impulse Location. Position and Velocity Components of the Controlled Orbit are Also Plotted for Reference.

Since the reversal of the full velocity vector performs poorly at maintaining the orbit's attitude, we consider the same impulse maneuver except only reverse the $\dot{y}$ and $\dot{z}$ components (or $\dot{\rho}$ and $\dot{\theta}$ components). This result, as seen in figure 7.2, also does not maintain the orbit perpendicular to the Sun line but has less deviation than the full velocity reversed maneuver.

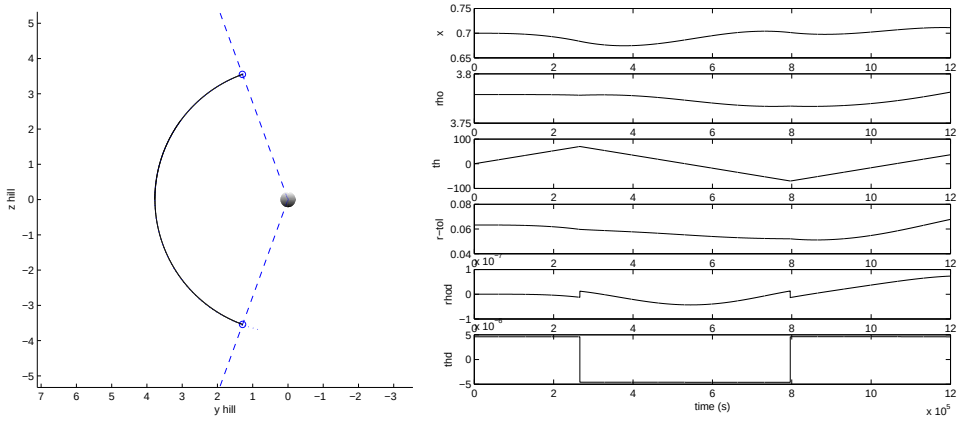

Figure 7.2: Orbit Control with Reversed θ and ρ Velocity Impulse with Angle Boundary. Solid = Controlled Trajectory. Blue = Angle Boundary. o = Impulse Location. Position and Velocity Components of the Controlled Orbit are Also Plotted for Reference.

Finally lets consider once again the exact same impulse maneuver except only reverse the $\dot{\theta}$ component:

$$\Delta v = v_+ - v_- = \rho_+\dot{\theta}_+ - \rho_-\dot{\theta}_-, \tag{7.1}$$

where $\rho_+ = \rho_- = \rho$ and $\dot{\theta}_+ = -\dot{\theta}_- = \dot{\theta}$ resulting in:

$$\Delta v = 2\rho\dot{\theta}. \tag{7.2}$$

This would ideally result in a final velocity of $-\rho\dot{\theta}$. This control impulse, as seen in figure 7.3, maintains the x offset similar to the $\dot{\rho}$ and $\dot{\theta}$ reversal but does not maintain the ρ component as well.

Figure 7.4 shows a comparison of the three impulsive schemes for the angle boundary. It is clear that the reversal of the $\dot{\rho}$ and $\dot{\theta}$ velocity components is the best of the three at maintaining the orbit across all three position components.

The drawback to the boundary defined by angles is that the spacecraft can be contained within the bounded area and still impact the comet. Let's consider now an orbit bounded by the angles as before and also a minimum radius from the body.

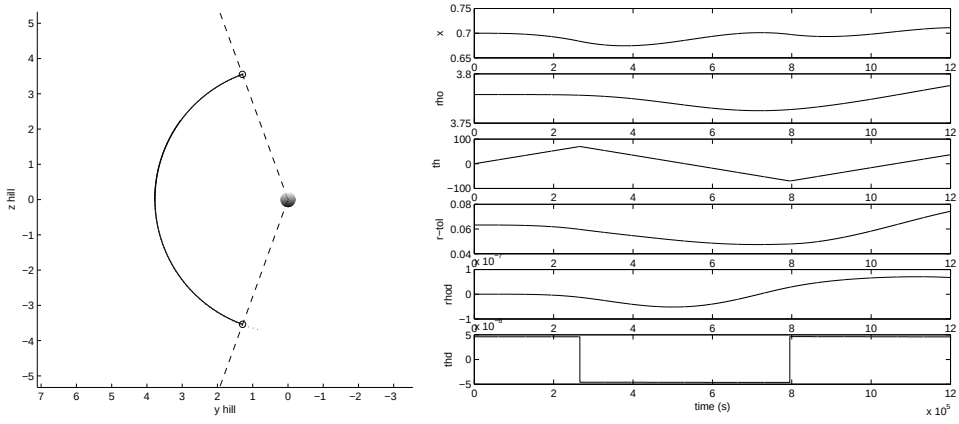

Figure 7.3: Orbit Control with Reversed θ Velocity Impulse with Angle Boundary. Solid = Controlled Trajectory. Blue = Angle Boundary. o = Impulse Location. Position and Velocity Components of the Controlled Orbit are Also Plotted for Reference.

When the spacecraft encounters the angle boundary, a reversal of the $\dot{\theta}$ velocity component impulse will be applied, while a reversal of the $\dot{\rho}$ velocity component impulse will be applied when the radius boundary is violated. Figure 7.5 illustrates the result of this control scheme and figure 7.6 illustrates the addition of a reversal of the $\dot{x}$ velocity component also when the minimum radius boundary is encountered. Note that both methods give similar results for the x offset but the method with the additional $\dot{x}$ velocity control maintains the ρ component better.

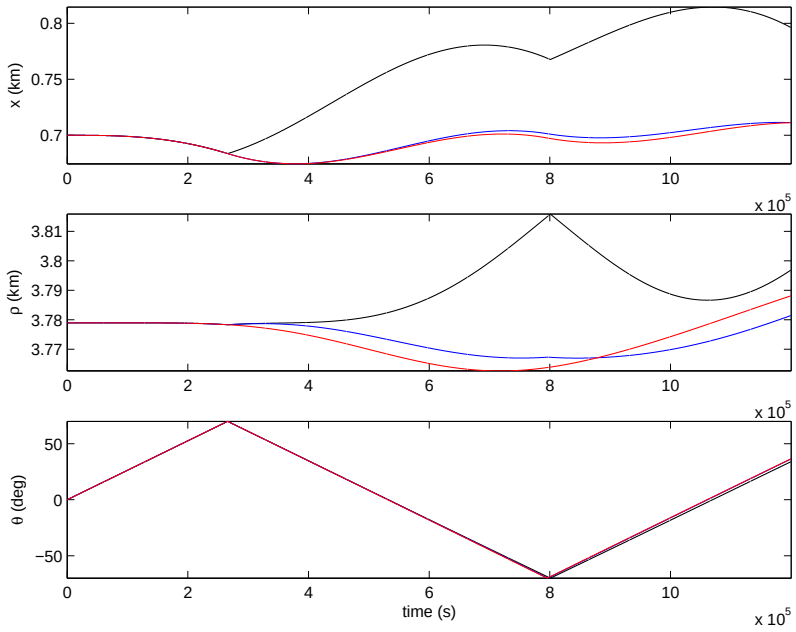

Figure 7.4: Orbit Control Comparison with Angle Boundary. Black = Full Velocity Reversal. Blue = $\dot{\rho}$ and $\dot{\theta}$ Reversal. Red = $\dot{\theta}$ Reversal.

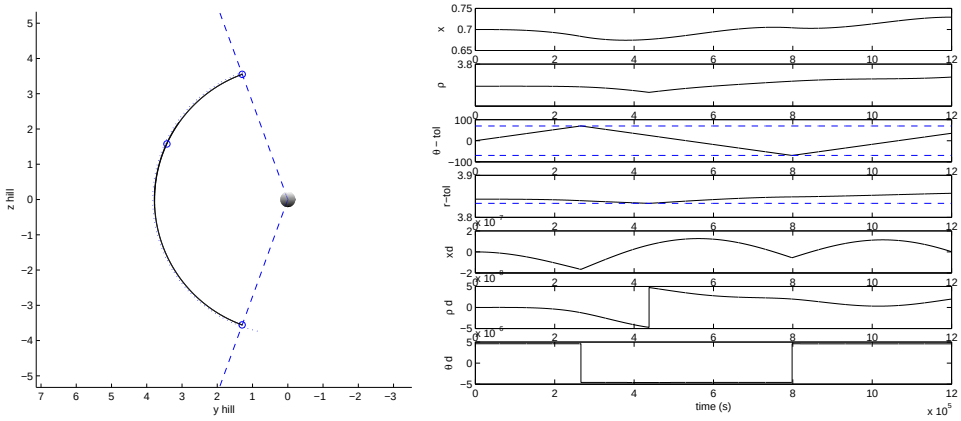

Figure 7.5: Orbit Control with Reversed θ and ρ Impulse with Angle Boundary and ρ Velocity Impulse with Minimum Radius Boundary. Solid = Controlled Trajectory. Blue = Angle Boundary. o = Impulse Location.

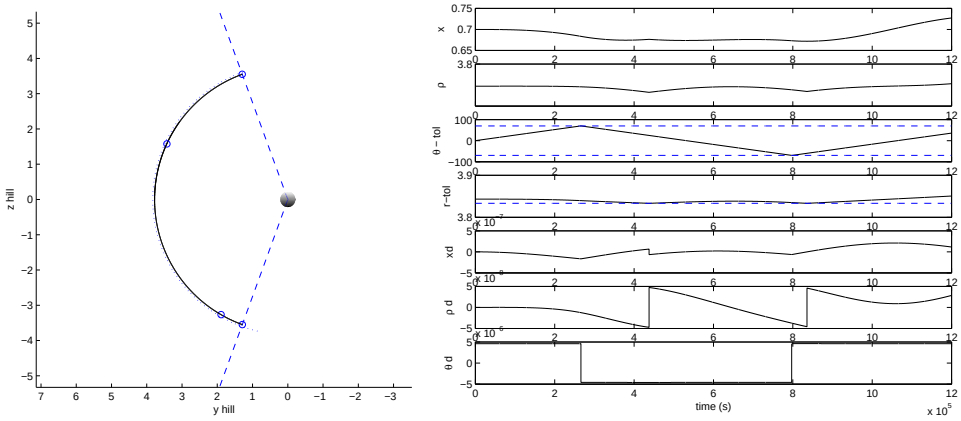

Figure 7.6: Orbit Control with Reversed Full Velocity Impulse with Angle Boundary and ρ Velocity Impulse with Minimum Radius Boundary. Solid = Controlled Trajectory. Blue = Angle Boundary. o = Impulse Location.

7.2 Finite Burn Maneuvers

The control used up until this point has been an impulsive thrust maneuver with the main objective of confining the spacecraft within a region. These methods were necessary to illustrate that the spacecraft could be controlled to remain within an allowable region and not escape. A finite burn maneuver can be developed to recreate the impulsive thrust to reverse the motions and retrace the spacecraft's path. We now consider a finite burn based on the best impulsive control with the form:

$$\vec{T} = m[0, -v_{\dot{\rho}}, -v_{\dot{\theta}}], \tag{7.3}$$

where m is a scale factor and $-v_{\dot{\rho}}$ and $-v_{\dot{\theta}}$ are the velocity components of the spacecraft at the time of boundary crossing. Note that this control thrust is fixed in magnitude and direction once the boundary has been violated. The thrust is turned on when the spacecraft crosses the boundary angle and turned off once its $\dot{\theta}$ becomes the negative of the value at the boundary crossing. Figures 7.7 and 7.8 illustrate the finite burn control for a range of angle boundaries. Note that the deviation from the initial circular orbit depends on the x-offset and the scale factor, m. These represent a more realistic case of orbit control, although we note that other important effects such as orbit uncertainty and central body non-sphericity have not been incorporated.

7.3 Summary

Multiple control maneuvers were presented to restrict the motion of the spacecraft within a defined bounded area. Initially, impulsive maneuvers were explored to verify that stable orbits could be controlled in such a manner and still remain near the original orbit. Finally, a finite burn thrust based on the best performing impulsive

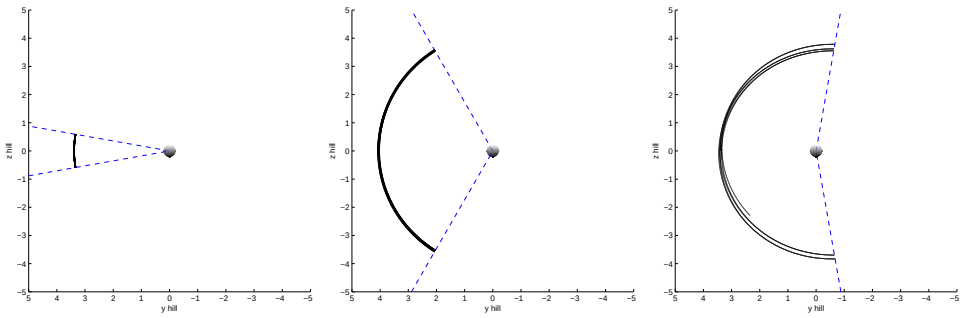

Figure 7.7: Orbit with Initial Offset of $x = 1$ km with Angle Boundary at ± 10, ± 50, and ± 110 degrees. Black = Controlled Trajectory with Finite Burn Reversal of $\dot{\rho}$ and $\dot{\theta}$ Velocity Components. Blue = Angle Boundary.

maneuver was used to demonstrate a more realistic approach for restricting the orbits.

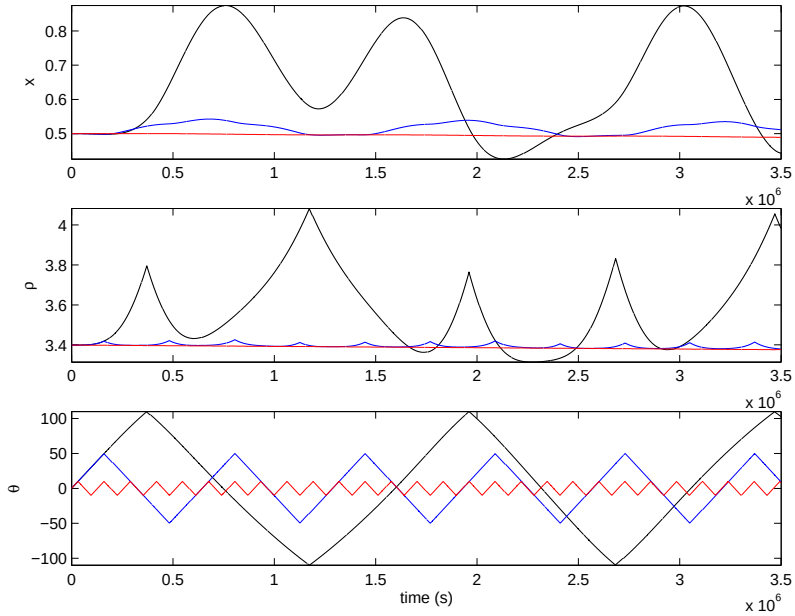

Figure 7.8: Orbit Control Comparison with Varied Angle Boundary. Black = ±110 degrees. Blue = ±50 degrees. Red = ±10 degrees.

CHAPTER VIII

Conclusions

With the small bodies in our solar system, particularly comets, becoming important targets of space missions, this thesis has addressed some of the associated challenges. While many missions have flown by and investigated comets from a distance there has yet to be a mission to actually orbit or land on the surface. The need to determine safe orbits in the vicinity of a comet has become important as this type of mission is near to becoming a reality with ESA's Rosetta mission and the proposed NASA comet surface sample return mission. For the flyby type of comet mission, long term predictions of the rotation state can be similarly important. This is especially evident in NASA's Stardust NExT mission as the spacecraft will not arrive when observations of the comet are made, thus the rotational state needs to be propagated over time to determine any trajectory corrections that may need to be made months or years before the arrival.

8.1 Outgassing Jet Model and Comet Rotational State

In support of a spacecraft mission to a comet, this thesis develops a simple cometary outgassing jet mathematical model for a single jet with constant half angle, δ, using a uniform ellipsoidal model of the comet nucleus. The pressure field created

by the jet is constant across its profile with the magnitude inversely proportional to the square of the distance from the surface. To explore the evolution of the rotational state of a comet nucleus, we derived improved averaged equations for rotationally symmetric bodies as a result of reactive torques produced by jets. The averaged equations were compared to the full equations of motion, integrated using a variational algorithm, and were shown to capture the drift in the rotational state of the comet. This validates the theory presented in Neishtadt et al.[11] and can be used to predict the rotational state of the comet nucleus as it passes through perihelion. Stardust NExT is set to image the crater left behind by Deep Impact on the comet Tempel 1. The optimal time for a trajectory correction is well in advance of the encounter, therefore, for a successful mission, the rotational state of the comet needs to be accurately predicted so that the spacecraft can target the crater for imaging.

With a small correction in the initial conditions, the averaged equations accurately capture the long term drift in the comet's rotation state assuming fixed jet geometry over multiple perihelion passages. The theory allows the comet nucleus dynamics to be propagated over long time spans as a function of a few parameters. This also allows for development of a stochastically varying comet nucleus rotation over very long time spans. A variable jet geometry's effect on the evolution was explored and compared to the averaged equations' prediction with similar results. By examining these averaged equations over long time spans, insight into comet spin up and spin down can be gained. The comet spinning at too large of a rate has severe implications[35]. Comet spin up due to the torques produced by the sublimation in active areas has been considered to be a major cause to the breakup of comets[36]. By being able to predict the long term evolution of the comet's rotational state and spin rate due to outgassing jets, comets which are on a path to break up could be

identified.

8.2 Outgassing Jet Effects and Jet Estimation

If a mission is planned to encounter a comet during a phase of jet activity, there is a need to determine the effect outgassing from discrete jets has on an orbiting spacecraft. A model of a triaxial ellipsoidal comet was simulated using 20 discrete jets based on the comet Wild 2 model to verify the analytical results found by assuming small changes in the orbital elements of the spacecraft relative to the comet. The first case considered was when a spacecraft passes though a nearly radially outgassing jet, such as when it is far from the comet. It was shown that if the spacecraft has a negative radial velocity component, the outgassing jet will decrease the semimajor axis and eccentricity and if the spacecraft has a positive radial velocity component, the outgassing jet will tend to make the orbit more eccentric and increase the semimajor axis for a radial impulse when the spacecraft is located significantly far from the comet.

If, on the other hand, the spacecraft is in close proximity to the comet nucleus, such as during a landing or hovering scenario, it has been shown that the transverse component of the outgassing can affect the semimajor axis and eccentricity of the spacecraft oppositely depending on the relative magnitudes of the components. The orientations of the jets should be known prior to attempting to land on the comet surface to properly predict the trajectory of the spacecraft.

The locations of the jets will need to be determined and compared to images taken of the comet surface in order to estimate the jet orientations. Estimation methods were presented in this thesis to not only estimate the jet locations, but also the outgassing velocity and the half angle. The outgassing velocity can be deter-

mined by taking a measurement of the mass flux and the change in the spacecraft's acceleration using Doppler tracking depending on the outgassing strength and thus the heliocentric distance.

The half angle can be estimated by using boundary crossing points mapped to the surface of the comet. The method for estimating the half angle of the jet includes an algorithm for identifying jet locations when multiple jet outgassing fields have been crossed and for ideally estimating non-circular cross sections. For the half angle estimation method simulated, a small angle error in the measurement results in general in a small half angle estimate error. These estimates help to provide a better trajectory fit for the spacecraft as well as to better predict future trajectories. By knowing probable jet locations, the spacecraft can target these areas for scientific measurements or avoid them to maintain particular orbital parameters.

8.3 Stable Orbits in a Rotating Frame

For longer stays at a comet, the effects of the heliocentric motion about the Sun need to be considered. Since comets are, in general, located significantly far from other celestial bodies, the dynamic setup of the Hill three-body problem nicely describes the system. We have shown that on average Sun synchronous circular orbits offset from the center of mass of the comet body exist in the Hill equations of motion when solar radiation pressure is present. The construction of zero velocity curves provide insight into the stability of these orbits and allows for evaluation of stability in the presence of pressure from an outgassing jet. The stability of the orbits as deemed by zero velocity curve analysis was verified though spectral stability analysis. Although the Hill equations of motion are for a constant rate about the Sun, for short time spans, on the order of weeks, these orbits will persist.

Since the focus is on comets, there are significant perturbations which were examined. In direct connection to the topic of this thesis, a bound on the outgassing magnitude was determined such that the stability of an orbit is maintained as a spacecraft passes though a jet field, i.e. the spacecraft does not escape from the comet body. This bound only allows for the spacecraft to remain in a stable orbit which is not necessarily the original orbit it was following or even in the vicinity of the original orbit. The number of passages through jet fields (either the same one or multiple different ones) has no limit as long as the outgassing magnitude for each jet remains within the given bound.

As discussed, comet bodies are rarely spherical, therefore an ellipsoidal body was then incorporated into the equations of motion to determine the effect on the identified stable orbits. Different effects were explored by varying the radii of the ellipsoidal body and changing it's orientation to the orbits. As expected, the more non-spherical the body became the larger the deviation from the nominal spherical body became. Also, as the spacecraft orbit is located farther from the body, the less the ellipsoidal body affected the deviation from the nominal. Until the exact shape of the comet body is known, orbiting at a larger distance from the body will produce the least deviation from the nominal stable orbit while gathering information to determine the feasibility of maintaining a stable orbit in close proximity to the nucleus.

Imaging the comet surface or monitoring a particular region on the comet requires careful control. In particular, the Sunrise terminator on the comet would provide valuable information in terms of jet activity and may be of interest to monitor. Therefore multiple control maneuvers were presented to restrict the motion of the spacecraft within a defined bounded area. Initially, impulsive maneuvers

were explored to verify that stable orbits could be controlled in such a manner and still remain near the original orbit. Finally, a finite burn thrust based on the best performing impulsive maneuver was used to demonstrate a more realistic approach for restricting the orbits. These restricted orbits give the spacecraft the ability to "hover" over a particular region.

8.4 Future Directions

While this thesis contributes to many areas in the field of outgassing jet dynamics, there are more effects to be considered.

8.4.1 Rotational State of the Comet Nucleus

Although this thesis provided a basic look at the effects that variable jet geometry on the rotational evolution of a comet nucleus, a more systematic approach could be devised. Previously, we assumed that as jets expired, new jets appeared randomly. Using the predicted changes in the the rotational state, the jets could be correlated to the rotational axis orientation such that new jets would appear on only sunlit areas of the comet surface. In addition, the spin up of the comet could be examined more carefully. Using the jet reactive torques, it may be possible to find conditions on the jets, their geometry, or the rotation axis that will lead to the eventual breakup of the comet nucleus.

8.4.2 Orbit Sensitivity to Outgassing

The sensitivity of the orbits to the outgassing perturbations needs to be quantified as it may affect the navigation precision. A correlation between the outgassing magnitude and the immediate deviation from the nominal orbit could be made. Assuming that the time it takes to pass though an outgassing jet field is small, the

results from the two-body orbital elements analysis could be applied. Also, since the outgassing jet parameters may not be well known, a covariance analysis with respect to the jet parameter errors on a spacecraft's trajectory would provide more insight into the orbit's sensitivity.

8.4.3 Stable Orbits in a Rotating Frame

For long term orbiting, the elliptical heliocentric motion of the comet would need to be considered. This thesis assumed that the spacecraft would be in the vicinity of the comet for a short time span such that the heliocentric motion would be approximately constant. This would not be the case for a mission goal of long term monitoring of comet activity or multiple surface sampling. A possible solution for this would be to determine stable orbits for segments of the heliocentric path by averaging over the changing angular rate. Maneuvers could be performed at the intersection of the segments to transfer the spacecraft from one stable orbit to a new stable orbit for the next segment. The segment size would need to be a function of the angular rate. Therefore there would need to be more segments and more transfers near perihelion where the angular rate is rapidly changing.

APPENDICES

The algorithm for the variational integration[28] used is presented. The rotational equations of motion for a rigid body in a body fixed frame.

$$\mathbf{J} \cdot \dot{\vec{\omega}} + \vec{\omega} \times \mathbf{J} \cdot \vec{\omega} = \vec{M}, \tag{A.1}$$

$$\dot{\mathbf{R}}_\mathbf{t} = \mathbf{R}_\mathbf{t} \times \vec{\omega}, \tag{A.2}$$

where $\mathbf{J} \in \mathbf{R}^{3\times3}$ is the inertia matrix of the body, $\vec{M}, \vec{\omega} \in \mathbf{R}^3$ are the moment and angular velocity vectors, respectively, and $\mathbf{R}_\mathbf{t}$ is the rotation matrix.

To begin, denote the function $\mathbf{S}(\cdot)$ as a skew mapping of a generic vector to a matrix such that for $x, y \in \mathbf{R}^3$:

$$\mathbf{S}(x)y = x \times y. \tag{A.3}$$

Also, let the matrix $\mathbf{J}_d$ be related to the inertia matrix, $\mathbf{J}$, by the relationship:

$$\mathbf{J} = trace[\mathbf{J}_d]\mathbf{I}_{3\times3} - \mathbf{J}_d. \tag{A.4}$$

Note that $\mathbf{J}_d$ is symmetric and satisfies the following equation for ω:

$$\mathbf{S}(\mathbf{J}\omega) = \mathbf{S}(\omega)\mathbf{J}_d + \mathbf{J}_d\mathbf{S}(\omega). \tag{A.5}$$

For a general shape, $\mathbf{J}_d$ is defined as:

$$\mathbf{J}_d = \begin{bmatrix} \int x^2 dm & \int xy dm & \int xz dm \\ \int xy dm & \int y^2 dm & \int yz dm \\ \int xz dm & \int yz dm & \int z^2 dm \end{bmatrix} = \int \vec{\rho}\vec{\rho} dm. \tag{A.6}$$

For a constant density ellipsoid with principal axes a, b, c and mass M, as was assumed for the comet body above, $\mathbf{J}_d$ is defined as:

$$\mathbf{J}_d = \frac{1}{5}M \begin{bmatrix} a^2 & 0 & 0 \\ 0 & b^2 & 0 \\ 0 & 0 & c^2 \end{bmatrix}. \tag{A.7}$$

An initial ω_k, $\mathbf{J}$, and $\mathbf{R}_k$ are known (k denotes time step). To begin, the implicit Eq. A.8 needs to be solved for $\mathbf{F}_k$.

$$\mathbf{S}(\mathbf{J}\omega_k) = \frac{1}{h}(\mathbf{F}_k\mathbf{J}_d - \mathbf{J}_d\mathbf{F}_k^T), \tag{A.8}$$

where h is the time step.

To solve this equation, consider the implicit Eq. A.9 which can be solved by using the following Cayley Transformation into equivalent vector Eqs. A.10 and A.11[37]. Note that $g = h\mathbf{J}\omega_k$ is the relationship which solves Eq. A.8.

$$\mathbf{S}(g) = \mathbf{F}_k\mathbf{J}_d - \mathbf{J}_d\mathbf{F}_k^T, \tag{A.9}$$

$$G_{Cay}(f) = g + g \times f + (g^T f)f - 2\mathbf{J}f = 0, \tag{A.10}$$

$$\mathbf{F}_{Cay} = (\mathbf{I}_{3\times3} + \mathbf{S}(f))(\mathbf{I}_{3\times3} - \mathbf{S}(f))^{-1}. \tag{A.11}$$

Here $\mathbf{F}_{Cay}$ is the solution for $\mathbf{F}_k$ which solves Eq. A.8. To find $\mathbf{F}_{Cay}$, the vector f must be computed. To do this, the Jacobian $\bigtriangledown G_{Cay}(f)$ is needed

$$\bigtriangledown G_{Cay}(f) = \mathbf{S}(g) - 2\mathbf{J} + (g^T f)\mathbf{I}_{3\times3} - fg^T. \tag{A.12}$$

Using Newton's iteration on Eq. A.13, solve for f using the previous solution as the initial guess, $f_{k+1,0} = f_{k,i}$, (use angular velocity as an initial guess for $f_{0,0}$) and the following equation (i denotes iteration number and k denotes time step):

$$f_{k,i+1} = f_{k,i} - \bigtriangledown G_{Cay}(f_{k,i})^{-1} G_{Cay}(f_{k,i}), \tag{A.13}$$

until the condition from Eq. A.10 or computationally, $\|G_{Cay}(f)\| < tolerance$ is satisfied from the iteration on f. $\mathbf{F}_{Cay}$ $(= \mathbf{F}_k)$ can then be computed from Eq. A.11.

Once $\mathbf{F}_k$ is known, the rotation matrix, $\mathbf{R}_{k+1}$ (body fixed frame to inertial frame) for the next time step is found as:

$$\mathbf{R}_{k+1} = \mathbf{R}_k \mathbf{F}_k. \tag{A.14}$$

In general, the moment vector is produced from the potential, V, and is determined as $\mathbf{S}(M) = \frac{\partial V}{\partial \mathbf{R}}^T \mathbf{R} - \mathbf{R}^T \frac{\partial V}{\partial \mathbf{R}}$. For our comet body's complex rotation, the moments are produced by the jets and using $\mathbf{R}_{k+1}$, we can then solve for M_{k+1} from our outgassing model. The angular velocity is calculated from:

$$\omega_{k+1} = \mathbf{J}^{-1}(\mathbf{F}_k^T \mathbf{J} \omega_k + h M_{k+1}). \tag{A.15}$$

BIBLIOGRAPHY

[1] JPL, *Composite and Stereo Images of Comet Wild2*, 2004, http://stardust.jpl.nasa.gov/, retrieved September 2008.

[2] *Announcement of Opportunity: New Frontiers Program 2003 and Missions of Opportunity (AO-03-OSS-03)*, NASA, October 2003, http://research.hq.nasa.gov, retrieved November 2007.

[3] Miller, J. K., Weeks, C. J., and Wood, L. J., "Orbit Determination Strategy and Accuracy for a Comet Rendezvous Mission," *Journal of Guidance, Control, and Dynamics*, Vol. 13, No. 5, 1990, pp. 775–784.

[4] Scheeres, D. J., Marzari, F., Tomasella, L., and Vanzani, V., "ROSETTA mission: satellite orbits around a cometary nucleus," *Planet. Space Sci.*, Vol. 46, No. 6/7, 1998, pp. 649–671.

[5] Crifo, J. F., Itkin, A. L., and Rodionov, A. V., "The Near-Nucleus Coma Formed by Interacting Dusty Gas Jets Effusing from a Cometary Nucleus: I," *ICARUS*, Vol. 116, 1995, pp. 77–112.

[6] Sekanina, Z., Brownlee, D. E., Economou, T. E., Tuzzolina, A. J., and Green, S. F., "Modeling the Nucleus and Jets of Comet 81P/Wild 2 Based on the Stardust Encounter Data," *Science*, Vol. 304, No. 5678, 2004, pp. 1769–1774.

[7] Dankowicz, H., "Some Special Orbits in the Two-Body Problem with Radiation Pressure," *Celestial Mechanics and Dynamical Astronomy*, Vol. 58, 1994, pp. 353–370.

[8] Scheeres, D. J. and Marzani, F., "Spacecraft Dynamics in the Vicinity of a Comet," *Journal of the Astronautical Sciences*, Vol. 50, No. 1, 2002, pp. 35–52.

[9] Scheeres, D. J., "Satellite Dynamics about Small Bodies: Averaged Solar Radiation Pressure Effects," *Journal of the Astronautical Sciences*, Vol. 47, No. 1, 1999, pp. 25–46.

[10] Chesley, S. R. and Yeomans, D. K., "Nongravitational Accelerations on Comets," *Dynamics of Populations of Planetary Systems Proceedings IAU Colloquium*, Vol. 197, 2005, pp. 289–302.

[11] Neishtadt, A. I., Scheeres, D. J., Sidorenko, V. V., Stooke, P. J., and Vasiliev, A. A., "Evolution of Comet Nucleus Rotation," *ICARUS*, Vol. 157, 2002, pp. 205–218.

[12] Drahus, M. and Waniak, W., "Non-constant Rotation Period of Comet C/2001 K5 (LINEAR)," *ICARUS*, Vol. 185, 2006, pp. 544–557.

[13] Gutiérrez, P. J., Ortiz, J. L., Rodrigo, R., López-Moreno, J. J., and Jorda, L., "Evolution of the Rotational State of Irregular Cometary Nuclei," *Earth, Moon and Planets*, Vol. 90, 2002, pp. 239–247.

[14] Samarasinha, N. H., Mueller, B. E. A., Belton, M. J. S., and Jorda, L., "Rotation of Cometary Nuclei," *Comets II*, 2004, pp. 281–299.

[15] Scheeres, D. J., "Dynamics About Uniformly Rotating Tri-Axial Ellipsoids. Applications to Asteroids," *ICARUS*, Vol. 110, 1994, pp. 225–238.

[16] Brownlee, D. E., Horz, F., Newburn, R. L., Zolensky, M., Duxbury, T. C., Sandford, S., Sekanina, Z., Tsou, P., Hanner, M. S., Clark, B. C., Green, S. F., and Kissel, J., "Surface of Young Jupiter Family Comet 81P/Wild 2: View from the Stardust Spacecraft," *Science*, Vol. 304, No. 5678, 2004, pp. 1764–1769.

[17] A'Hearn, M. F., Belton, M. J. S., Delamere, W. A., Kissel, J., Klaasen, K. P., McFadden, L. A., Meech, K. J., Melosh, H. J., Schultz, P. H., Sunshine, J. M., Thomas, P. C., Veverka, J., Yeomans, D. K., Baca, M. W., Busko, I., Crockett, C. J., Collins, S. M., Desnoyer, M., Eberhardy, C. A., Ernst, C. M., Farnham, T. L., Feaga, L., Groussin, O., Hampton, D., Ipatov, S. I., Li, J.-Y., Lindler, D., Lisse, C. M., Mastrodemos, N., W. M. Owen, J., Richardson, J. E., Wellnitz, D. D., and White, R. L., "Deep Impact: Excavating Comet Tempel 1," *Science*, Vol. 310, No. 5746, 2005, pp. 258–264.

[18] Combi, M. R., Kabin, K., DeZeeuw, D. L., and Gombosi, T. I., "Dust-Gas Interrelations in Comets: Observations and Theory," *Earth, Moon, and Planets*, Vol. 79, 1997, pp. 275–306.

[19] Marsden, B. G., Sekanina, Z., and Yeomans, D. K., "Comets and nongravitational forces," *Astronomical Journal*, Vol. 78, 1973, pp. 211–225.

[20] JPL, *Stardust, NASA's Comet Sample Return Mission*, 2004, http://stardust.jpl.nasa.gov/, retrieved October 2008.

[21] Duxbury, T. C., Newburn, R. L., and Brownlee, D. E., "Comet 81P/Wild 2 size, shape, and orientation," *Journal of Geophysical Research*, Vol. 109, 2004.

[22] Weeks, C. J., "The Effect of Comet Outgassing and Dust Emission on the Navigation of an Orbiting Spacecraft," *Journal of Astronautical Sciences*, Vol. 43, No. 3, 1995, pp. 327–343.

[23] Lamy, P. L., Toth, I., Fernédez, Y. R., and Weaver, H. A., "The Sizes, Shapes, Albedos, and Colors of Cometary Nuclei," *Comets II*, 2004, pp. 223–264.

[24] Belton, M. J. S., Samarasinha, N. H., Fernndez, Y. R., and Meech, K. J., "The excited spin state of Comet 2P/Encke," *ICARUS*, Vol. 175, 2005, pp. 181–193.

[25] Scheeres, D. J., Marzani, F., and Rossi, A., "Evolution of NEO rotation rates due to close encounters with Earth and Venus," *Icarus*, Vol. 170, 2004, pp. 312–323.

[26] Pravec, P., Harris, A. W., Scheirich, P., Kušniréka, P., Ŝarounové, L., Hergenrother, C. W., Mottola, S., M. D. Hickse, G. M., Krugly, Y. N., Shevchenko, V. G., Nolani, M. C., Howell, E. S., Kaasalainen, M., Galéd, A., Brownl, P., DeGraff, D. R., Lambert, J. V., Jr., W. R. C., and Foglia, S., "Tumbling asteroids," *ICARUS*, Vol. 173, 2005, pp. 108–131.

[27] Scheeres, D. J., "Rotational fission of contact binary asteroids," *ICARUS*, Vol. 189, 2007, pp. 370–385.

[28] Lee, T., Leok, M., and McClamroch, N. H., "Lie Group Variational Integrators for the Full Body Problem in Orbital Mechanics," *Celestial Mechanics and Dynamical Astronomy*, Vol. 98, No. 2, 2007, pp. 121–144.

[29] Neishtadt, A. I., Scheeres, D. J., Sidorenko, V. V., and Vasiliev, A. A., "The Influence of Reactive Torques on Comet Nucleus Rotation," *Celestial Mechanics and Dynamical Astronomy*, Vol. 83, No. 3, 2003, pp. 249–275.

[30] Baruh, H., *Analytical Dynamics*, MacGraw-Hill, 1999.

[31] MacMillan, W. D., *Dynamics of Rigid Bodies*, MacGraw-Hill, 1936.

[32] Byram, S. M. and Scheeres, D. J., "Models for the Comet Dynamical Environment," *Journal of Guidance, Control, and Dynamics*, Vol. 30, No. 5, 2007, pp. 1445–1454.

[33] Broschart, S. B. and Scheeres, D. J., "Boundedness of Spacecraft Hovering Under Dead-Band Control in Time-Invariant Systems," *Journal of Guidance, Control, and Dynamics*, Vol. 30, No. 2, 2007, pp. 601–610.

[34] Villac, B. F. and Scheeres, D. J., "Escape Trajectories in the Hill Three-Body Problem and Applications," *Journal of Guidance, Control, and Dynamics*, Vol. 26, No. 2, 2003, pp. 224–232.

[35] Davidson, B. J. R., "Tidal Splitting and Rotational Breakup of Solid Biaxial Ellipsoids," *ICARUS*, Vol. 149, 2001, pp. 375–383.

[36] Samarasinha, N. H. and Belton, M. J. S., "Long-Term Evolution of Rotational States and Nongravitational Effects for Halley-like Cometary Nuclei," *ICARUS*, Vol. 116, 2002, pp. 340–358.

[37] "Cayley-based LGVI," 10-18-2006, unpublished memo obtained from Eugene Fahnestock.